Vol.4 No.I Tahun 2021

P-ISSN : 2621-0215
E-ISSN : 2621-489X

Al-Fiziya

Journal of Materials Science, Geophysics, Instrumentation and Theoretical Physics

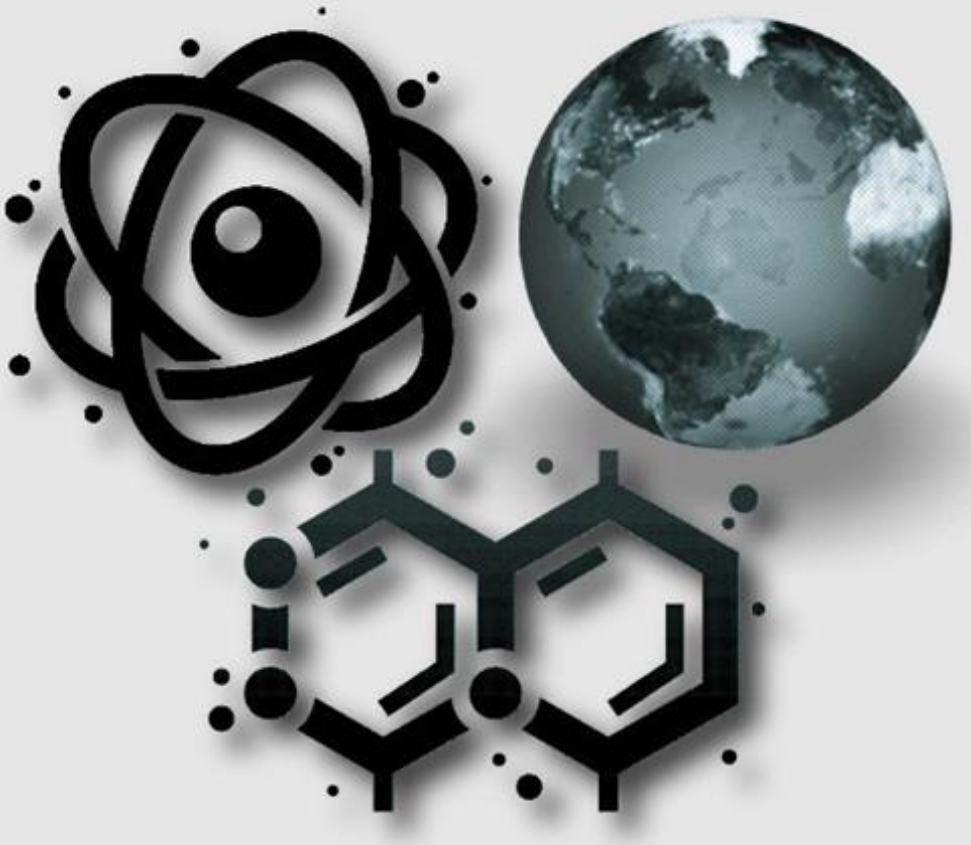

Published by
Program Studi Fisika
Fakultas Sains dan Teknologi
Universitas Islam Negeri Syarif Hidayatullah Jakarta

AL-FIZIYA:

Journal of Materials Science, Geophysics, Instrumentation, and Theoretical Physics

Vol. 4, No. I, Tahun 2021

Alamat Redaksi
Gedung Fakultas Sains dan Teknologi Lt. 3
Jl. Ir. H Juanda No.95 Ciputat 15412 Tangerang
Telp. (6221)743731, (6221)7493315
Email: al-fiziya@uinjkt.ac.id

Published by
Program Studi Fisika, Fakultas Sains dan Teknologi
Universitas Islam Negeri Syarif Hidayatullah Jakarta

PENGANTAR REDAKSI

Assalamu'alaikum, Wr. Wb.

Puji Syukur kita panjatkan kehadirat Allah SWT, dengan terbitnya Al-Fiziya: *Journal of Materials Science, Geophysics, Instrumentation, and Theoretical Physics* Vol 4, No. I, Tahun 2021 dengan nomor ISSN: 2621-0215 dan E-ISSN: 2621-489X sebagai jurnal penelitian dan pengembangan ilmu fisika yang diterbitkan oleh Program Studi Fisika Fakultas Sains dan Teknologi UIN Syarif Hidayatullah Jakarta. Jurnal ini menyajikan artikel-artikel penelitian dan pengembangan terkini baik dalam Bahasa Indonesia maupun Bahasa Inggris di bidang fisika murni dan terapan, antara lain bidang fisika material, geofisika, fisika instrumentasi, dan fisika teori. Jurnal ini merupakan sarana publikasi bagi dosen dan para peneliti yang bergerak di bidang penelitian dan pengembangan ilmu fisika. Dengan demikian, melalui penerbitan jurnal ini kami memberikan kesempatan seluas-luasnya bagi siapapun yang ingin berpartisipasi dalam menyampaikan buah pikirannya melalui tulisan atau artikel yang akan kami muat pada edisi berikutnya.

Artikel yang masuk akan melalui proses seleksi oleh dewan editor dan review yang melibatkan mitra bestari baik dari para dosen ahli dibidangnya berdasarkan kesesuaian isi dan bobot karya ilmiah. Untuk informasi lengkap submit dan tata cara penulisan dalam Al-Fiziya: *Journal of Material Science, Geophysics, Instrumentation, and Theoretical Physics* dapat dilihat pada pedoman penulisan artikel di halaman akhir penerbitan atau dapat mengakses website kami di http://journal.uinjkt.ac.id/index.php/al-fiziya. Atas nama dewan redaksi, kami mengucapkan terimakasih atas dukungan dan partisipasi dari semua pihak hingga terbitnya Al-Fiziya: *Journal of Materials Science, Geophysics, Instrumentation, and Theoretical Physics.*

Editorial in chief
Sitti Ahmiatri Saptari

Daftar Isi

Vol 4, No. I Tahun 2021

Available online at:
Al-Fiziya: Journal of Materials Science, Geophysics, Instrumentation and Theoretical Physics
Website: http://journal.uinjkt.ac.id/index.php/al-fiziya
Vol.4 No.I Tahun 2021, 1 - 7

Ohmic and Diamagnetic Currents Contribution on the Electromagnetic Penetration Depth of a Conducting Surface

Adam B. Cahaya[1,†]

[1]Department of Physics, Faculty of Mathematics and Natural Sciences, Universitas Indonesia
Depok 16424, Indonesia

[†]adam@sci.ui.ac.id

Submitted: February 2021; Revised: March 2021; Approved: May 2021; Available Online: June 2021

Abstrak. Karena memiliki elektron konduksi, logam merupakan reflektor yang baik untuk gelombang elektromagnetik. Gelombang elektromagnetik yang menembus permukaan logam memiliki kedalaman tembus yang terbatas. Ada dua limit yang sering dipelajari dengan baik dalam buku teks fisika. Limit pertama adalah limit gelombang elektromagnetik frekuensi tinggi yang menembus logam dengan konduktivitas kecil dan medan statis (frekuensi rendah). Limit kedua adalah gelombang elektromagnetik yang menembus superkonduktor (logam dengan konduktivitas sangat besar). Dalam artikel ini kami mempelajari daerah pertengahan antara dua limit ekstrim ini. Dengan menetapkan kerapatan arus listrik sebagai jumlah total arus Ohmik dan diamagnetik, kami menunjukkan transisi antara dua batas ini.

***Kata Kunci**: Penetrasi Elektromagnetik, skin depth, diamagnetic current, Maxwell equations, London equation.*

Abstract. Due to its conducting electron, metal is a good reflector for electromagnetic wave. An electromagnetic wave penetrating a metallic surface has a finite penetrating depth. There are two limit that are well studied in the physics textbooks. They are high frequency electromagnetic wave penetrating a metal with small conductivity and a static (low frequency) field penetrating a superconductor (metal with infinitely large conductivity). In this article we study the intermediate regime between these two limits. By setting the electric current density as the total sum of both Ohmic and Diamagnetic currents, we derive the penetration depth in the intermediate regime., we show the transition between these two limits.

***Keywords**: Electromagnetic penetration, skin depth, diamagnetic current, Maxwell equations, London equation.*

DOI : *10.15408/fiziya.v4i1.19790*

P-ISSN: 2621-0215, E-ISSN: 2621-489X

INTRODUCTION

Due to its conducting nature, electromagnetic waves are reflected by metallic surface. The reflection mechanism can be mathematically described by substituting the following Ohmic current into the Maxwell equation[1].

$$\mathbf{J} = \sigma\mathbf{E}, \tag{1}$$

where $\mathbf{J}$ is electric current density, σ is conductivity and $\mathbf{E}$ is the electric field. In the limit of small conductivity, the skin depth of the penetrating electromagnetic wave is inversely proportional to the conductivity of the metal[2].

$$\delta = \frac{2}{\sigma}\sqrt{\frac{\varepsilon}{\mu}}. \tag{2}$$

Here ε is the permittivity and μ is the permeability. Because of that, one can expect that the skin depth of superconductor is zero. However, Meisner effect shows that a penetrating magnetic field has a finite skin depth, also known as London penetration depth l, is not zero [3], [4].

$$l = \sqrt{\frac{m}{\mu n e^2}}. \tag{3}$$

Here m is the electron mass, $-e$ is the electron charge and n is the carrier density. London penetration can be derived by substituting the following London diamagnetic current into the Maxwell equation and taking a static limit [5]–[7]. The reflection of electromagnetic field in superconductor is mainly caused by the London diamagnetic current

$$\mathbf{J} = -\frac{ne^2}{m}\mathbf{A}. \tag{4}$$

Here $\mathbf{A}$ is the vector potential.

δ and λ are two limiting cases that are well studied in the physics textbooks [1], [8]. In this article, we focus on the intermediate regime where the effect of both ohmic and diamagnetic current are important. The effect of Ohmic current has been widely studied in surface designs [9], [10]. On the other hand, the study of diamagnetic current is gaining increasing attention in physics [11], [12] and related areas [13], [14].

METHOD: MATHEMATICAL FORMALISM

The dynamics of electric field $\mathbf{E}$ and magnetic field $\mathbf{B}$ in a material is best described by Maxwell equations. The Maxwell equations can be written in term of scalar potential ϕ and vector potential $\mathbf{A}$.

$$\mathbf{E} = -\boldsymbol{\nabla}\phi - \frac{\partial \mathbf{A}}{\partial t}, \tag{5a}$$

$$\mathbf{B} = \boldsymbol{\nabla} \times \mathbf{A}, \tag{5b}$$

By using Lorentz gauge condition,

$$\boldsymbol{\nabla} \cdot \mathbf{A} + \varepsilon\mu\frac{\partial \phi}{\partial t} = \mathbf{0}, \tag{6}$$

one can obtain the partial differential equations for ϕ and vector potential $\mathbf{A}$ [15]

$$\left(\nabla^2 - \frac{\partial^2}{c^2 \partial t^2}\right)\phi = -\frac{\rho}{\varepsilon}, \tag{6a}$$

$$\left(\nabla^2 - \frac{\partial^2}{c^2 \partial t^2}\right)\mathbf{A} = -\mu \mathbf{J}. \tag{6b}$$

Here $c = 1/\sqrt{\varepsilon\mu}$ is the speed of light in the material. We will solve Eqs. (6a) and (b) by choosing $\phi = 0$. In this case one can show that for electromagnetic wave propagating in x direction, the solution of $\mathbf{A}, \mathbf{E}$ and $\mathbf{B}$ that have the following form

$$\mathbf{A} = A\hat{\mathbf{y}}e^{i(kx-\omega t)} \tag{7a}$$

$$\mathbf{E} = -\frac{\partial \mathbf{A}}{\partial t} = i\omega A\hat{\mathbf{y}}e^{i(kx-\omega t)} \tag{7b}$$

$$\mathbf{B} = \nabla \times \mathbf{A} = ikA\hat{\mathbf{z}}e^{i(kx-\omega t)} \tag{7c}$$

Here k is the wavenumber and ω is the frequency. Using this choice of ϕ and vector potential $\mathbf{A}$, we can derive the penetration depth by examining the imaginary part of k because it creates an exponentially decaying term in the electromagnetic fields**.** The inverse of this imaginary term is the penetration depth.

In the following subsections we illustrate the derivation of these two limits: high frequency electromagnetic wave penetrating a metal with small conductivity and a low frequency field penetrating a metal with large conductivity, by consider Ohmic and diamagnetic current, respectively. In the next Section we will combine both currents to see the penetration depth for intermediate regimes.

Reflection by Ohmic current

To study the limit of high frequency electromagnetic wave penetrating a metal with small conductivity, we solve Eq. (6b) by substiting Eq. (1).

$$\left(\nabla^2 - \frac{\partial^2}{c^2 \partial t^2}\right)\mathbf{A} = -\mu \mathbf{J}_{\text{Ohm}} = \mu\sigma \frac{\partial \mathbf{A}}{\partial t} \tag{8}$$

Substituting Eq. (7) to Eq. (8) we arrive at the following equation

$$\left(-k^2 + \frac{\omega^2}{c^2} + i\mu\sigma\omega\right)A\hat{\mathbf{y}}e^{i(kx-\omega t)} = 0 \tag{9}$$

The dispersion $k(\omega)$ can then be derived as follows.

$$k = \frac{\omega}{c}\sqrt{1 + \frac{i\sigma}{\varepsilon\omega}} \tag{10}$$

For small conductivity and large frequency $\sigma \ll \varepsilon\omega$, one can show that the imaginary part of k is proportional to σ

$$\lim_{\sigma \ll \varepsilon\omega} k = \frac{\omega}{c}\left(1 + \frac{i\sigma}{2\varepsilon\omega}\right) = \frac{\omega}{c} + i\frac{\sigma}{2}\sqrt{\frac{\mu}{\varepsilon}} \tag{11}$$

The inverse of this imaginary term is the penetration depth in Eq. (2).

Reflection by Diamagnetic current

To study the limit of low frequency electromagnetic wave penetrating a metal with large conductivity, we solve Eq. (6b) by substituting Eq. (4).

$$\left(\nabla^2 - \frac{\partial^2}{c^2 \partial t^2}\right)\mathbf{A} = -\mu \mathbf{J}_{\text{Dia}} = \mu \frac{ne^2}{m}\mathbf{A} \tag{12}$$

Substituting Eq. (7a) to Eq. (12) we arrive at the following equation

$$\left(-k^2 + \frac{\omega^2}{c^2} - \mu\frac{ne^2}{m}\right)A\hat{\mathbf{y}}e^{i(kx-\omega t)} = 0 \tag{13}$$

The dispersion $k(\omega)$ can then be derived as follows.

$$k = \frac{\omega^2}{c^2} - \mu\frac{ne^2}{m} \tag{15}$$

For small frequency, k is purely imaginary

$$\lim_{\omega\to 0} k = i\mu\frac{ne^2}{m} \tag{16}$$

Its inverse is the London penetration depth in Eq. (3).

RESULT AND DISCUSSION: REFLECTION BY OHMIC AND DIAMAGNETIC CURRENT

To study the intermediate regime, we set the electric current density as the total sum of both Ohmic and Diamagnetic currents.

$$\mathbf{J} = \mathbf{J}_{\text{Ohm}} + \mathbf{J}_{\text{Dia}} = \sigma\mathbf{E} - \frac{ne^2}{m}\mathbf{A} \tag{17}$$

In terms of δ and l:

$$\mu\mathbf{J} = \frac{2}{c\delta}\frac{\partial\mathbf{A}}{\partial t} - \frac{1}{l^2}\mathbf{A} \tag{18}$$

We can solve the expression for $\mathbf{A}$ by substituting Eq. (8) back to Eq. (6b)

$$\left(\boldsymbol{\nabla}^2 - \frac{\partial^2}{c^2\partial t^2}\right)\mathbf{A} = -\frac{2}{c\delta}\frac{\partial\mathbf{A}}{\partial t} + \frac{1}{l^2}\mathbf{A} \tag{19}$$

Substituting Eq. (7a) to Eq. (12) we arrive at the following equation

$$\left(-k^2 + \frac{\omega^2}{c^2} + i\frac{2\omega}{c\delta} - \frac{1}{l^2}\right)A\hat{\mathbf{y}}e^{i(kx-\omega t)} = 0 \tag{20}$$

The dispersion $k(\omega)$ can then be derived as follows.

$$k = \sqrt{\frac{\omega^2}{c^2} - \frac{1}{l^2} + i\frac{2\omega}{c\delta}} \tag{21}$$

To discuss the penetration depth *i.e.* the inverse of the imaginary part of k, we need to look at two frequency regimes separated by the critical frequency $\omega_0 = c/l$

High frequency $\omega > c/l$

In this case, the dispersion $k(\omega)$ can be written as follows

$$k = \frac{1}{c}\left((\omega^2 - \omega_0^2)^2 + \left(\frac{2c\omega}{\delta}\right)^2\right)^{\frac{1}{4}} e^{i\alpha/2} \tag{22a}$$

$$\alpha = \tan^{-1}\frac{2c\omega}{(\omega^2 - \omega_0^2)\delta} \tag{22b}$$

Its imaginary part is as follows.

$$\text{Im}\, k = \frac{1}{c}\left((\omega^2 - \omega_0^2)^2 + \left(\frac{2c\omega}{\delta}\right)^2\right)^{\frac{1}{4}} \sin\frac{\alpha}{2} \tag{23a}$$

$$= \frac{1}{c\sqrt{2}}\sqrt{\sqrt{(\omega^2 - \omega_0^2)^2 + \left(\frac{2c\omega}{\delta}\right)^2} - (\omega^2 - \omega_0^2)} \tag{23b}$$

Low frequency $\omega < c/l$

In this case, the dispersion $k(\omega)$ can be written as follows

$$k = \frac{i}{c}\left((\omega_0^2 - \omega^2)^2 + \left(\frac{2c\omega}{\delta}\right)^2\right)^{\frac{1}{4}} e^{-i\beta/2} \tag{24a}$$

$$\beta = \tan^{-1}\frac{2c\omega}{(\omega_0^2 - \omega^2)\delta} \tag{24b}$$

Its imaginary part is as follows.

$$\mathrm{Im}\, k = \frac{1}{c}\left((\omega_0^2 - \omega^2)^2 + \left(\frac{2c\omega}{\delta}\right)^2\right)^{\frac{1}{4}} \cos\frac{\beta}{2} \tag{25a}$$

$$= \frac{1}{c\sqrt{2}}\sqrt{\sqrt{(\omega_0^2 - \omega^2)^2 + \left(\frac{2c\omega}{\delta}\right)^2} + (\omega_0^2 - \omega^2)} \tag{25b}$$

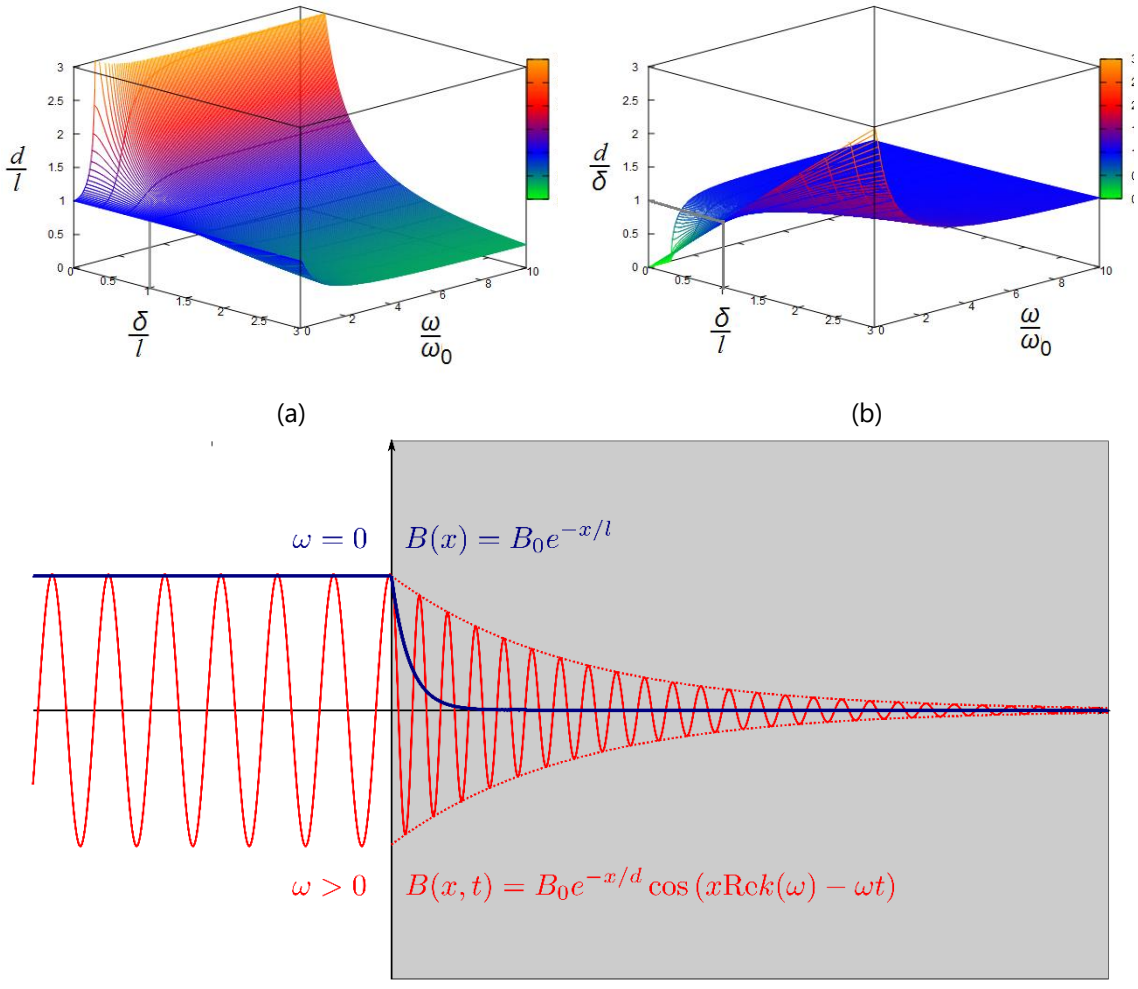

Figure 1. Penetration depth d as a function of δ/l and ω/ω_0. (a)Penetration depth normalized to l. By normalizing d to l we can clearly see that in the limit of low frequency, d approach l. (b)Penetration depth normalized to δ. By normalizing d to δ we can clearly see that in the limit of high frequency, d approach δ. (c) Illustration of penetration of electromagnetic wave.

Electromagnetic penetration depth

We note that Eq. (23b) and (25b) are exactly the same. Because of that the penetration depth *d* can be summarize in one expression

$$d = \frac{l\sqrt{2}}{\sqrt{\sqrt{\left(\frac{\omega^2}{\omega_0^2}-1\right)^2+\left(2\frac{l}{\delta}\frac{\omega}{\omega_0}\right)^2}-\left(\frac{\omega^2}{\omega_0^2}-1\right)}} = \frac{\delta}{\sqrt{2}}\sqrt{\sqrt{\left(1-\frac{\omega_0^2}{\omega^2}\right)^2+\left(2\frac{l}{\delta}\frac{\omega_0}{\omega}\right)^2}+\left(1-\frac{\omega_0^2}{\omega^2}\right)} \quad (26)$$

Using Eq. (26), we can illustrate penetration depth d as a function of δ/l and ω/ω_0. In Fig. 1a and 1b, d is normalized to l and δ, respectively. We can clearly see that our result converges to the following well-known limits.

$$\lim_{\omega \ll \omega_0} d = l \quad (27a)$$

$$\lim_{\omega \gg \omega_0} d = \delta \quad (27b)$$

Furthermore, we can see that when $\delta = l$, $d \approx l = \delta$.

CONCLUSION

To summarize, we study the intermediate regime between two well-studied limits: high frequency electromagnetic field penetrating a metal with small conductivity and a static field penetrating a superconductor. The former limit can be derived by consider Maxwell equations with Ohmic current. On the other hand, the later limit is obtained by focusing on the diamagnetic current.

By setting the electric current density as the total sum of both Ohmic and Diamagnetic currents, we derive the penetration depth in the intermediate regime. The penetration depth that include both contribution of Ohmic and diamagnetic currents depends on the ratio of δ/l and ω/ω_0 (see Eq. (26)). Figure 1 show that our result converges to the following well-known limits. When $\delta = l$, the penetration depth does not depend strongly to frequency.

REFERENCES

[1] D. J. Griffiths, *Introduction to electrodynamics; 4th ed.* Boston, MA: Pearson, 2013.
[2] "{XIII}. On electrical motions in a spherical conductor," *Philos. Trans. R. Soc. London*, vol. 174, pp. 519–549, 1883, doi: 10.1098/rstl.1883.0013.
[3] J. E. Hirsch, "On the dynamics of the Meissner effect," *Phys. Scr.*, vol. 91, no. 3, p. 35801, Jan. 2016, doi: 10.1088/0031-8949/91/3/035801.
[4] J. E. Hirsch, "Corrigendum: On the dynamics of the Meissner effect (2016Phys. Scr.91 035801)," *Phys. Scr.*, vol. 91, no. 9, p. 99501, 2016, doi: 10.1088/0031-8949/91/9/099501.
[5] W. F. Edwards, "Classical Derivation of the London Equations," *Phys. Rev. Lett.*, vol. 47, no. 26, pp. 1863–1866, 1981, doi: 10.1103/PhysRevLett.47.1863.
[6] B. Segall, L. L. Foldy, and R. W. Brown, "Comment on 'Classical Derivation of the London Equations,'" *Phys. Rev. Lett.*, vol. 49, no. 6, p. 417, 1982, doi: 10.1103/PhysRevLett.49.417.
[7] L. Banyai, "Mean-field Theory of the Meissner Effect in Bulk Revisited," Sep. 2020, doi: 10.20944/preprints202008.0653.v2.
[8] C. Kittel, "Introduction to solid state physics, John Wiley & Sons," *New York*, p. 402, 1996.
[9] J. E. Raynolds, B. A. Munk, J. B. Pryor, and R. J. Marhefka, "Ohmic loss in frequency-selective

surfaces," *J. Appl. Phys.*, vol. 93, no. 9, pp. 5346–5358, 2003, doi: 10.1063/1.1565189.

[10] B. A. Munk, *Frequency Selective Surfaces: Theory and Design*, 1st ed. Wiley-Interscience, 2000.

[11] A. B. Cahaya, "Paramagnetic and Diamagnetic Susceptibility of Infinite Quantum Well," *Al-Fiziya J. Mater. Sci. Geophys. Instrum. Theor. Phys.*, vol. 3, no. 2, pp. 61–67, 2020.

[12] A. B. Cahaya, A. O. Leon, M. R. Aliabad, and G. E. W. Bauer, "Equilibrium current vortices in rare-earth-doped simple metals," *arXiv:2006.13024*, 2020.

[13] G. A. Hallock and M. A. Meier, "Diamagnetic current measurements in a solid-state plasma," *Rev. Sci. Instrum.*, vol. 89, no. 8, p. 83505, 2018, doi: 10.1063/1.5029356.

[14] R. J. F. Berger, G. Monaco, and R. Zanasi, "On the topology of total and diamagnetic induced electronic currents in molecules," *J. Chem. Phys.*, vol. 152, no. 19, p. 194101, 2020, doi: 10.1063/5.0006992.

[15] R. Nevels and C.-S. Shin, "Lorenz, Lorentz, and the gauge," *{IEEE} Antennas Propag. Mag.*, vol. 43, no. 3, pp. 70–71, 2001, doi: 10.1109/74.934904.

Al-Fiziya
Journal of Material Sciences, Geophysics Instrumentation, and Theoretical Physics

Available online at:
Al-Fiziya: Journal of Materials Science, Geophysics, Instrumentation and Theoretical Physics
Website: http://journal.uinjkt.ac.id/index.php/al-fiziya
Vol.4 No.I Tahun 2021, 8 - 20

Application of the Acoustic Impedance (AI) Seismic Inversion and Multi-Attribute Method for Reservoir Characterization in Bonaparte Basin

Maurin Puspitasari[1,†], Ambran Hartono[1], Egie Wijaksono[2], Tati Zera[1]

[1]Physics Study Program, Faculty of Sciences and Technology, Syarif Hidayatullah State Islamic University Jakarta, Tangerang Selatan 15412, Indonesia
[2]Exploration Building 3 Research and Development Center for Oil and Gas Technology (PPPTMGB) LEMIGAS, Ciledug Raya Kavling 109 Cipulir St, Kebayoran Lama, South Jakarta City, Jakarta 12230, Indonesia

[†]maurinarin@gmail.com

Submitted: February 2021; Revised: April 2021; Approved: May 2021; Available Online: June 2021

Abstrak. Penelitian mengenai penerapan metode seismik inversi *acoustic impedance* (AI) dan *multi-attribute* telah dilakukan dengan tujuan untuk karakterisasi reservoir pada Cekungan *Bonaparte*. Pemodelan yang digunakan dalam metode seismik inversi *acoustic impedance* berupa *model based*. Sedangkan pada metode seismik *multi-attribute* menggunakan log porositas dengan menerapkan metode regresi linear serta menggunakan teknik *step-wise regression*. Berdasarkan hasil analisis sensitivitas dan analisis dengan metode seismik inversi *acoustic impedance*, zona reservoir dengan litologi batu pasir yang prospek akan hidrokarbon dan mengandung gas berada pada bagian Timur Laut - Barat Daya pada daerah penelitian yang berada di WCB-1, WCB-3 dan WCB-4 dengan rentang nilai *acoustic impedance* sebesar 4.800–13.000 (m/s)*(g/cc), dan nilai porositas yang dihasilkan dari analisis menggunakan metode seismik *multi-attribute* berada pada rentang 5–16% pada WCB-1 dan WCB-4, 2–10% pada WCB-3.

***Kata Kunci**: acoustic impedance, multi-attribute, model based, step-wise regression.*

Abstract. Research on the application of the acoustic impedance (AI) seismic inversion and multi-attribute method was conducted with the aim to characterize the reservoir in the Bonaparte Basin. Model-based is the modeling that is used in the acoustic impedance of the inversion seismic method. Meanwhile, log porosity is used in the multi-attribute seismic method that using the linear regression method with stepwise regression technique. Based on the result of sensitivity analysis between acoustic impedance, the reservoir zone in sandstone lithology that has the prospect of hydrocarbons containing gas is located in the Northeast-Southwest of the study area which in WCB-1, WCB-3, and WCB-4 well with the acoustic impedance values are in the range of 4.800-13.000 (m/s)*(g/cc), and the porosity values generated from the analysis using the multi-attribute seismic method are in the range of 5-16% in WCB-1 and WCB-4, 2-10% on WCB-3.

Keywords: *acoustic impedance, multi-attribute, model-based, stepwise regression.*

DOI : *10.15408/fiziya.v4i1.19788*

P-ISSN: 2621-0215, E-ISSN: 2621-489X

INTRODUCTION

In this 21st Century, human dependency on oil and natural gas is inccreasing. The natural energy is needed to fulfill daily household life that is dominated using oil and natural gas, which are the main strategy of energy commodity in Indonesia. This increasement need to be balanced with the development of technologies used in natural resources exploration which can be carried out through one of the geohpysics methods, namely the reflection seismic method in the form of acoustic impedance inversion and multi-attribute.

Reservoir is the main target in the exploration of oil and natural gas industry. Reservoirs can be defined as storage spaces in the form of pores or cavities beneath the surface of the earth located between mineral grains or in rock fractures that contain low-value porosity and oil and natural gas as well. Therefore, analysis of reservoir characterization is need to be done by using the seismic inversion acoustic impedance and multi-attribute method to determine the actual subsurface conditions, especially in the reservoir zone based on geological modeling in the form of constituent lithology and fluid content [1].

This research was conducted in the Plover Formation, the Bonaparte Basin, which is the main object of exploration and has the prospect of hydrocarbons and reservoir lithology content in the form of coarse-fine sandstone with alternating shale and claystone.

Regional Geology

This research is located in the Bonaparte Basin which is in the Northern part of the passive boundary of the Australian plate and belongs to the Graben Calder. The Bonaparte Basin is composed of several sub-basins and exposure areas that exist since the Paleozoic and Mesozoic periods. The formation of this basin is generally controlled by two main phases, namely the extension phase which occurred during the Paleozoic period, then followed by the compression phase occurred in the Triassic era, and finally encountered a phase of extension again in the Mesozoic period and peaked when Gondwana Land in the Middle Jurassic era split.

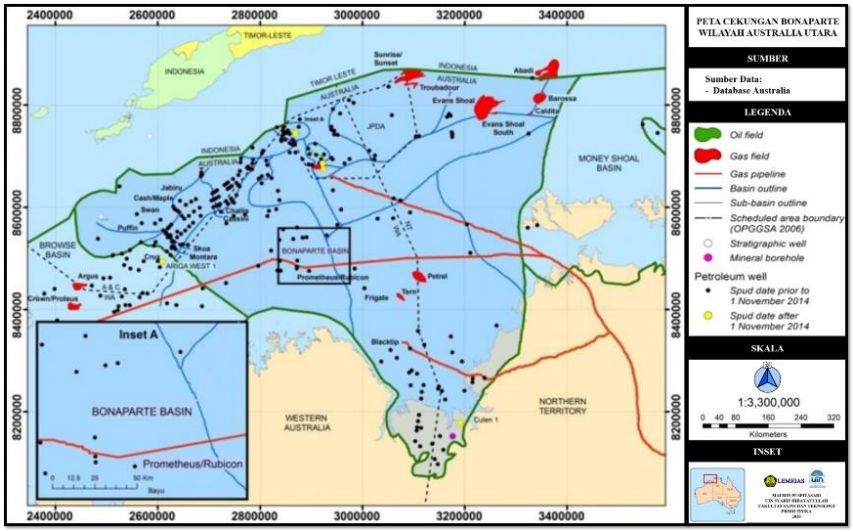

Figure 1. Map of Bonaparte Basin [4]

The Bonaparte Basin approximately has an area of ± 270.000 m^2, lies along the offshore stretching from Western Australia to the Timor Sea. This area consists of fluvial, siliciclastic, and carbonate sediments with a thickness of up to 15 kilometers. This basin is located in an area belongs to three countries: Australia, East Timor, and Indonesia. The Northern part of the basin is directly adjacent to the Timor Gap, while the Southern part is directly adjacent to the city of Darwin in Northern Australia, and the western part is bordered by the open seas of Indonesia and Australia. The map of Bonaparte Basin is shown in Figure 1 [2][3].

The Plover Formation consists of reservoir rocks that their structure are dominated by sandstone and alternatated with layers of clay and shale. This formation is divided into upper and lower Plover. The upper Plover is composed of the shallow seashore to the shore sequence sediments which are in the transgressive phase with its characteristics of either massive or layered sandstone of medium-coarse size, with more than 5 m thickness and inserted by clay rock. The lower Plover is composed of fluvio-deltaic sequence sediments which are in a regressive phase with its characteristics of a sandstone layer with medium-fine grains and thinner compared to the thickness of upper Plover and inserted by clay rock. The stratigraphy of target area at Bonaparte Basin is shown in Figure 2.

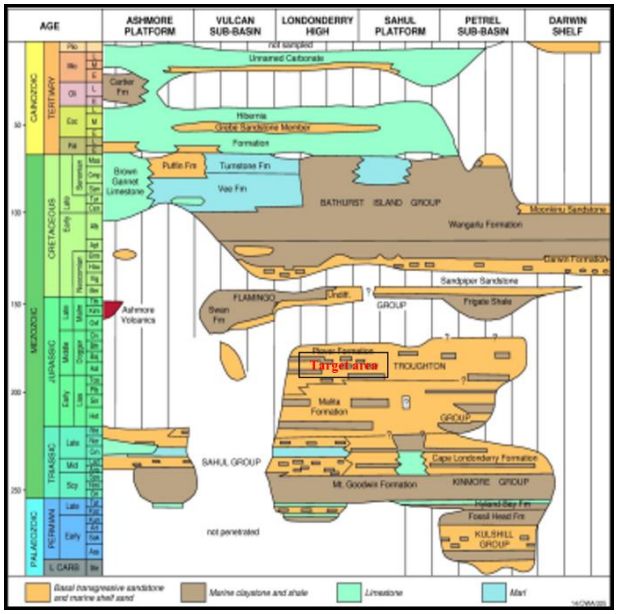

Figure 2. Bonaparte Basin Stratigraphy [5].

Seismic Reflection

Seismic reflection is one of the most important methods useful in supporting exploration in the oil and gas sector. Seismic reflection is used because this method provides more complete information and also able to explain and describe the subsurface structures more detail in three dimensions. To examine the subsurface of the earth with seismic reflection is used elastic sound waves. The elastic sound waves are emitted by a vibrating source in the form of dynamite explosions which are generally used during data acquisition on the land. Besides, there are also air guns, sparkers, and boomers which are generally used during data acquisition in the sea. The explosion produces waves that capable to penetrate rocks beneath the earth's surface. Later, it will be reflected in the form of a rock layer boundary to the earth's surface through its

reflector plane. Then, the recording device in the form of a geophone on the land and a hydrophone in the sea will receive and record the waves which are then will be reflected back to the surface. During propagation, seismic waves are reflected from the boundary between two recorded rock mediums. The big changes of acoustic impedance (AI) that occurred between the two rock mediums are directly related to these seismic waves reflection. The Survey of Seismic Reflection at Sea can be seen in Figure 3 [6] [7] [8].

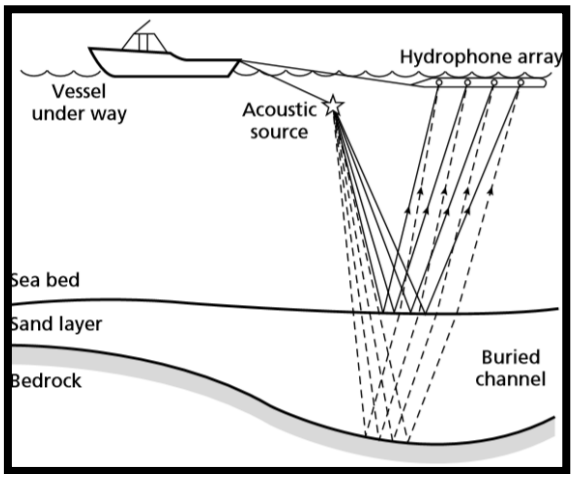

Figure 3. Seismic Reflection Survey at Sea [9].

Seismic Inversion

Seismic inversion is inverse modeling where its algorithmic modeling is a deconvolution between seismic recorded data and seismic waves, which then produces an acoustic impedance section related to the creation of a seismic section based on the shape of the earth. This method forms a geological model of the subsurface layer using two data in the form of seismic data as input and well data as control. This method involves mapping the physical structure and properties of the layers beneath the earth's surface by taking measurements on the earth's surface. The illustration of inversion seismic process is shown in Figure 4 [10].

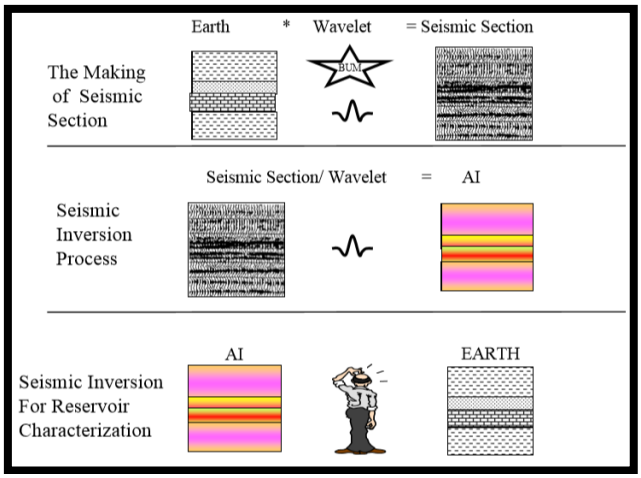

Figure 4. Illustration of Inversion Seismic Process [10].

The seismic inversion method is divided into two parts, namely the pre-stack inversion seismic and the post-stack inversion. The post-stack inversion is related to the

amplitude inversion which consists of three types of modeling: recursive (bandlimited), sparse-spike, and model-based. This study used the post-stack inversion seismic method by using model-based modeling [11].

Post-stack model-based inversion has a principle on describing the geological model. The geological model needs to be compared with the real seismic data. Then, it will be used to update the previous model and adjust it to the seismic data. The advantage of using this method is it does not inverse the seismic directly, but inverses the geological model.

Acoustic Impedance

Acoustic impedance is a nature of rocks which is influenced by porosity, depth, lithology type, fluid content, temperature, and pressure. Therefore, acoustic impedance is generally used as indicator of lithology, lithology mapping, porosity, seismic facies, flow mapping, hydrocarbons, as a means to quantify reservoir characters, formation of subsurface geological models. Acoustic impedance can transmit seismic waves on rocks [6] [12]. To define the acoustic impedance, use the equation below:

$$Z = AI = \rho \, . \, v, \tag{1}$$

where Z is the acoustic impedance (m/s)*(kg/m^3), ρ is the density (kg/m^3) and v is the velocity (m/s).

Multi-attribute Analysis

Multi-attribute analysis is a seismic method that using more than one attribute to estimate several properties of the physic of earth based on seismic data. This analysis is carried out to estimate the volume of log properties in all seismic volume locations by applying the relationships acquired from the results of log relationships and seismic data at the well locations. In reservoir characterization, statistics are used to predict the relationship between spatial variables at the desired value in a location where there is no sample data measurable.

Based on facts in nature, it is often that the measurement of variables which took place in an area that is close to each other has something in common. The alignment between two measurements will be inversely proportional to the distance, when the distance increased, the alignment of the measurements will be decreased. In fact, what is being analyzed is its seismic attribute data, not the seismic data, because it is more advantageous and able to increase the the prediction power, which is caused by several attributes that have non-linear characteristic [13].

In a multi-attribute analysis, there are three main sub-categories for identification, that is:

1). Extension of cokriging involved more than one secondary attribute to estimate the main parameter.
2). A covariance matrix is used to estimate parameters linearly based on the weighted input attributes.
3). Several seismic attributes are combined to estimate the required parameters by using Artificial Neutral Networks (ANNs) or non-linear techniques.

Linear regression method is used to determine the relationship between the target log and the attribute than show as crossplot. This method can be explained by equation:

$$y = a + bx. \tag{2}$$

Where y is the predicted value, a is the intercept that estimated by regression, b is coefficient that estimated by regression, and x is the predictor that present in data.

Stepwise regression technique is used to know how to determine the best attribute combinations that are most effective in predicting a log target with several steps. First, determine the single best attribute by trial and error and has the lowest prediction error and call this one attribute. Second, determine the best pair of attributes with the lowest prediction error and call this second attribute. Third, determine the best triplet of attributes with the lowest prediction error and call this third attribute. Carry on this process as long as desired.

METHODS

This research was conducted in the KP3T Field of the Exploration Building 3 Research and Development Center for Oil and Gas Technology (PPPTMGB) "LEMIGAS" located on Ciledug Raya Kav. 109 Cipulir St, Kebayoran Lama, South Jakarta City, Jakarta 12230. The research took place from February to August 2020. The research area was in the Bonaparte basin and using methods such as seismic inversion acoustic impedance and multi-attribute. The research data that were used are 3D Post-Stack Time Migration (PSTM) seismic data; 4 well data consisting of Gamma Ray log, Resistivity log, NPHI log, RHOB log, P-Wave log, PHIT log, and Sw log; marker data, and checkshot data.

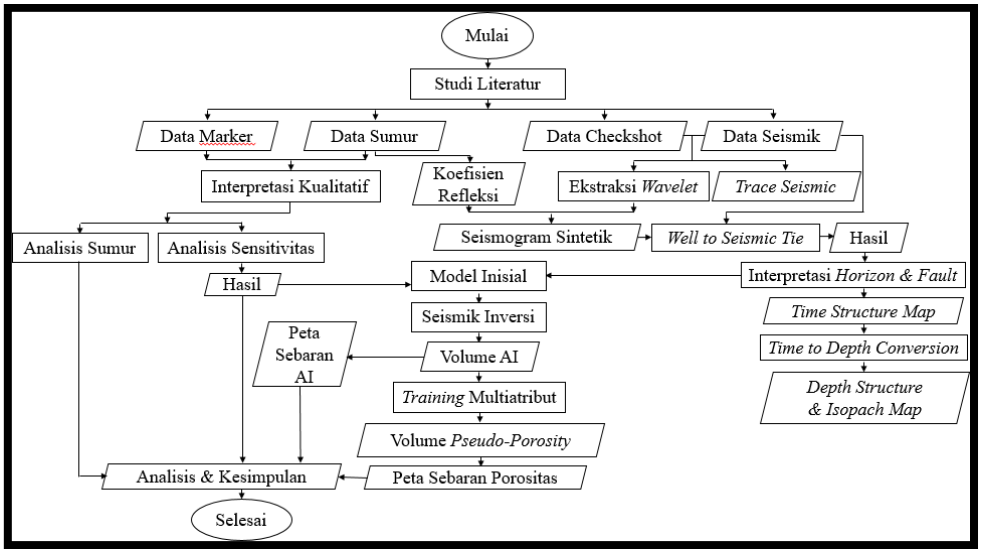

Figure 5. Research Flowchart

Data processing was carried out by using the CE8R4 version of Hampson Russell Software (HRS) for seismic and well data processing to AI inversion and multi-attribute to determine the characteristics of the reservoir zone in each well. Then, Petrel software is used for horizon interpretation by drawing continuity lines on the reflector plane and faults by drawing continuity lines on the fault plane, time to depth convertion, and create structure and surface map in the time and depth domain. The flow chart of well analysis and seismic inversion untill multi-attribute is shown in Figure 5.

Interpretation to determine the characteristics of the reservoir in this study was carried out by correlating the results of data processing, regional geological information of the research area, and information of the value in each log and the porosity table.

RESULT AND DISCUSSION

Target Zone Analysis Based on Well Log Correlation

The result of the quicklook analysis of the research target reservoir zone at WCB-3 well is shown in Figure 6. The display of the gamma ray log curve shows the presence of a permeable layer reservoir zone because it has low gamma ray values ranging from 10-60 API with lithology in the form of sandstone. Moreover, there is a cross over between the NPHI log and the RHOB log which indicates the presence of hydrocarbons containing fluid in the reservoir zone with a depth of 4.140 to 4.440 ft.

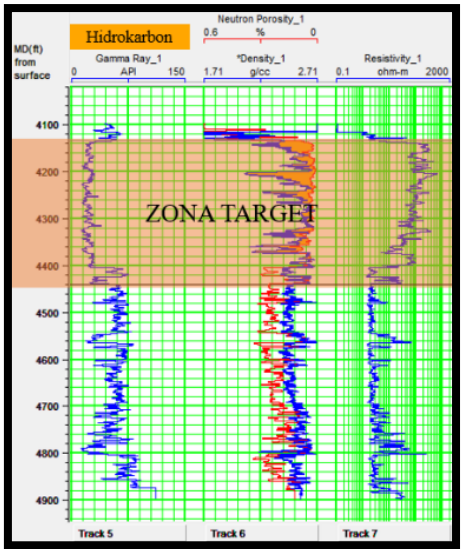

Figure 6. Quicklook Target Zone Analysis of WCB-3 Well

The response of LLD resistivity log is used to determine the fluid content, where the LLD resistivity log with high value and has more than 80 Ohm. This indicates that there is a fluid content in the form of gas in the target zone of WCB-3 well in the research area (Table 1) [14].

Table 1. Results of Target Zone Analysis Based on Well Log Correlation

Well	Gamma Ray (API)	Cross over NPHI & Density	Resistivity LLD (Ohm)	Depth (ft)
WCB-1	Low	Exist	>80 Ohm	3.910 – 4.220
WCB-2	Low	Doesn't Exist	<80 Ohm	4.300 – 4.575
WCB-3	Low	Exist	>80 Ohm	4.140 – 4.440
WCB-4	Low	Exist	>80 Ohm	4.170 – 4.490

Sensitivity Analysis

According to the results of the crossplot on the target zone which refers to regional geology is shown in Figure 7, the separation of lithology is divided into two zones: a zone that is composed of shale lithology with green colored and a zone that is composed of sandstone lithology with peach colored. This analysis is considered sensitive because it can separate the two lithologies well and determine the relationship between acoustic impedance and porosity which is inversely proportional.

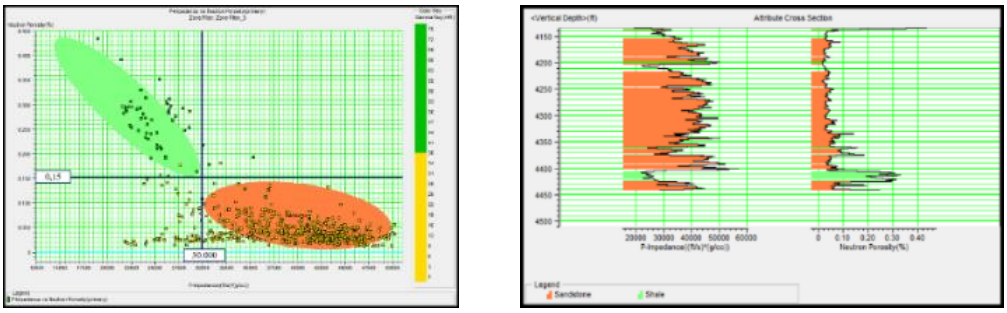

(a) (b)

Figure 7. (a) Crossplot Results on WCB-3, (b) Cross-Section View on WCB-3

Besides, cut-off or or acoustic impedance limitiation for both zones is 30.000 (ft/s)*(g/cc) and a porosity cut-off (NPHI) of 0,15. It can be inferred that the reservoir zone of the WCB-1, WCB-3, and WCB-4 wells are composed of sandstone lithology, while the WCB-2 reservoir zone is composed of sandstone lithology but dominated by shale inserts.

Well to Seismic Tie Analysis

According to the result analysis using wavelet ricker, the author argue that synthetic seismograms have similarities with seismic traces and have maximum correlation value and minimum time shift. This indicates that the result obtained from the well seismic tie process is quite good. Therefore, it helps in interpreting the horizon which is will be referred while picking. It can be seen that the TOP-X horizon in seismic data is at the peak, while the BASE-Y horizon is on the through (Table 2).

Table 2. Correlation of Well To Seismic Tie in Each Well

Number	Well	Correlation	Time Shift (ms)
1	WCB-1	0,939	0
2	WCB-2	0,810	0
3	WCB-3	0,802	0
4	WCB-4	0,914	0

Horizon and Fault Interpretation

Interpretation of the horizon is carried out by pulling the continuity of the seismic reflector based on the presence of the TOP-X and BASE-Y target zone markers that have been carried out in the well seismic tie as a reference. Meanwhile, fault interpretation is carried out by drawing a line on the fault plane based on regional geological information in the NE-WS (Northeast-Southwest) and shown in Figure 8.

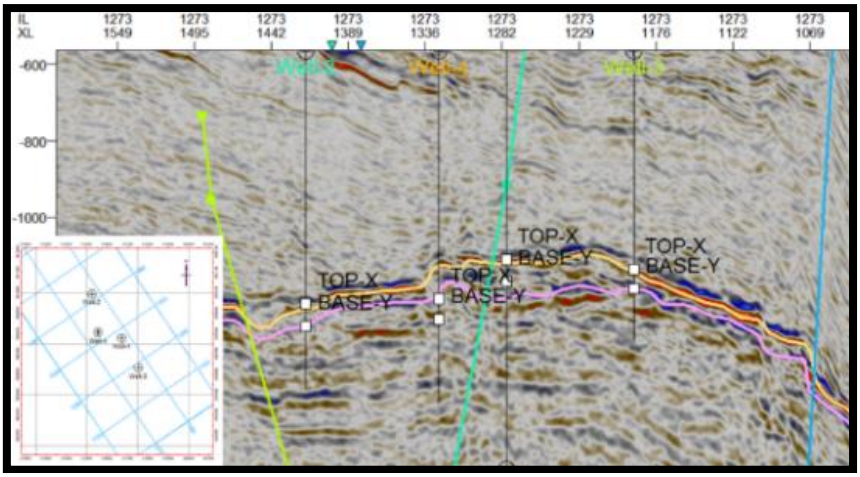

Figure 8. Display of Horizon and Fault Interpretation

Time and Depth Structure Map

The time structure map at the top and basement of the research target reservoir zone is used to determine how the structure condition is in the time domain. According to the time structure map in TOP-X and BASE-Y is shown in Figure 9, it can be seen that the reservoir zone is in one closure which is higher area compared to the surrounding area, and has domain time in the range of 1.200-1.400 ms.

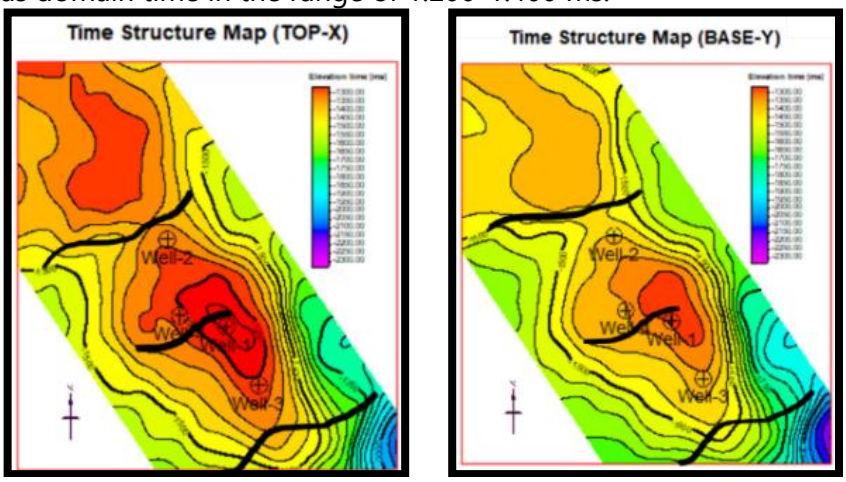

(a) (b)

Figure 9. Time Structure Map (a) Horizon TOP-X, (b) Horizon BASE-Y

Meanwhile, the depth structure map is used to determine the condition of the structure in the depth domain and it can be seen that the reservoir zone on both horizons is at one closure which is a higher area compared to the surrounding area and the depth structure map is shown in Figure 10.

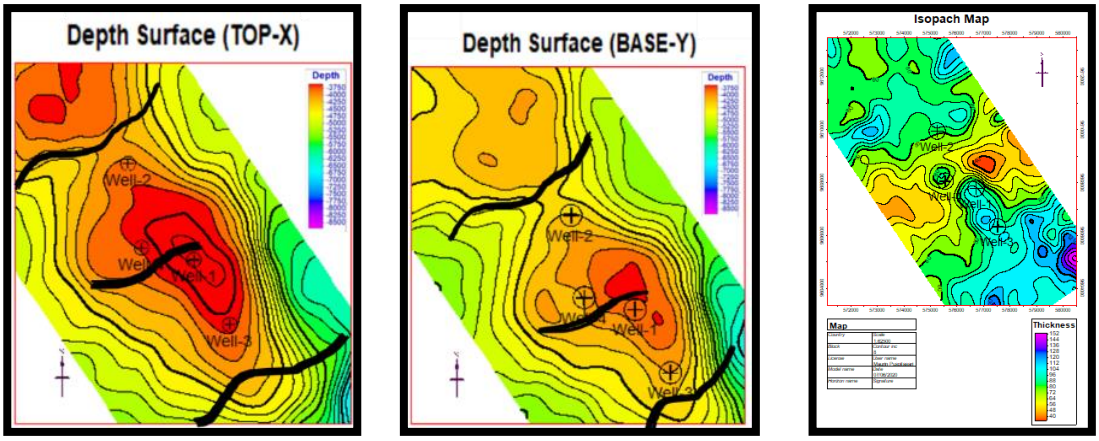

(a) (b) (c)

Figure 10. (a) Depth Structure Map of Horizon TOP-X, (b) Depth Structure Map of Horizon BASE-Y, (c) Thickness Map

Table 3. Depth and thickness domains for each well

Well	Depth Domain		Thickness
	TOP-X	BASE-Y	
WCB-1	3.500 ft	4.000 ft	88-104 m
WCB-2	3.750-4.000 ft	4.500 ft	72-88 m
WCB-3	3.500 ft		88-104 m
WCB-4		4.250 ft	72-104 m

Analysis of Acoustic Impedance Seismic Inversion

According to the results of the acoustic impedance inversion section in the form of a model-based, it can be inferred that the reservoir containing sandstone has an AI value in the range of 4.800 (m/s)*(g/cc) to 13.000 (m/s)*(g/cc) which marked in light green to dark blue. This is in accordance with the results of well log data calculations. After that, the slicing was carried out on the cross-section of the inversion to determine the lateral distribution pattern of AI values.

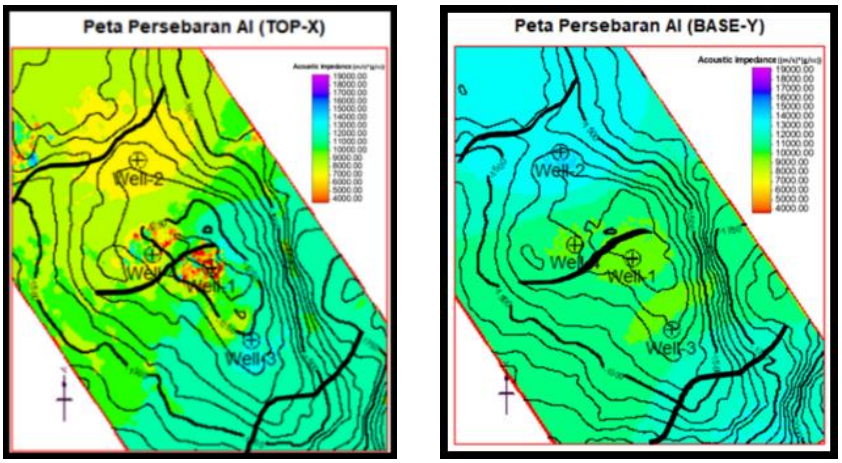

(a) (b)

Figure 11. Map of AI Distribution Display (a) Horizon TOP-X, (b) Horizon BASE-Y

According to the AI distribution map in Horizon TOP-X, the WCB-1 Reservoir Zone which is inline 1281, the AI values range from 4.800 (m/s)*(g/cc) to 7.000 (m/s)*(g/cc) marked in orange to yellow. The WCB-2 Reservoir Zone which is in inline 1281, has an AI value of 7.000 (m/s)*(g/cc) which is marked in yellow. Meanwhile, the WCB-3 Reservoir Zone which is in inline 1273, the AI value ranges from 11.000 (m/s)*(g/cc) to 13.000 (m/s)*(g/cc) which is marked in greenish blue until light blue. For the WCB-4 Reservoir Zone which is in inline 1237, the AI values range from 4.800 (m/s)*(g/cc) to 11.500 (m/s)*(g/cc) marked in orange to greenish blue.

According to the AI distribution map on Horizon BASE-Y, Reservoir Zone on WCB-1 and WCB-4, the AI value is 10.000 (m/s)*(g/cc) marked in green. While the WCB-2 Reservoir Zone, the AI value is 13.000 (m/s)*(g/cc) marked in blue. While the WCB-3 Reservoir Zone, the AI value is 11.000 (m/s)*(g/cc) marked in turquoise blue. The map of AI distribution is shown in Figure 11.

According to the AI distribution map on both horizons that are correlated with regional geological information, density log data, and the results of the sensitivity analysis, it can be inferred from reservoir zone in WCB-1 and WCB-4 that their constituent lithology are sandstone that is porous because it has a relatively low density when compared with the reservoir zone in other wells. Whereas in the WCB-2 reservoir zone, its constituent lithology is sandstone inserted by shale rock because it has a relatively large density value when compared to the WCB-1 and WCB-4 reservoir zones. Then, for the WCB-3 reservoir zone, its constituent lithology is compact sandstone because it has a large density value when compared to the reservoir zones in other wells.

Multi-attribute Analysis

According to the pseudo-porosity cross-section by applying the linear regression method and stepwise regression technique that using 10 attributes with 9 operators length, the author assume that there is an alignment between the color and the log porosity values contained in the well and the porosity log predicted in this analysis using 8 out of 10 existing attributes. This is caused by the increasement in validation error value and the validator curve in the ninth attribute which indicates overtraining. After that, the slice is made with a 4 ms window under the horizon to form a map porosity distribution in the research area.

According to the porosity distribution map in the both horizon is shown in Figure 12, the reservoir zone in WCB-1 and WCB-4 is a hydrocarbon prospect zone that has a porosity value in the range of 5% to 16%. Meanwhile, the WCB-3 reservoir zone which is a hydrocarbon prospect zone has a porosity value in the range of 2% to 10%. Then, WCB-2 which does not have hydrocarbon prospect has a porosity value that is in the range of 3% to 12%.

According to the porosity distribution map in the both horizons which is correlated with regional geological information, density log data, and the result of the sensitivity analysis, it can be seen that the WCB-1 and WCB-4 lithological reservoir zones are composed of sandstone that is porous because it has a relatively low density when compared with the reservoir zone in other wells. Whereas in the WCB-2 reservoir zone, its constituent lithology is sandstone inserted by shale rock because it has a relatively large density value when compared to the WCB-1 and WCB-4 reservoir zones. Then, for the WCB-3 reservoir zone, its constituent lithology is compact sandstone because it has a large density value when compared to the reservoir zones in other wells. Also, it can be

seen that the distribution of the reservoir in the study area leads to the Northeast-Southwest and is in one closure in an elevated area.

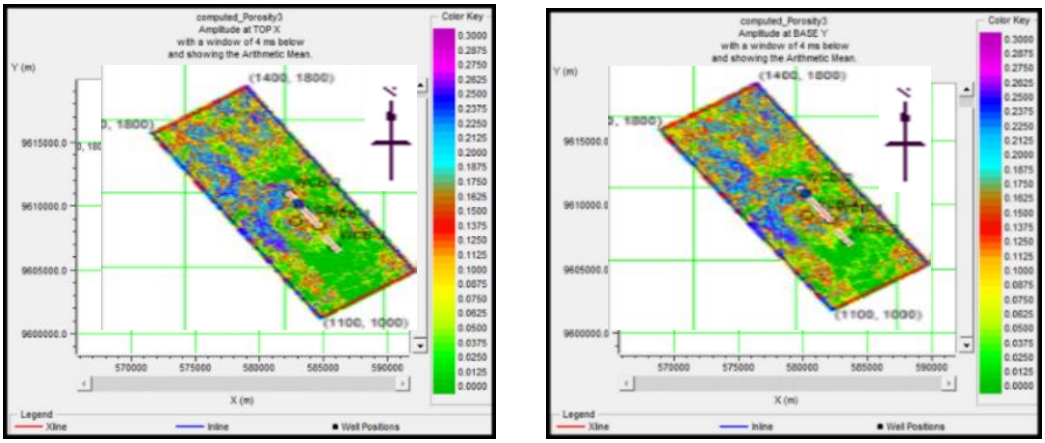

(a) (b)

Figure 12. Map of Porosity Distribution (a) Horizon TOP-X, (b) Horizon BASE-Y

By using the methods, both the acoustic impedance inversion seismic method and the multi-attribute seismic method, it can be inferred that the similiar distribution pattern or trend is obtained. Where the reservoir zone that has hydrocarbon prospects is in the Northeast-Southwest part with a relatively low acoustic impedance value and high porosity value obtained from multi-attribute analysis in shaft sandstone. Meanwhile, compact sandstone has a high acoustic impedance value and a relatively low porosity value. According to the porosity classification table, the resulting porosity values in the multi-attribute analysis in this study were classified into bad porosity in the reservoir that has <10% porosity value, but in some areas that has 10% to 16% and classified into good porosity with low acoustic impedance value has hydrocarbon prospect.

CONCLUSION

According to the results of research on the application of the acoustic impedance seismic inversion and multi-attribute method for reservoir characterization in the Bonaparte Basin, can be inferred as follows:

1. WCB-1, WCB-3 and WCB-4 wells in the research area are the locations that potentially become hydrocarbon reservoir zones.
2. The distribution of sandstone reservoirs that potentially contain gas hydrocarbons in this study is located in the Northeast-Southwest and is in high areas, and the characteristics of the reservoir based on the acoustic impedance value are in the range of 4.800 – 13.000 (m/s)*(g/cc) obtained by the seismic inversion acoustic impedance method.
3. The distribution of sandstone reservoirs that potentially contain gas hydrocarbons in this study is located in the Northeast-Southwest and is in high areaa, and the characteristics of the reservoirs WCB-1 and WCB-4 based on their porosity values are in the range of 5% to 16% while The WCB-3 reservoir is in the range of 2% to 10% obtained by the multi-attribute seismic method.

REFERENCES

[1] R. P. Koesoemadinata, 1980, *Geologi Minyak dan Gas Bumi,* Institut Teknologi Bandung, Bandung.
[2] S.J. Cadman, dan P.R Temple, 2003, *Bonaparte Basin, NT, WA, AC & JPDA, Australian Petroleum Accumulations Report 5, 2nd Edition,* Geoscience Australia, Canberra.
[3] P. Barber., P. Carter., T. Fraser., P. Baillie., dan K. Myers, 2003, *Paleozoic and Mesozoic Petroleum System in The Timor and Arafura Seas, Eastern Indonesia, Proceedings Indonesia Petroleum Association 29th,* Indonesia IPA03-G-169, Jakarta.
[4] *Peta Cekungan Bonaparte*, [Online]. Available: https://www.ga.gov.au/scientific-topics/energy/province-sedimentary-basin-geology/petroleum/acreagerelease/bonaparte. [Accessed: 16-Juli-2020].
[5] K.L. Earl, 2004, *The Petroleum System of The Bonaparte Basin,* Geoscience Australia, Canberra.
[6] D.A. Herron, 2011, *First Steps in Seismic Interpretation,* SEG, USA.
[7] W.A. Ashcroft, 2011, *A Petroleum Geologist's Guide to Seismic Reflection,* Wiley-Black Well, UK.
[8] M. E. Badley, 1987, *Practical Seismic Interpretation,* Prentice Hall, USA.
[9] P. Kearey., M. Brooks., dan I. Hill, 2002, *An Introduction to Geophysical Exploration Third Edition,* Blackwell Science, Berlin.
[10] S. Sukmono, 2002, *Seismic Inversion for Reservoir Characterization,* Departement of Geophysical Engineering, Institut Teknologi Bandung.
[11] B. H. Russel, 1988, *Introduction to Seismic Inversion Methods,* SEG Course Notes Series, USA.
[12] D. N. Sanjaya., D.D. Warnana., dan B.J. Sentosa, 2014, *Analisis Sifat Fisis Reservoar Menggunakan Metode Seismik Inversi Acoustic impedance (AI) dan Multi-attribute (Studi Kasus Lapangan F3), J. Sains dan Seni Pomits.,* vol. 3, no. 2.
[13] B. H. Russel., dan D. P. Hampson, 1997, *Multiattribute seismic analysis, The Leading Edge*, vol. 16, pp. 1439-1443.
[14] M. H Rider, 2000, *The Geological Interpretation of Well Logs Second Edition,* Rider-French Consulting Ltd, French.

Available online at:
Al-Fiziya: Journal of Materials Science, Geophysics, Instrumentation and Theoretical Physics
Website: http://journal.uinjkt.ac.id/index.php/al-fiziya
Vol.4 No.I Tahun 2021, 21-28

ANALYSIS OF MOISTURE CONTENT, CALORIFIC VALUE AND BURNING RATE OF CORNCOB AND KAPOK RANDU (*Ceiba pentranda*) SKIN BRIQUETTE

Anshori Huroeroh[1†], Sheilla Rully A[2], Hamdan Hadi Kusuma[1]

[1]Physics Education Department, Science and Technology Faculty, UIN Walisongo Semarang
[2]Physics Department, Science and Technology Faculty, UIN Walisongo Semarang

[†]Anshorihuroeroh@gmail.com

Submitted: February 2021; Revised: March 2021; Approved: April 2021; Available Online: June 2021

Abstrak. Penelitian ini telah dikaji nilai kadar air, nilai kalor, dan laju pembakaran briket kulit tongkol jagung dan kapuk randu (Ceiba pentranda). Pembuatan briket dilakukan dalam 5 tahap: Pertama, bahan utama tongkol dan kulit kapuk randu (Ceiba Pentranda) dijemur agar beratnya berkurang 20%. Kedua, karbonisasi bahan utama dengan suhu 400˚C selama 60 menit dengan furnace dan diayak. Ketiga, briket dipadatkan dengan komposisi kulit tongkol jagung dan kapuk randu (Ceiba Pentranda sebagai berikut A (100%: 0%), B (75%: 25%), C (50%: 50%), D (25 %: 75 %), E (0%: 100%) dengan 10% w/w tepung tapioka sebagai bahan pengikat. Keempat, jemur sampel briket dan oven pada suhu 100 ˚C selama 60 menit. Kelima, sampel diuji dengan bomb calorimeter. Hasil penelitian menunjukkan bahwa nilai kadar air tertinggi pada sampel E 3,33%, Nilai kalor tertinggi terdapat pada sampel E yaitu sebesar 6195,05 Cal/gram dan laju pembakaran tertinggi terdapat pada sampel D dengan nilai 0,0622 gram/menit.

Abstract. This research has studied the value of moisture content, calorific value, and the rate of burning of corncob skin briquettes and kapok kapok (Ceiba pentranda). The briquettes were produced in 5 steps: First, the main material for cobs and kapok randu (Ceiba Pentranda) skin is dried so that the weight is reduced by 20%. Second, the carbonization of the main materials with a temperature of 400˚C for 60 minutes with a furnace and sieved. Third, compressed briquettes with corncob and kapok randu (Ceiba Pentranda) skin composition in the following ratios of A (100%: 0%), B (75%: 25%), C (50%: 50%), D (25%: 75 %), E (0%: 100%) with 10% w/w tapioca starch as binder. Fourth, dried the briquette sample and roasted at a temperature of 100˚C for 60 minutes. Fifth, the samples were then characterized by bomb calorimeter. The results show that the highest moisture content value was in sample E 3,33%, the highest calorific value was in sample E which was 6195.05 Cal/grams, and the highest burning rate was found in sample D with the value was 0.0622 grams/minute.

Keywords: *Briquettes, Corncob, Kapok randu (Ceiba pentranda) skin, moisture content, calorific value, burning rate.*

DOI : *10.15408/fiziya.v4i1.19745*

P-ISSN: 2621-0215, E-ISSN: 2621-489X

INTRODUCTION

Energy is a basic need for humans. The use of energy is increasing every year, but the existence of energy sources is decreasing, so there is a need for new solutions to obtain renewable energy, such as implementing new energy conservation. Energy needs in Indonesia are generally obtained from mining products, where the supply is running low until one day it will run out. Data from the Ministry of Energy and Mineral Resources in 2018 states that the Indonesian state has 3.2 - 3.3 per barrel or 0.2% of world oil and gas reserves are only 15% of world gas reserves [1]. Based on these data, it shows that the availability of fuel oil in Indonesia is decreasing so that it has an impact on fuel price increases, therefore it is necessary to use other energy sources as alternative energy, one of which is the use of biomass.

Biomass is used as alternative energy, one of which is briquettes. Briquettes can be defined as a fuel that is solid and comes from the remaining organic material which has undergone a compression process with a certain compressive power. Briquettes can replace the use of firewood which is starting to increase in consumption and has the potential to destroy forest ecology. Briquettes are quite economical, have high, flavorless, durable, and can be made with easily available materials, for example, corn cobs and kapok randu (Ceiba Pentranda) skin [2]. Corn cobs as raw material are quite abundant, cheap, and renewable. Corn cobs contain 33% crude fiber, 44.9% cellulose and 33.3% lignin. From some of these ingredients, corn cobs can be used as raw material for charcoal briquettes [3]. While the kapok randu (*Ceiba pentranda*) skin has a supportive content for briquette raw materials including 50-69% Holocellulose, 23-36% cellulose, and 10-26% lignin [4].

The use of corn cobs for briquettes can increase the high calorific value [3]. According to Laily (2017) and Andi, et al. (2011) corn cob briquettes produce low ash content, high ash content causes low briquette quality. Corn cobs briquettes can produce a low water content of 6.01%. The low water content will result in the combustion rate, the higher the water content, the faster the briquettes will run out when burned [5][6]. Also, kapok randu (*Ceiba pentranda*) skin can be used as an ingredient for briquettes. According to Faizal, et al (2018) the raw material for kapok randu (*Ceiba pentranda*) skin can produce a calorific value that exceeds the Indonesian briquette standard, with a predetermined carbonization temperature of 400° -600° C [4]. In previous studies, making briquettes from a mixture of kapok randu (*Ceiba pentranda*) seeds and kapok randu (*Ceiba pentranda*) skin with a ratio of 50%: 50% with 30% starch adhesive resulted in a calorific value of 4981 Cal/g [7]. The production of biomass from kapok randu (*Ceiba pentranda*) skin with 10% starch adhesive also has a high calorific value of 6782 Cal/g and produces a fairly low water content [8].

Making briquettes cannot be done without adhesive, the use of adhesive is to increase the calorific value and burning time [9]. There are several kinds of adhesive, including starch adhesive, flour adhesive, sugar cane adhesive, adhesive, sodium silicate, and others. According to previous research, the starch adhesive will produce high-value briquettes in terms of density and ash content. In the research of Nasruddin and Risman (2011) 4% starch adhesive will produce a calorific value of 4552 Cal / g higher than sugar cane adhesive which produces 4485 Cal / g with the main ingredient of corn cobs and adhesive composition of 4% each. The use of a higher composition will result in a higher density and longer combustion process [6]. A study conducted by Unokoly, et al. (2016)

with the main ingredients of corn cobs and bamboo showed that variations in the composition of the adhesive produced a burning time value that was not too much different, including 10% adhesive burned in 123,10 minutes, 20% with 123,147 minutes and 30% with 123,363 minutes [2]. The use of the type and composition of the adhesive is an important factor in making briquettes.

This research was conducted by analyzing the calorific value and the rate of burning in the manufacture of briquettes from two materials, namely, corn cobs and kapok randu (Ceiba Pentranda) skin with starch adhesive. Of the two main ingredients, variations in the composition will be tested with 5 samples, namely Briquette A (100% pure corn cobs), Briquette B (corn cobs and kapok randu (Ceiba Pentranda) skin = 75%: 25%), Briquette C (corn cobs and kapok randu (Ceiba Pentranda) skin = 50%: 50%), Briquette D corncob and kapok randu (Ceiba Pentranda) skin = 25%: 75%), and Briquette E (100% pure kapok randu (Ceiba Pentranda) skin). This study aims to obtain the results of moisture content, heating value, and combustion rate following Indonesian briquette standards.

METHODOLOGY

The method used in this research is experimental. The making of briquettes through several steps including First, the main material for cobs and kapok randu (*Ceiba pentranda*) skin is dried in the sun for 3 days so that the weight of the ingredients is reduced by 20%. Second, the carbonization of the main material with a temperature of 400˚C for 60 minutes with a furnace and then sieved with a 50 mesh size. Third, compressed 6 grams of briquettes sample with the composition of corn cobs and kapok randu (*Ceiba pentranda*) skin with ratio A (100%: 0%), B (75%: 25%), C (50%: 50%), D (25%: 75%), E (0%: 100%) with 10% w/w of tapioca starch as a binder, and then pressed with a strength of 1,32 tons. Fourth, drying the briquette sample under the sun for 3 days (20 hours) and oven at 100˚C for 60 minutes. Fifth, characterized the sample for moisture content, calorific value, and burning rate.

Moisture Content

Determination of water content can be obtained using the Eq. (1).

$$MC(\%) = \frac{w_1 - w_2}{w_1} \times 100\%. \quad (1)$$

MC = Moisture Content
w_1 = Initial weight
w_2 = Weight after drying

Calorific Value

Calorific value was determined with bomb calorimeter. The equation of calorific value using Eq. (2).

$$CV\left(Cal/_g\right) = \frac{(\Delta T.W) - e_1 - e_2}{m}. \quad (2)$$

CV = Calorific Value
ΔT = $T_1 - T_2$

W = Benzoate acid value (2465,57 ˚C)
e_1 = Burnt wire x 2,3 Cal
e_2 = Ml titration x 1 Cal
m = Mass

Burning Rate

The burning rate is the ratio between the mass of the briquette burned with the duration of time. Materials with low density have a larger air cavity so that the amount of material burned is greater. The Eq. (3) and (4) used to determine the rate of combustion.

$$M_a = M_1 - M_{2.} \quad (3)$$

$$BR = \frac{M_a}{t}. \quad (4)$$

BR = Burning rate
M_a = Mass of the briquette burned
M_1 = Mass of Initial Briquette
M_2 = Mass of residual briquette
t = Duration of burning time

RESULT AND DISCUSSION

Moisture Content

Table 1 is the percentage of moisture content the briquette, showing that the briquettes with composition E have the highest moisture content of 3,33% and briquettes with composition B has the lowest moisture content of 2,45%. The moisture content that is still contained in the briquette is due to the water trapped in the particles of the main materials when drying cannot come out completely. Besides, the water trapped in the adhesive material used causes the water content in the briquettes to remain high. The water trapped in the briquette is due to the difficulty of evaporating some waters during the drying process because the outside has dried first and forms a strong bond [6]. The moisture content in the briquette is related to the initial ignition of the fuel. If the moisture content higher, so it will be more difficult to ignition the briquettes. Because it takes energy to evaporate the moisture in the briquette [10].

Table 1. Moisture Content of the Briquette

Sample	Moisture Content (%)
Sample A	3,11
Sample B	2,46
Sample C	2,52
Sample D	2,57
Sample E	3,33

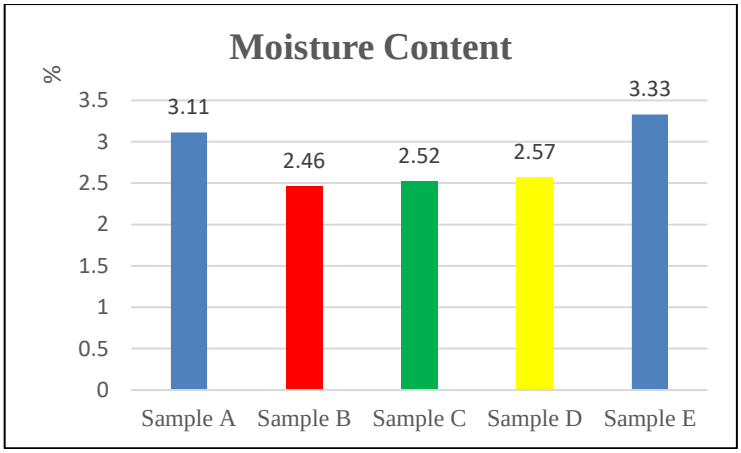

Figure 1. Moisture Content

Based on Figure 1, the water content value of sample B to sample E has increased based on the ratio of increasing the composition of kapok randu (*Ceiba pentranda*) skin. The difference in composition of each briquette sample will result in a different surface area of the briquette, so this has an effect on the absorption of moisture in the briquette. The adhesive composition and the type of adhesive also affect the moisture content value.

Table 2. Bio Briquette Quality (SNI 01-6235 2000)

No	Parameters (Units)	Value
1.	Inherent Moisture (%)	Max. 8
2.	Ash Content (%)	Max. 8
3.	Volatile Matter (%)	Max. 15
4.	Fixed Carbon (%)	Min. 77
5.	Calorific Value (Cal/gr)	Min. 5000

All samples made have met the national briquette standards that have been determined by Badan Standar Nasional (BSN) according to table 2 (Indonesian Briquette Standards) [11]. The results of this study with a moisture content of 2,45 -3,3%, were lower than previous studies. The value of the moisture content of this study is better than the previous research conducted by Faiz et al. (2015) regarding the combination of corn cobs and tea waste resulted in the lowest moisture content of 2,89% and the highest was 3,90% [12]. Research conducted by Lilih and Budi (2017) briquettes of corn cobs with variations and percentages of tapioca starch showed an average moisture content value of 4,58% [9].

Calorific Value

Figure 2 shows that the calorific value has decreased from sample A to sample D along with the decreasing composition of the corn cobs. The lowest calorific value was found in sample D, which is 3803,96 Cal/gram. The low calorific value can be caused by several factors, among others. First, the low temperature and time of carbonization resulted in a low heating value [3]. Second, the more adhesive is added, the more water and ash content that comes from the adhesive will result in high moisture content and ash content [9]. The calorific value determines the quality of the briquette. The higher the calorific value, the better the briquette quality. This is inversely proportional to the

moisture content and ash content, the higher the water content and the ash content, the less good the briquette quality.

Table 3. Calorific Value of the Briquette

Sample	Calorific Value (Cal/gram)
Sample A	4960,45
Sample B	4725,9
Sample C	4644,06
Sample D	3803,96
Sample E	6195,05

Figure 2 shows that the more corn cobs composition in the briquette making, the higher the calorific value is obtained. The results of this study are in line with the research conducted by Budi et al. (2016) with variations in the composition resulting in the highest calorific value at the composition of 100% corn cobs, namely 6078 Cal/gram. [3]. The highest calorific value is found in sample E which is 6195,05 Cal/gram. Research by Faizal, et al. (2018) obtained the highest calorific value results from the carbonization temperature. This is because the higher the carbonization temperature, the higher the carbon content in the briquette charcoal, while the water content will be lower so that it will produce a high calorific value in the briquette. [4]. The calorific value obtained from 5 samples according to the briquette standard according to SNI is only 1 sample that meets the standards, namely sample E (6195,05 Cal/gram).

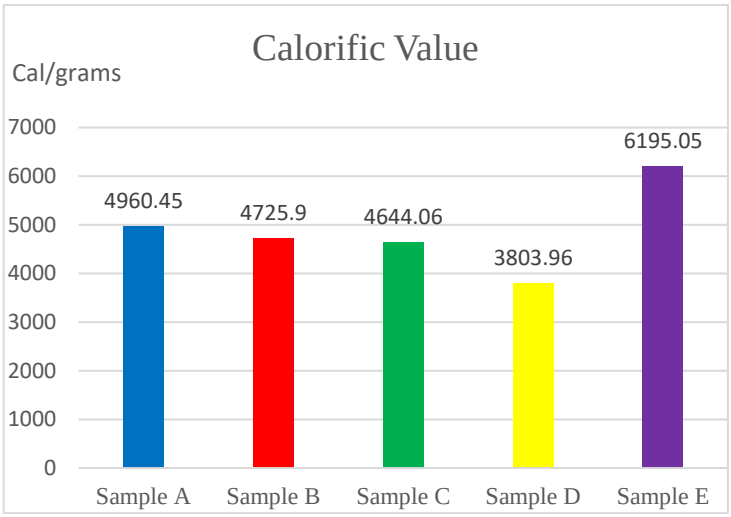

Figure 2. Calorific Value

Burning Rate

Based on Table 4 shows that the highest burning rate is in sample D. While the lowest burning rate of briquettes was found in sample E with a value of 0.0448 gram/minute. The less the composition of the corn cobs in making briquettes, the higher the value of the burning rate obtained. The high and low burning rate is influenced by the calorific value contained in the briquette [13]. It can be seen in Figure 3 that sample E has the lowest combustion rate but has the highest calorific value.

Table 4. Burning Rate of the Briquette

Sample	Burning Rate (gram/minute)
Sample A	0,0596
Sample B	0,0557
Sample C	0,0597
Sample D	0,0622
Sample E	0,0448

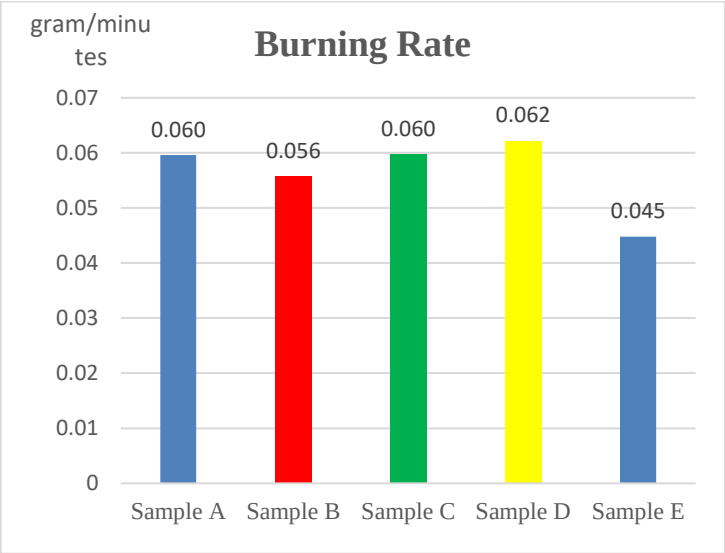

Figure 3. Burning Rate

Besides being influenced by the composition of the briquette material, the burning rate is also influenced by the presence of adhesive. The use of high adhesive concentrations results in high density, compressive strength and slows down the burning rate. The use of the type and composition of the adhesive in the manufacture of briquettes is an important factor in making briquettes [2].

CONCLUSIONS

Corn cobs and kapok randu (Ceiba Pentranda) skin can be used as ingredients for briquettes with a mixture of tapioca starch adhesive. The results show that the highest moisture content value in sample E is 3.3303% and the lowest moisture content in sample B (2.4587%). The highest calorific values are sample E which is 6195.05 Cal/gram. While the lowest calorific value was found in sample D which was 3803.96 Cal/gram. The lowest burning rate was found in sample E with a value was 0.0448 gram/minute. While the highest burning rate was found in sample D with the value was 0.0622 gram/minute.

REFERENCES

[1] Ditjem Etbk, *Kementrian Jendral Esdm*. 2018.

[2] P. Unukoly, V. N. Lawalata, And S. G. Sipahelut, "Kualitas Briket Arang Sebagai Bahan Bakar Alternatif Berbahan Baku Limbah Tongkol Jagung Dan Bambu," *J. Agroforestri*, Vol. Xi, No. 1, 2016.

[3] B. N. Widarti, P. Sihotang, And E. Sarwono, "Penggunaan Tongkol Jagung Akan Meningkatkan Nilai Kalor Pada Briket," *J. Integr. Proses*, Vol. 6, No. 1, Pp. 16–21, 2016.

[4] Muhammad Faizal, Achmad Daniel Rifky, And Irwanto Sanjaya, "Pembuatan Briket Dari Campuran Limbah Plastik Ldpe Dan Kulit Buah Kapok Randu (Ceiba Pentranda) Sebagai Energi Alternatif," *J. Tek. Kim.*, Vol. 24, No. 1, Pp. 8–16, 2018.

[5] L. N. Hamidah And A. Rahmayanti, "Optimasi Kualitas Briket Biomasa Padi Dan Tongkol Jagung Dengan Variasi Campuran Sebagai Bahan Bakar Alternatif," *J. Res. Technol.*, Vol. 3, No. 2, Pp. 70–79, 2017.

[6] Nasruddin And R. Affandy, "Karakteristik Briket Dari Tongkol Jagung Dengan Perekat Tetes Tebu Dan Kanji," *J. Din. Penelit. Ind.*, Vol. 22, No. 2, Pp. 1–10, 2011.

[7] Syamsuddin And Hasna, "Perbandingan Limbah Biji Kapok Randu (Ceiba Pentranda) Dengan Kulit Kapok Randu (Ceiba Pentranda) Sebagai Briket Arang Pengganti Bahan Bakar Rumah Tangga," *J. Sulolipu Media Komun. Sivitas Akad. Dan Masy.*, Vol. 19, No. 2, Pp. 276–281, 2019.

[8] D. A. Prayuda, "Analis Kualitas Pembakaran Biopelet Kulit Buah Kapok Randu (Ceiba Pentranda) Dengan Tepung Kanji," 2020.

[9] L. Sulistyaningkarti And B. Utami, "Pembuatan Briket Arang Dari Limbah Organik Tongkol Jagung Dengan Menggunakan Variasi Jenis Dan Persentase Perekat," *Jkpk (Jurnal Kim. Dan Pendidik. Kim.*, Vol. 2, No. 1, P. 43, 2017.

[10] I. Isa, "Briket Arang Dan Arang Aktif Dari Limbah Tongkol Jagung," 2012.

[11] Bsn, *Sni No. 01-6235-2000*. 2000.

[12] T. A. Faiz, L. A. Harahap, And S. B. Daulay, "Pemanfaatan Tongkol Jagung Dan Limbah Teh Sebagai Bahan Briket," *J. Rekayasa Pangan Dan Pertan.*, Vol. 4, No. 3, Pp. 427–432, 2015.

[13] I. I. Ikelle And O. S. Philip Ivoms, "Determination Of The Heating Ability Of Coal And Corn Cob Briquettes.," *Iosr J. Appl. Chem.*, Vol. 7, No. 2, Pp. 77–82, 2014.

Available online at:
Al-Fiziya: Journal of Materials Science, Geophysics, Instrumentation and Theoretical Physics
Website: http://journal.uinjkt.ac.id/index.php/al-fiziya
Vol.4 No.I Tahun 2021, 29-35

Water Level Detection System using Virtual Instrumentation for Monitoring Flood

Sabar[1,†], Dewi Maulidah Nur Anjani[2], Sastra Kusuma Wijaya[3]

[1]Electrical Engineering Study Program, Faculty of Production and Industrial Technology, Institut Teknologi Sumatera, Terusan Ryacudu Way Huwi Street, Lampung Selatan, 35365, Indonesia
[2]Physics Study Program, Faculty of Mathematics and Natural Sciences, Universitas Jendral Soedirman, Profesor DR. HR Boenyamin No.708, Central Java 53122, Indonesia
[3]Physics Departement, Faculty of Mathematics and Natural Sciences, *Universitas Indonesia, Jakarta, Indonesia*

[†]sabar@staff.itera.ac.id

Submitted: February 2021; Revised: March 2021; Approved: April 2021; Available Online: June 2021

Abstrak. Indonesia merupakan negara yang sering mengalami bencana, salah satunya adalah bencana banjir dimana setiap tahun pasti wilayah Indonesia mengalami kebanjiran. Oleh karena itu dibutuhkan suatu sistem instrumentasi yang mampu mendeteksi tingkat ketinggian air sebagai salah satu sistem pencegahan berupa sistem peringatan dan monitoring. Pada penelitian ini dibuat suatu rancangan pendeteksi ketinggian air pada suatu tempat dengan menggunakan Water level sensor berupa jenis funduino beserta buzzer module dihubungkan dengan arduino uno sebagai Master Control Unit (MCU) yang mengelola hasil pembacaan sensor menjadi data digital. Selanjutnya tampilan data berupa grafik dan numerik ditunjukkan pada display komputer (laptop) dengan menggunakan antarmuka pengguna grafis berbasis LabVIEW.

***Kata Kunci**: Arduino, Water Level Sensor, LabVIEW, Banjir*

Abstract. Indonesia is a country that often experiences disasters, one of which is the flood disaster where every year the territory of Indonesia is definitely flooded. Therefore we need an instrumentation system capable of detecting water level as a prevention system in the form of a warning and monitoring system. In this research, a water level detection system was designed using a water level sensor called *funduino* and a buzzer module was connected to Arduino Uno as a Master Control Unit (MCU) which manages the sensor readings into digital data. Furthermore, the data displayed in the form of graphs and numerics were shown on a computer display using LabVIEW based on graphical user interface.

***Keywords**: Arduino, Water Level Sensor, LabVIEW, Flooded*

DOI : *10.15408/fiziya.v4i1.19808*

P-ISSN: 2621-0215, E-ISSN: 2621-489X

INTRODUCTION

Indonesia is a country that has two seasons, namely the rainy and dry seasons. The rainy season that occurs ranges from October to March, while the dry season ranges from April to September. During the rainy season, the total volume has abundant amount of water, it will cause river water overflows and is unable to accommodate the excess volume of water. This condition is caused by the volume from body of water such as a river or lake that overflows or breaks a dam so that the water comes out of its natural limits. Floods often result in destructing to houses, roads, plants and other buildings [1]. If flood does not overcome using a good management of disaster mitigation system, this situation will cause the victim or casualties[2]. The previous studies said that ultrasonic sensors can be applied to measure the distance of water level. However, in this paper using a water level sensor to detect the water level, and buzeer modul is used as alarm system to give a signal that the water is full in tank. The system works when water reached the sensor and it would be detected.

Many experiments have been carried out using LabVIEW and Arduino, such as automated monitoring of the water level using LabVIEW to overcome water supply shortages.[3] The next research was implementation of the IoT based on system for the large-area management of the water distribution system using LabVIEW[4]. After that LabVIEW is used as user-friendly, computer-controlled instrumentation and data analysis technique that can revolutionize the way measurements are made, allowing theoretical predictions, simulations, and actual experimental results compared by almost instantaneously[5].

The proposed measurement system in this paper was designed by connecting the a water level sensor called *funduino* and a buzzer module was connected to Arduino Uno as a Master Control Unit (MCU) which manages the sensor readings into digital data. Furthermore, the data displayed in the form of graphs and numerics were shown on a computer display using LabVIEW based on graphical user interface. Then the data is processed and displayed on the front panel in LabVIEW as the results of monitoring the flood.

METHODOLOGY

In designing this virtual instrumentation system consists of several steps, namely the General Design of the System, Hardware, Software which contains an algorithm to carry out the measurement data acquisition process. The system design framework generally consists of several blocks that are interrelated and integrated with each other, so that they can work together to achieve goals. The system circuit diagram can be seen in Figure 1. In accordance with the flow of the circuit diagram the system consists of the Input, Process and Output sections. The input section consists of a water level sensor and a buzzer module, the process part consists of the Arduino Uno module, the GUI uses LabVIEW and the Output section consists of the computer as display monitoring.

Vol.4 No.I Tahun 2021, 29-35
P-ISSN: 2621-0215, E-ISSN: 2621-489X

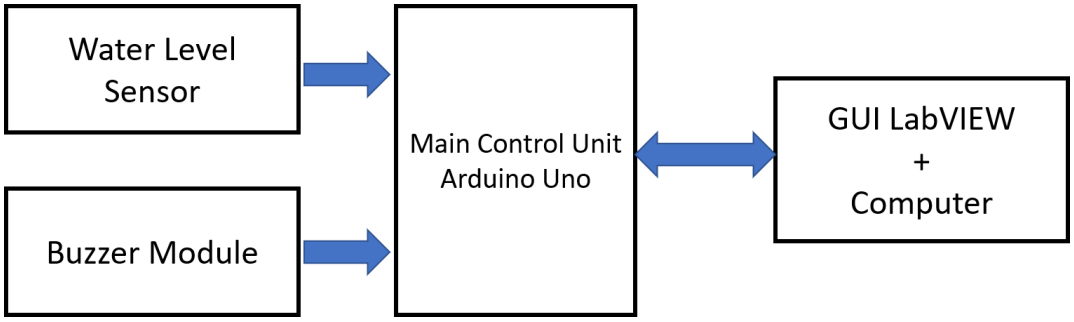

Figure 1. Flowchart Diagram Of Water Level Detection

RESULTS AND DISCUSSION

Hardware Design

Arduino Uno R3

Arduino Uno is a circuit board based on the ATmega328 microcontroller. This IC (integrated circuit) has 14 digital inputs / outputs (6 outputs for pulse width modulation (PWM), 6 analog inputs, a 16 MHz ceramic crystal resonator, universal serial bus (USB) connection, adapter socket, ICSP header pins, and buttons reset. This is what needed to support the microcontroller so that it is easily connected with a USB power cable or AC adapter power supply cable to DC or also battery [2].

Water Level Sensor (Funduino)

This sensor is designed to detect water that can be used widely, namely detecting rainfall levels, water levels. This sensor works with the digital I/O pin of the Arduino or can use it with an analog pin to detect the amount of contact induced by water between the ground and the sensor trace. This sensor can measure the water level by going through a series of parallels, it can also measure water droplets / water size. It is easy to convert the water size into an analog signal and output, the value is directly used in the program function to achieve the water level alarm function. The characteristics of this module have low power consumption and high sensitivity.

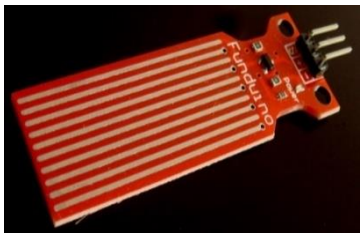

Figure 2. Water Level Sensor

Buzzer Module

A buzzer is an audio signal device, which may be mechanical, electromechanical, or piezoelectric. Use of the buffer as an alarm device, timer and confirm user input such as mouse clicks or key stokes. Buzzer is an integrated structure electronic transducer, DC power supply, widely used in computers, printers, copiers, alarm, electronic toys, automotive electronic equipment, telephones, timer and other electronic products for sound devices. Active buzzer 5V rated power can be directly connected to continuous

Vol.4 No.I Tahun 2021, 29-35
P-ISSN: 2621-0215, E-ISSN: 2621-489X

sound, this section is dedicated sensor expansion module and board in combination, can complete a simple circuit design, to "plug and play"

Figure 3. Buzzer Module

LabVIEW

LabVIEW is a graphical programming language for instrumentation, data acquisition, automation and control as well as communication. This software is a developer as well as the programming language C / C ++, FORTRAN or BASIC. LabVIEW program is designed to be machine independent so it can be transferred between operating systems. LabVIEW also has many tools for handling mathematical functions, graphical data visualization and input data objects that are commonly found in data analysis and data acquisition applications [6]. In this research uses LabVIEW 2017 of student version that obtained from www.ni.com. The first step, we can create account there. After that you can get free for student.

The system works when the water level sensor and buzzer module are connected to the Vcc pin with a 5V power supply and the black wire connected to the GND pin on the Arduino. Output of Water Level Sensor, namely the blue wire connected to Analog pin A5, while the green buzzer wire is connected to digital pin 13 on the Arduino. The USB port is connected to the Personal Computer to transmit the results from Arduino to LabVIEW and then perform data retrieval.

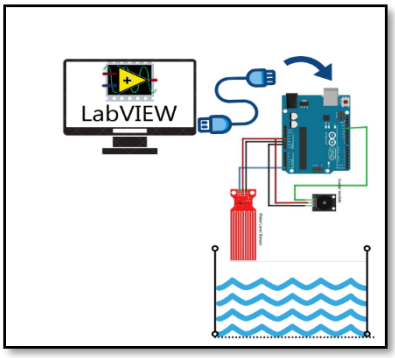

Figure 4. Block Diagram Proposed Design System

Software System Design

Figure 5 Block Circuit Diagram in LabVIEW software used for programming is LabVIEW and the programming package in VI Package Manager (VIPM), namely Maker-Hub. It is usually used for communication with Arduino, at the time of creating the program. The first step to build the program is by uploading the firmware to Arduino from the LINX Maker hub package on the LabVIEW tools then if the serial port has been read on the Maker Hub, that means the program can work properly. If it does not work

Vol.4 No.I Tahun 2021, 29-35
P-ISSN: 2621-0215, E-ISSN: 2621-489X

or the serial port has not been read, it is preferred to download the NI-VISA Driver first for running the program on LabVIEW when it is connected to Arduino and the serial port has been read on LabVIEW. Analog output The output from the water level sensor is displayed on the LabVIEW front panel in the form of a voltage value and displayed on the tank.

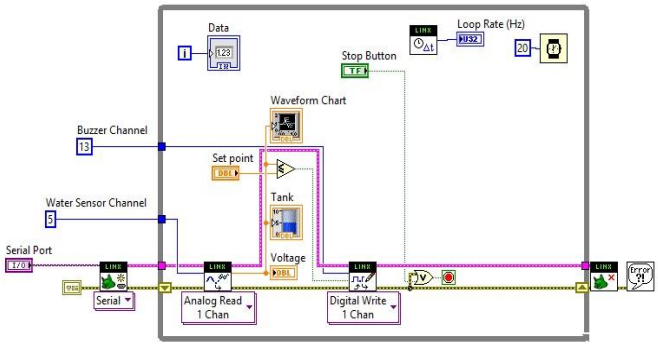

Figure 5. Block Circuit Diagram of LabVIEW

IMPLEMENTATION

Based on the results of implementation that the prototype had been successfully created using hardware contains of water level sensor and buzzer to connect the Arduino uno. The output from this sensor is s signal analog of Voltage sent by Arduino to LabVIEW for displaying. Then the data are processed and displayed on the front panel in LabVIEW as the results of monitoring the flood. We can see figure 5 displays of monitoring of front panel of LabVIEW. It seems simple but it is very friendly for user for monitoring the condition such as tank, dam, river, lake and so on.

The advantages of this system have water level sensor which are low power consumption and high sensitivity compared ultrasonic sensor that needs high power, low accuracy, not operate moving parts and temperature correction is required.[7]. According to the studies said that the best instrumentation system which can measure fast, non-destructively and environmentally-friendly[8]. From figure 6 can be seen the menu such as serial port shows that when com 3 is active, the system will work. And the loop rate has the function to obtain sampling the data. Then set poin has the function as the menu to adjust a limitation of voltage. We can see figure 6 design system that will become a virtual instrumentation of measurement.

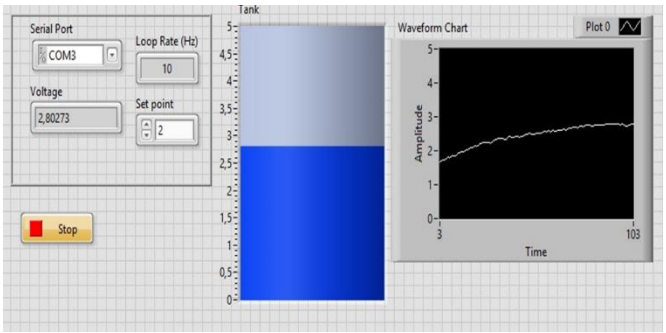

Figure 6. Displays Of Monitoring The Proposed Design System

Vol.4 No.I Tahun 2021, 29-35
P-ISSN: 2621-0215, E-ISSN: 2621-489X

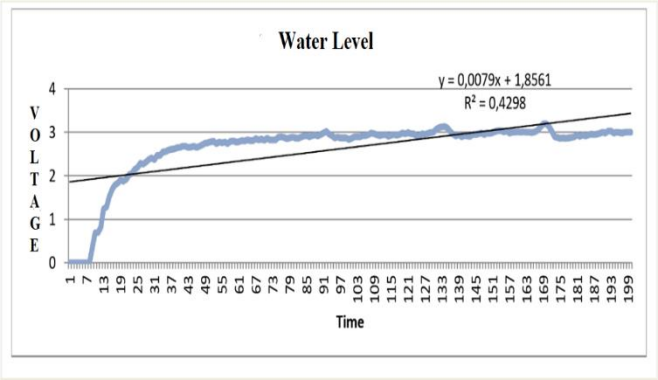

Figure 7. Graph Of Voltage Versus Volume Of Water Level

Figure 7 shows the value of voltage from sensor when water level reaches the sensor surface. The data obtained of the voltage value and the water level sensor when control panel is set the value set point 2, namely the maximum value of the sensor. So that the system will run to read the system and turn on the buzzer as the signal alarm of the system. When loop rate is set 10, it is mean the system will measure 10 data of voltage value every one second. When the volume of water increases and covers the sensor, the value of the voltage increases too. The graph of water level can be seen from the figure 7 that the output voltage shows linearity of system R2 = 0.4298, which means voltage value having small linearity. The reason happened because the instrumentation system design did not placed the sensor at good position when water would hit the sensor. This problem was different from paper by title system prediction salt content using hyperspectral imaging[9] which has high regression more or less 9.8 for prediction because in measurement needs calibration and comparation with other standard instruments.

CONCLUSION

According to data from the results of the design and testing water level detection system that has been carried out, it can be concluded that virtual instrumentation detection with water level Sensor and Buzzer module had worked well to detect water level but it was still having small linearity. The Arduino and LabVIEW program had been running according to the design, and it was able to control the entire work circuit and as an interface with LabVIEW. LabVIEW which used as a Graphical User Interface (GUI) was in accordance with the block diagram designed to be able to display voltage value and water level with graphs. Overall, water level detection system has worked quite well in accordance with the design that has been built. The next work will consider calibration and comparation several sensor for obtaining the objective measurement.

ACKNOWLEDGMENTS

We would like to thank Sastra Kusuma Wijaya, Ph.D is one of the lecturer in department of Physics, University of Indonesia supporting in writing this paper. He taught us the virtual instrumentation courses.

REFERENCES

[1] K. Saleh, Fauziyah, Hadi, And Freddy, "Sistem Pemantauan Ketinggian Permukaan Air Berbasis Mikrokontroler Basic Stamp-2 Menggunakan Memory Stick Sebagai Penyimpan Data," *Pros. Semirata Fmipa Univ. Lampung*, Pp. 511–515, 2013.

[2] Y. Al Hakim, "Pengembangan Automatic Water Level Recorder (Awlr) Untuk Flood Early Warning System (Fews)," *5th Urecol Proceeding*, No. February, Pp. 1602–1606, 2017.

[3] H. I. Azeez, N. Pimkumwong, And S.-C. Chen, "Automatic Water Level Control Using Labview," *Kurdistan J. Appl. Res.*, Vol. 2, No. 3, Pp. 369–375, 2017, Doi: 10.24017/Science.2017.3.28.

[4] Charles A Et All, "Iot Based Water Level Monitoring System Using Labview," *Int. J. Pure Appl. Math.*, Vol. 118, No. 20, Pp. 9–14, 2018.

[5] S. Sumathi And P. Surekha, *Labview Based Advanced Instrumentation Systems*. 2007.

[6] Y. P. Wijaya, "Simulasi Pengendalian Volume Tangki Menggunakan Labview Dan Arduino Uno," *J. Sains Dan Teknol. Ind.*, Vol. 13, No. 1, Pp. 79–82, 2016, [Online]. Available: Http://Ejournal.Uin-Suska.Ac.Id/Index.Php/Sitekin/Article/View/1293.

[7] G. Nikolov And B. Nikolova, "Virtual Techniques For Liquid Level Monitoring Using Differential Pressure Sensors," *Recent J.*, Vol. 9, No. September 2015, P. 2, 2008.

[8] Sabar, A. H. Saputro, And C. Imawan, "Moisture Content Prediction System Of Dried Sea Cucumber (Beche-De-Mer) Based On Visual Near-Infrared Imaging," *Proc. 2019 6th Int. Conf. Instrumentation, Control. Autom. Ica 2019*, No. August, Pp. 167–171, 2019, Doi: 10.1109/Ica.2019.8916705.

[9] Sabar, A. H. Saputro, And C. Imawan, "Salt Content Prediction System Of Dried Sea Cucumber (Beche-De-Mer) Based On Visual Near-Infrared Imaging," *2019 4th Asia-Pacific Conf. Intell. Robot Syst. Acirs 2019*, Pp. 245–249, 2019, Doi: 10.1109/Acirs.2019.8935953.

Available online at:
Al-Fiziya: Journal of Materials Science, Geophysics, Instrumentation and Theoretical Physics
Website: http://journal.uinjkt.ac.id/index.php/al-fiziya
Vol.4 No.I Tahun 2021, 36 – 44

2D Forward Modelling Geothermal Based on Gravity Data in South Solok Region, West Sumatra

Muhammad Nafian[1,†], Belista Gunawan[1], Nanda Ridki Permana[1]

[1]Physics Study Program, Faculty of Science and Technology, Syarif Hidayatullah State Islamic University Jakarta, Jalan. Ir. H. Djuanda No.95, Cempaka Putih, Ciputat, South Tangerang City, Banten 15412, Indonesia

[†]muhammad.nafian@uinjkt.ac.id

Submitted: March 2021; Revised: April 2021; Approved: May 2021; Available Online: June 2021

Abstrak. Panas bumi memiliki peranan penting sebagai bahan bakar alternatif karena merupakan sumber energi terbarukan, namun pemanfaatan di Indonesia belum dilakukan secara optimal. Salah satu daerah yang memiliki potensi energi panas bumi adalah Solok Selatan. Oleh karena itu, penelitian ini untuk mengetahui system panas bumi di Solok Selatan, Sumatera Barat dengan menggunakan metode gravitasi. Tahapan pengolahan data dimulau dari mendapatkan nilai CBA (*Complate Bouguer Anomaly*) dilanjutkan memisahkan anomaly menggunakan *Butterworth filter*, setelah itu dilakukan *forward modelling* 2D. Berdasarkan pemodelan pada peta CBA diduga memiliki prospek panas bumi karena terdapat nilai anomali rendah 7,9 mGal – 9,4 mGal. Sedangkan dari ke empat hasil slicing pemodelan yang diperoleh terdiri dari batuan lempung sebagai penutup, batu pasir, sebagai reservoir, granit sebgai batuan sumber panas bumi, dan lapisan berupa magma sebagai sumber panas bumi. Pemodelan anomali selanjutnya diperoleh penampang yang didominasi oleh batuan granit dengan nilai densitas 2500 kg/m^3 pada penampang AB dan nilai densitas 2550 kg/m^3 pada penampang CD.

Kata Kunci : *Forward Modelling*, system panas bumi, metode gravitasi

Abstract. Geothermal has an important role as an alternative fuel because it is a renewable energy source, but in use, it has not been done optimally. One of the areas that have the potential for geothermal energy is South Solok, West Sumatra. Therefore, this study was conducted to determine the geothermal system in the South Solok area, West Sumatra by using the gravity method. The data processing stage starts from calculating the value of the CBA (Complete Bouguer Anomaly), followed by anomalous separation using a Butterworth filter, after which 2D forward modelling is carried out. Based on the modelling on the CBA map, it is expected to have geothermal prospect because there are low anomalies of 7,9 mGal – 9,4 mGal. While the four slicing modelling results obtained consist of clay rock as a cover, sandstone as a reservoir, granite as a geothermal source rock, and a layer of magma as a geothermal source. The next anomaly modelling obtained a cross section dominated by granite with a density value of 2500 kg/m^3 on the AB section and a density value of 2550 kg/m^3 on the CD section.

Keywords: *Forward modelling, geothermal systems, gravity methods.*

DOI : *10.15408/fiziya.v4i1.20235*

P-ISSN: 2621-0215, E-ISSN: 2621-489X

INTRODUCTION

The dwindling reserves of fossil energy coupled with an unstable price that tends to continue to increase, and the evidence that fossil fuels are the cause of global warming and environmental damage, make Indonesia have to think rationally and innovatively to develop new and renewable energy. One of them is developing geothermal energy [1].

In the 2012-2021 PLN Electricity Supply Business Plan (RUPTL), it is stated that there are nearly 4,000 MW of geothermal power plant projects that will increase to around 6,348 MW in 2021. The amount of geothermal energy potential in Indonesia is estimated to be spread across 265 locations [1]. One of the areas that have the greatest potential for geothermal energy is South Solok, West Sumatra. With such a large geothermal energy potential and the government's efforts to prioritize the development of geothermal energy, it is hoped that the geothermal industry can develop in Indonesia, especially the South Solok area, West Sumatra.

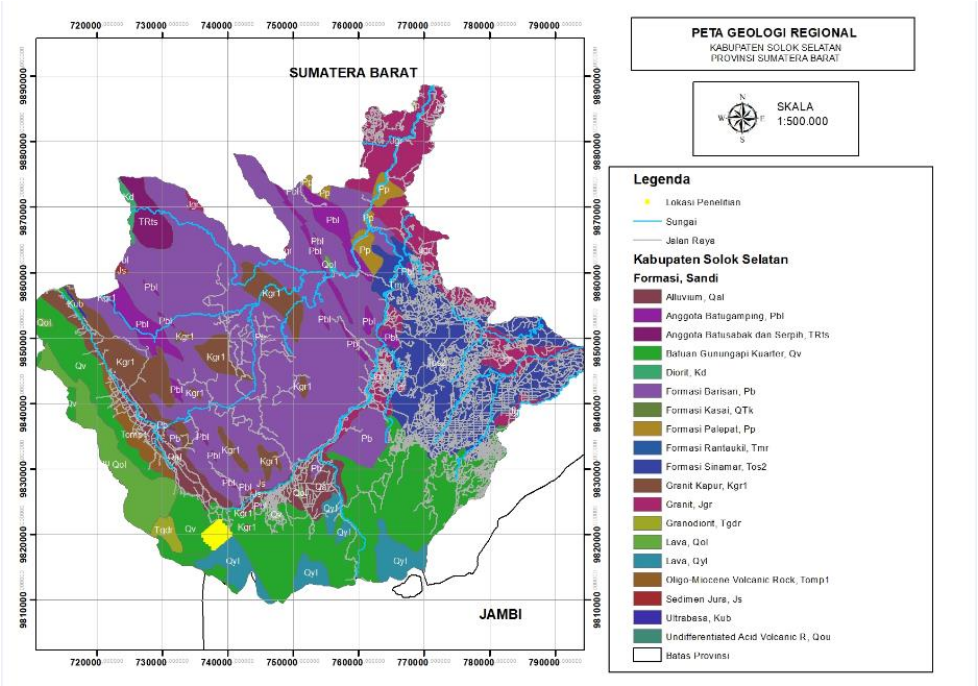

Figure 1. South Solok Regional Geological Map, West Sumatra

Geothermal energy comes from heat energy contained in the bowels of the earth and is generally associated with the existence of volcanoes. Water that comes from, among others, rain, will seep into the underground rock until it reaches the reservoir rock. This water is then heated by magma which is the main heat source so that it turns into hot water or hot steam (thermal fluid) which is then injected back into the reservoir through reinjection wells to maintain fluid and heat balance so that the geothermal system is sustainable [2].

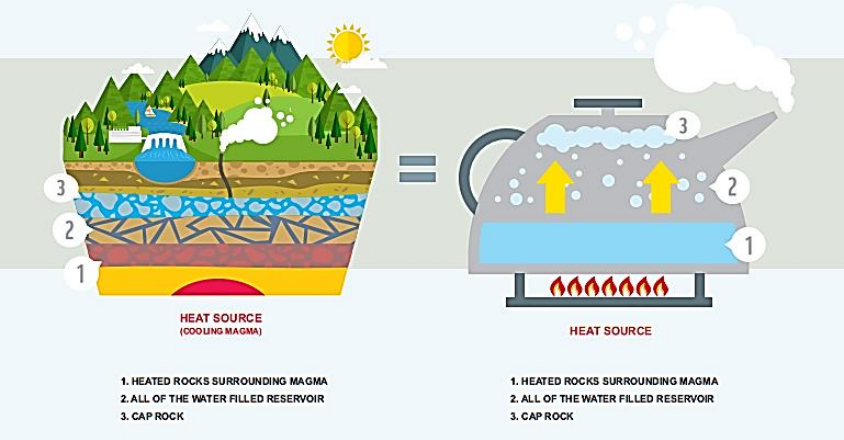

Figure 2. Geothermal Systems Work Like Boiling Water in a Kettle [3].

To see the geothermal system in a certain area requires a precise geophysical method, so that with its advantages it can provide information about subsurface structures and the causes of differences in the density of surrounding rocks. One of the geophysical methods that are suitable and commonly used for geothermal systems is the gravity method, because the gravity method has a pretty good picture for geothermal structures or complex structures through density parameters.

Principle of Gravity Method

The gravity method is included in the geophysical exploration method which is based on variations in mass density below the earth's surface. Gravitational field measurements result in a Complete Bouguer Anomaly, so to obtain gravitational data it is necessary to make corrections. Such as Bouguer correction and terrain correction.

Bouguer's correction is taken into account because there is a pull effect of the mass of rocks located in the stations and datum fields assuming they have infinite radius with a thickness of h (meters) and density of ρ (gr/cc). Bouguer correction value can be searched by the equation: [4]

$$BC = 2\pi g\rho h. \quad (1)$$

Terrain correction is performed because at the point of measurements there are topographic effects and differences elevations, such as hills and valleys around the measurement station, so that it is a correction to a simple Bouguer anomaly, in which the topography affects the reading of the due to its conservative gravity and reduced reading value than the state of Ideal [4].

Forward Modeling

Forward modeling states the process of calculating data that theoretically will be observed on the earth's surface if the price of certain subsurface model parameters is known. The calculation of the theoretical data uses mathematical equations derived from the physics concept that underlies the phenomenon being studied. In geophysical data modeling, a model is sought that produces a response that is suitable or fit with observational data or field data. Thus, the model can be considered to represent

Vol.4 No.I Tahun 2021, 36 – 44
P-ISSN: 2621-0215, E-ISSN: 2621-489X

subsurface conditions where the data is measured. In general, the forward modeling method takes a long time because it is not automatic like inversion modeling [5].

RESEARCH METHODS

This research was conducted from 26 February to 20 March 2021. The research location was in South Solok Regency, West Sumatra. Geographically, Solok Regency is currently located between 01°20'27" and 01°21'39" SL, 100°25'00" and 100°33'43" EL. Solok Regency has a varied topographic state, starting from highlands to relatively low in the northern with altitudes start from 100 meters until1,000 meters above sea level [6].

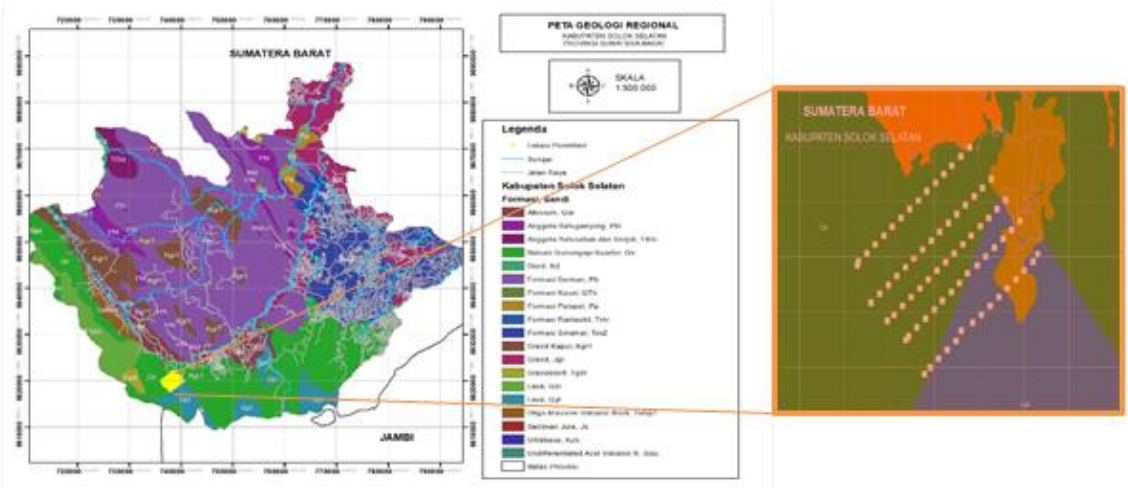

Figure 3. Research Survey Map.

The gravity data for the South Solok region is taken from Topex satellite data with a total of 100 data based on areas that are suspected of having geothermal potential, data from the Topex satellite is in the form of FAA (Free Air Anomaly) data and supporting data in the form of regional geological data made with Arcgis 10.3 software.

The gravity data processing stage requires some software to obtain the CBA (Complete Bouguer Anomaly) value, CBA contour maps, and anomaly separation using the Butterworth filter method. Anomaly separation is done using the Butterworth filter because this filter is very easy to do. In selecting regional and residual cut off zones in Oasis Montaj software, determining the intersection point of residual anomalies, and forward modeling of 2D geothermal systems without using topographic data. For more details see the flow chart below.

Vol.4 No.I Tahun 2021, 36 – 44
P-ISSN: 2621-0215, E-ISSN: 2621-489X

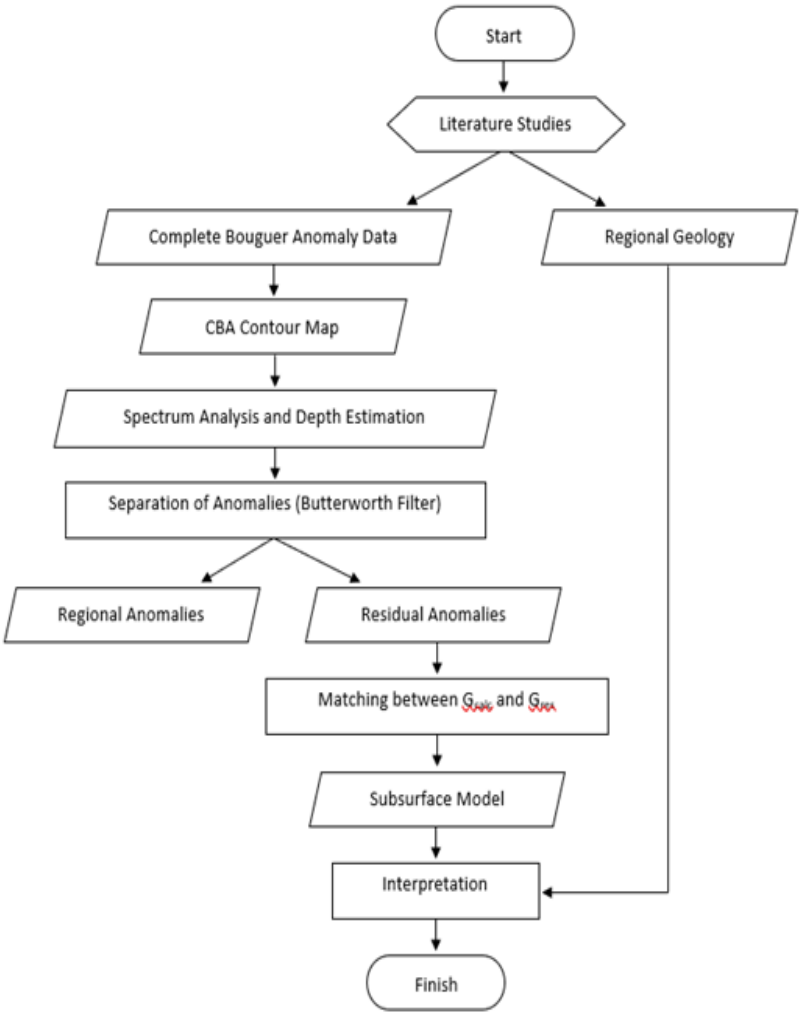

Figure 4. Research Flowchart.

RESULTS AND DISCUSSION

In data processing, after correcting the gravity value, the CBA (Complete Bouguer Anomaly) value is obtained. The CBA map shows that the anomalies generated in the data correlate well with the topography of the study area. Based on Newton's gravitational acceleration equation, shows that the value of gravity is proportional to the density of the rock beneath the surface. Therefore, the high gravity anomaly is proportional to the density of the region. Vice versa, low gravity anomaly shows a lower area density [7].

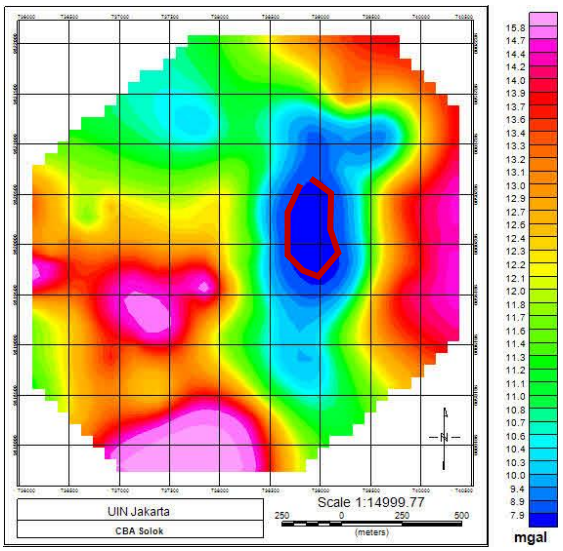

Figure 5. Complete Bouguer Anomaly Map.

Based on the CBA contour map, it can be seen that there are three gravitational anomaly patterns in the South Solok area, West Sumatra. The first anomaly pattern is a low anomaly with a range of values ranging from 7.9 mGal - 10.8 mGal. The second anomaly pattern is a moderate anomaly of 11.0 mGal - 13.3 mGal. The third anomaly pattern is a high anomaly of 13.4 mGal - 15.8 mGal. In this case, the target of the study was a low anomaly start from 7.9 mGal - 9.4 mGal which was marked in dark blue.

Complete Bouguer anomaly consists of residual anomalies and regional anomalies. Therefore, it is necessary to separate the two anomalies. The first step to take is to analyze the spectrum energy to obtain the anomaly depth value.

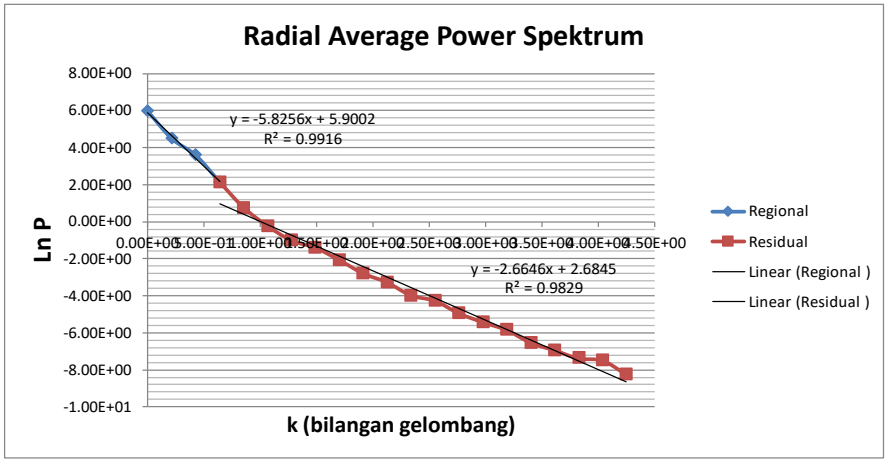

Figure 6. Radially Averaged Power Spectrum.

Based on the RAPS curve, the blue color shows a regional anomaly that can be seen from the presence of 4 observation points with the line equation y = -5.8256x + 5.9002. Because the shape is still in a gradient (in units of km), it must be converted into meters first so that it becomes -5825.6 m, then a calculation of -5825.6 / 4π is used so that the depth of the regional anomaly obtained is -463.8 m. While the red color shows the residual anomaly which can be seen from the existence of 18 observation points

Vol.4 No.I Tahun 2021, 36 – 44
P-ISSN: 2621-0215, E-ISSN: 2621-489X

with the line equation y = -2.6646x + 2.6845. With the same process as the previous anomaly, the residual anomaly depth obtained was -212.1 m because it appears that the residual depth limit is 212.1 m, a 2D model will be made based on the residual depth of 212.1 m.

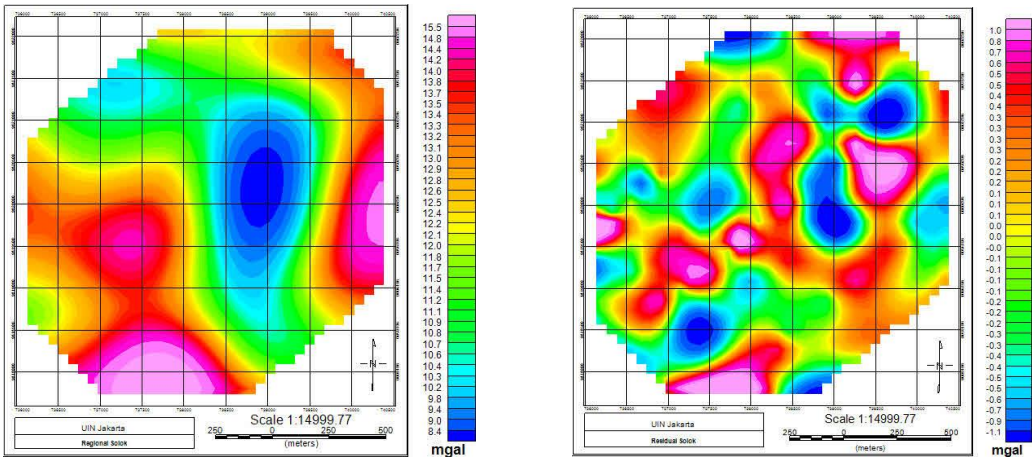

(a) (b)

Figure 7. (a) Regional Anomaly Map, and (b) Residual Anomaly Map.

The anomaly depth value is then depicted on a map through a filtering process using a Butterworth filter, which is one of the most commonly used frequency domain filters. As seen from Figure 7.a and Figure 7.b, it is clear that the difference in the residual anomaly map is rough due to the shallow location of the rocks with a value range of -1.1 - 1.0 mGal, while the regional anomaly map is smooth due to the deep location of the rocks. with a value range of 8.4 - 15.5 mGal. The regional anomaly map is almost the same as the CBA contour map because the regional anomaly value is much higher than the residual anomaly. Also, because the location of the regional anomaly is deeper and the rock density is high or compact, it will have more influence on the value of gravity.

Quantitative interpretation is done by making a model to describe the subsurface structure from the resulting gravitational anomaly profile. Modeling can be said to be correct or appropriate if the observation profile model is the same as the actual profile model which is indicated by the magnitude of the error value. The smaller the error value, the more accurate the model that has been made [8].

In this study, the residual anomaly map is sliced along a certain path into two parts. This results in two slicing sections of AB in the residual anomaly sliced from northwest to southeast (Figure 8.a) and CD slicing on residual anomaly from southwest to northeast (Figure 9.a). 2D modeling was made from each slicing, so that the geothermal system of Solok Selatan, West Sumatra can be seen.

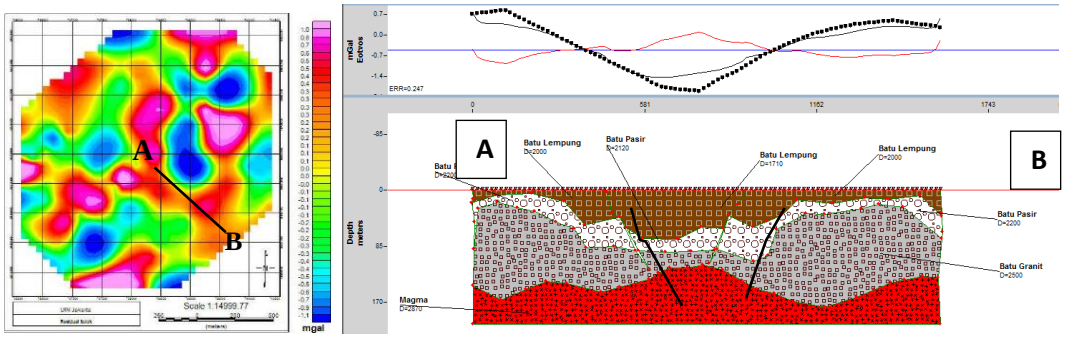

(a) (b)

Figure 8. (a) Slicing AB Residual Anomalies, and (b) 2D Modeling of AB Sections.

Figure 8.b is a cross-section of AB which consists of four layers. The first layer is marked with a brown color which is thought to have a depth of 0 m - 67 m and a density value of 1710 kg/m^3 and 2000 kg/m^3. This layer contains clay rock which is interpreted as stamp rock because it functions as a reservoir cover to prevent the release of geothermal fluids. Clay rocks also have low porosity and permeability, causing fractures that extend to the second layer due to the compressive force around the rock. The second layer is marked with a white color which is thought to have a depth of 20 m - 90 m. This layer contains sandstone as a subsurface reservoir with density values of 2120 kg/m^3 and 2200 kg/m^3. The third layer is marked in gray color which is thought to have a depth of 35 m - 172 m. This layer contains granite rock that is heated from magma, resulting in hot steam with a density value of 2500 kg/m^3. The fourth layer is marked in red which is thought to have a depth of 100 m - 200 m with a density value of 2870 kg/m^3. This layer is a source of geothermal energy because it contains a very hot liquid magma from the melting of rocks in the asthenosphere.

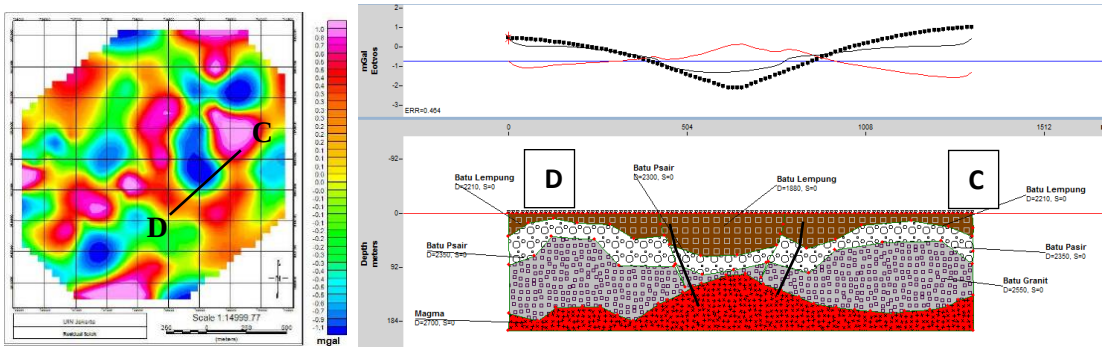

(a) (b)

Figure 9. (a) Slicing AB Residual Anomalies, and (b) 2D Modeling of CD Sections.

Based on the modeling drawings, the CD section is not much different from the AB cross sectional modeling which consists of four layers. The first layer is marked with a brown color which is thought to contain clay rock, has a depth of 0 m - 68 m with a density value of 1880 kg/m^3 and 2210 kg/m^3. The second layer is marked with a white color which is thought to contain sandstone and has a depth of 23 m - 95 m with a density value of 2350 kg/m^3. The third layer is marked with a gray color which is thought to contain granite and has a depth of 50 m - 182 m with a density value of 2550 kg/m^3. The fourth layer is marked in red, which is thought to have magma as a

source of geothermal energy and has a depth of 92 m - 200 m with a density value of 2700 kg/m^3.

Geothermal resources in the subsurface building of the South Solok area, West Sumatra is quite customary, because the area is composed of volcanic rocks and lava flows coming from Mount Kerinci. The water heat source will melt, then the hydrothermal fluid will move above its surface at a temperature that continues to increase and can be utilized in hot air bath attractions or so on.

CONCLUSION

Based on the results of research conducted with the gravity method in the South Solok area, West Sumatra, it can be concluded that:

1. Qualitative interpretation interprets the Complete Bouguer Anomaly map which is divided into three anomaly patterns. A low anomaly pattern with a value range of 7.9 mGal - 10.8 mGal, a moderate anomaly pattern of 11.0 mGal - 13.3 mGal, and a high anomaly pattern of 13.4 mGal - 15.8 mGal. From the map CBA, it appears that anomalies are dominating beneath the earth's surface. However, in this case, the target of the study is a low anomaly with a value range of 7.9 mGal - 9.4 mGal which is marked in dark blue which is thought to be a geothermal prospect area.
2. The quantitative interpretation produces 2D modeling on the anomaly cross sections AB and CD with the same number of layers, namely four. Starting from the first layer consisting of clay rock as a cap rock, sandstone as a reservoir, granite as rock heated by a heat source, and the last layer in the form of magma as a heat source. The anomaly modeling of these two sections is dominated by granite rock with a density value of 2500 kg/m^3 for the AB section and 2550 kg/m^3 for the CD section.

REFERENCES

[1] Ermawati. T, and N. D Siwage. 2014. "Policy Analysis of Geothermal Energy Development in Indonesia". Jakarta: Lipi Press.
[2] Geothermal Directorate. 2018. "Doing Business in Geothermal". Jakarta: Ministry of Energy and Mineral Resources.
[3] Suhud. M, et al. 2015. "Geothermal Training Module for Civil Society Organizations". WWF Indonesia: PT. Maginate Kreasindo.
[4] Maulana, A. D and Prasetyo, D. A. 2019. "Mathematical Analysis on Bouguer Correction and Correction of Topex Satellite Gravitational Data Field in Determining Geological Conditions of Palu Koro Fault Case Study, Central Sulawesi". Geoscience Journal, Vol. 5, No. 3, pp. 91-100.
[5] G. Hendra. 2009. "Introduction to Geophysical Inversion Modeling". Bandung: CV. Bhumi Printing.
[6] Solok Regency Office. 2018. "Profile of Solok Regency". Jakarta: RPIJM - Integrated Plan and Medium Term Infrastructure Program.
[7] Permana, N. R. 2020. "Mapping of Basic Rock Structure Using Energy Spectral Analysis Method - Multi Widow Test (Esa - Mwt) Gravity Data in Sakala Sub Basin". Jakarta: UIN Syarif Hidayatullah Jakarta.
[8] Ilmi, S, et al. 2014. "Subsurface Interpretation of Representative Geothermal Systems and Cranes Based on Gravity Data". Youngster Physics Journal, Vol. 3, No. 2, pp. 165-170.

Available online at:
Al-Fiziya: Journal of Materials Science, Geophysics, Instrumentation and Theoretical Physics
Website: http://journal.uinjkt.ac.id/index.php/al-fiziya
Vol.4 No. I Tahun 2021, 45 – 51

Investigation of Thermal Properties of Half-Heusler Alloy FeVZ (Z= As, P, Sb) within Density Functional Theory

Anugrah Azhar[1,†]

[1]Physics Study Program, Faculty of Sciences and Technology, Syarif Hidayatullah State Islamic University Jakarta, Tangerang Selatan 15412, Indonesia

[†]anugrahazhar@uinjkt.ac.id

Submitted: February 2021; Revised: March 2021; Approved: April 2021; Available Online: June 2021

Abstrak. Figure of merit (ZT) memegang peran penting dalam material termoelektrik yang menunjukkan efisiensi dari sebuah devais termoelektrik (TE). Semakin tinggi nilai ZT, semakin tinggi pula efisiensi yang akan diperoleh sebuah devais TE. Salah satu sub-kelas material yang memiliki potensi tinggi untuk aplikasi termoelektrik adalah paduan Half-Heusler (HH). Untuk mengetahui nilai ZT dari HH dilakukan simulasi untuk mengetahui nilai ZT dari paduan HH FeVZ (Z = As, P, Sb) dengan menggunakan *Density Functional Theory* (DFT). Hasil penelitian kami menunjukkan bahwa FeVAs memiliki nilai ZT yang lebih tinggi dari FeVP dan FeVSb pada kisaran temperatur 150-900 K. Semua paduan material masih memiliki nilai ZT yang baik sekitar ~ 0,7 bahkan pada nilai temperatur 900 K dan menunjukkan trend yang baik untuk material termoelektrik tipe-p.

***Kata Kunci**: Half-Heusler, Figure of merit, Termoelektrik*

Abstract. The figure of merit (ZT) holds an important role in thermoelectric material that indicates the efficiency of thermoelectric (TE) devices. The higher ZT value, the higher efficiency would be obtained of TE devices. One of the sub-class materials that has high potential application for thermoelectric material is Half-Heusler (HH) alloy. In order to investigate the ZT value of HH conduct simulation using to investigate the ZT value of HH alloy FeVZ (Z= As, P, Sb) by using density-functional theory (DFT). Our research results show that FeVAs has higher ZT values than FeVP and FeVSb in the range temperature of 150-900 K. All of those compounds still have good ZT value around ~0.7 even in the temperature regime of 900 K, and shows a good trend for p-type thermoelectric materials.

***Keywords**: Half-Heusler, Figure of merit, Thermoelectric*

DOI : *10.15408/fiziya.v4i1.19615*

P-ISSN: 2621-0215, E-ISSN: 2621-489X

INTRODUCTION

The discovery of the Heusler Alloy (HA) was founded by F. Heusler at the end of the 20th century, which reveals that Cu_2MnAl is magnetic although its constituent elements are not [1]. HA has a general formula of X_2YZ for full-Heusler (FH) and XYZ for half-Heusler (HH) where X and Y are transition metal elements, and Z is the main group element, and surprisingly, its magnetic moment can be predicted by simple rule calculation called Slater-Pauling rule [1], [2].

HA has a high tuning capacity because the properties of this material can be modified by changing its compounds through chemical substitutions and structural motifs [3] and the exploration of HA has been extensively explored due to its fascinating properties that can be implemented in the technology such as spintronic technology [4], shape-memory materials [5], superconductors [6], and thermoelectric (TE) devices [7].

Thermoelectric as one of the HA properties has been extensively studied to obtain high figures of merit (ZT) which describes the efficiency of the TE material. The higher the ZT, the higher the efficiency of the TE material. Half-Heusler (HH) alloy as one of the HA families and as one of the promising candidates for TE materials [7], has high ZT values around $ZT \approx 1$ [8]. Nano-sized grains is used experimentally in order to reduce the thermal conductivity between grain boundaries mediated by phonon scattering [9]. Another approach such as nanocomposites is also used by certain metal combinations that have been preferred to reduce thermal conductivity due to the difference in atomic size [10].

Due to of its high potential application as thermoelectric materials, therefore, we try to explore the iron-based of half-Heusler FeVZ (Z= As, P, Sb) by performing the density-functional theory (DFT) calculation using Quantum-Espresso package [11], [12] to obtain its electronic properties and BoltzTraP calculation to obtain the thermal properties (electronic part) of the FeVZ systems [13].

COMPUTATIONAL METHODS

In order to acquire the density of states (DOS) and the chemical potential information of FeVZ, we perform the DFT calculations by running Quantum-Espresso (QE) package [11], [12]. We also incorporate the Message Passing Interface (MPI) for parallel computing to reduce the computational time [14]. The Pseudopotential type that is used in this work is the Local Density Approximation (LDA) type pseudopotential of the Psilibrary [15]. After we obtain the DOS and the chemical potential, we then perform BoltzTraP calculation to get the electrical conductivity, thermal conductivity, Seebeck coefficient, and ZT of FeVZ systems [13].

(a) (b)

Figure 1. The $C1_b$ crystal structure of FeVZ with the lattice constant of 5.4855 Å, 5.3138 Å, and 5.7758 Å for FeVAs, FeVP, and FeVSb, respectively. (a) Conventional unit cell of FeVZ systems occupy the Wyckoff positions of Fe (red), V (grey), and As/P/Sb (yellow) placed at (0,0,0), (0.25,0.25,0.25), and (0.75,0.75,0.75), respectively. (b) Primitive unit cell of FeVZ systems.

RESULTS AND DISCUSSION

Density of States (DOS)

We use 12×12×12 k-points grid mesh in the self-consistent field (SCF) of QE calculation for all compounds and 36×36×36 k-points grid mesh for the non-self-consistency field (NSCF) calculation in order to obtain a good quality DOS and accurate chemical potential value. The chemical potential values obtained from QE calculation of FeVAs, FeVP, and FeVSb which are 14.26 eV, 15.31 eV, and 12.98 eV, respectively. All of those chemical potential values lies on the edge of the DOS that indicate all of the systems are p-type semiconductor (see figure 2).

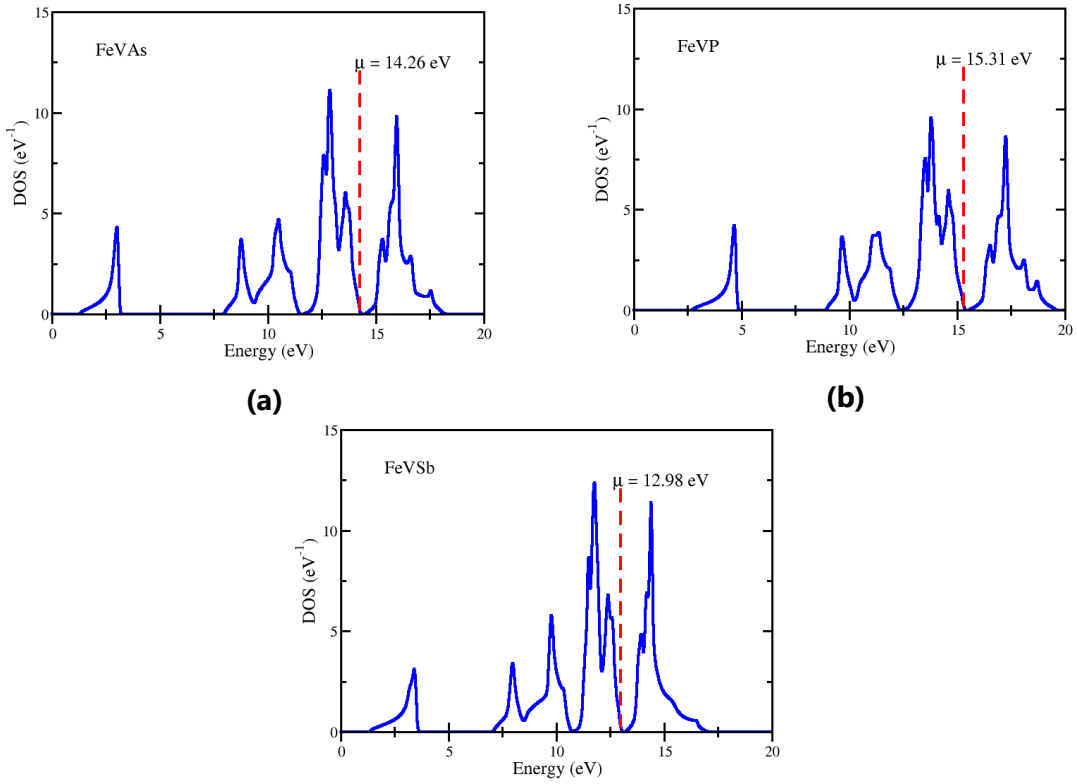

Figure 2. The DOS of: (a) FeVAs, (b) FeVP, and (c) FeVSb.

Vol.4 No.I Tahun 2021, 45 – 51
P-ISSN: 2621-0215, E-ISSN: 2621-489X

Electrical and Thermal Conductivity

Figure 3 shows the temperature-dependent electrical conductivity per relaxation time τ of FeVZ systems obtained from the BoltzTraP calculation. τ value is assumed to be a constant, and its typical value is around 10^{-14} s [16].

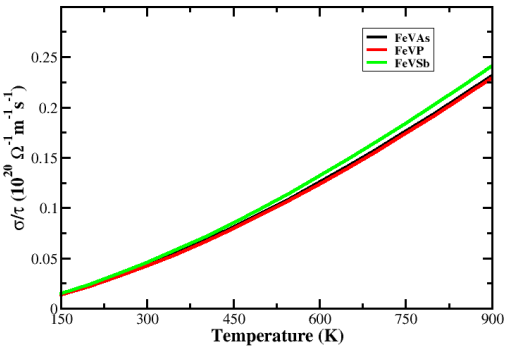

Figure 3. The temperature-dependent electrical conductivity (σ) of the FeVZ systems.

As shown in figure 3, the value of σ increases as the temperature is increased for all system, and typically are similar for all system indicating that all of those materials have good electrical conductivity even for high temperature of 900 K.

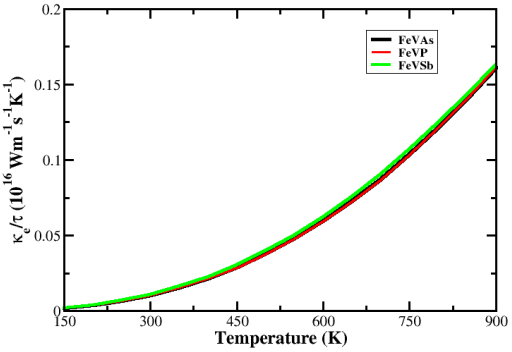

Figure 4. The temperature-dependent electron thermal conductivity (κ_e) of the FeVZ systems.

Figure 4 shows the electron thermal conductivity (ETC) of the FeVZ systems which increase as the temperature increases. From the information above, all κ_e of FeVZ systems almost give the same values in the temperature range of 150-900 K. However, we should note that the real κ obtained through experimental result contains two contribution formulated as

$$\kappa = \kappa_e + \kappa_{ph}, \tag{1}$$

where κ_e is the thermal conductivity contributed by electron, while κ_{ph} is the thermal conductivity contributed by phonon. Because the calculation to obtain the thermal conductivity of the phonon contribution need an expensive calculation and took a very long computational time, we restrict our calculation only to the thermal conductivity of the electron contribution to give a rough interpretation about the figure of merit of the FeVZ systems. However, we realize that a very good approximation should include the thermal conductivity of the phonon contribution to give very accurate ZT values.

Vol.4 No.I Tahun 2021, 45 – 51
P-ISSN: 2621-0215, E-ISSN: 2621-489X

Seebeck Coefficient and Figure of Merit

Figures 5 shows the Seebeck coefficient of FeVZ in the range temperature of 150 – 900 K.

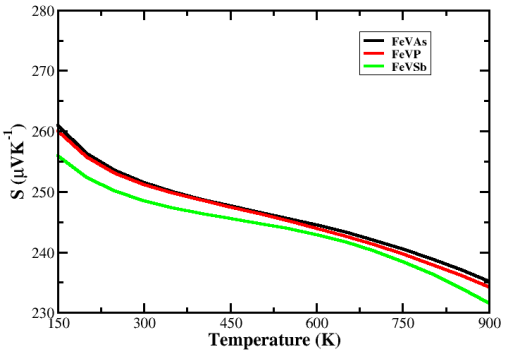

Figure 5. The temperature-dependent Seebeck coefficient (*S*) of FeVZ.

In figure 5, we see that FeVSb trend is quite shifted from the other, while the FeVP trend is slightly different from the FeVAs system. The Seebeck coefficient decreases as the temperature increases and shows a good trend of the p-type thermoelectric material even for high-temperature regime.

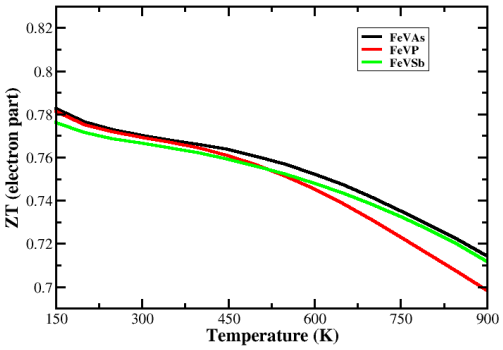

Figure 6. The temperature-dependent figure of merit (ZT) of FeVZ.

From the figure of merit data shown in figure 6, we obtain that FeVAs has higher ZT value than FeVP and FeVSb. At 900 K, we can see the difference that FeVP is quite different from FeVAs and FeVSb. However, that all of those materials still give high ZT value around 0.7 for FeVP, 0.71 for FeVSb, and 0.715 for FeVAs. Those ZT values range are still acceptable for HH material and in agreement with other HH material conducted by Vandu et al. which obtain the ZT value around 0.8-1 for TiNiSn system doped with Zr and Hf [17].

CONCLUSION

We have done the first-principles density functional theory calculation to study the thermoelectric behavior of half-Heusler FeVZ (Z=As, P, Sb). Our results show that FeVAs has higher ZT value than FeVP and FeVSb. We obtain that all of the FeVZ systems behave as p-type semiconductor signatured by the positive sigh of their Seebeck coefficient values. The Seebeck coefficient and figure of merit (electron part) of

all of FeVZ systems in the room temperature are around ~250 μV/K and ~0.75, respectively. All FeVZ systems in 900 K still gives a high Seebeck coefficient and figure of merit (electron part) around ~230 μV/K and ~0.7, respectively. We realize that our results may not yet give a fully realistic prediction for the real material due to the phonon contribution which is neglected to the calculation of the figure of merit (ZT). We acknowledge that the phonon thermal conductivity must be considered in the calculation in order to obtain a more realistic prediction of ZT values.

ACKNOWLEDGEMENT

This research was supported by High-Performance Computing facility (https://hpc.lipi.go.id/) of Indonesian Institute of Sciences (LIPI).

REFERENCES

[1] T. Graf, C. Felser, and S. S. P. Parkin, "Simple rules for the understanding of Heusler compounds," *Progress in Solid State Chemistry*, vol. 39, no. 1, pp. 1–50, 2011.
[2] S. Skaftouros, K. Özdoğan, E. Şaşıoğlu, and I. Galanakis, "Generalized Slater-Pauling rule for the inverse Heusler compounds," *Physical Review B*, vol. 87, no. 2, p. 024420, Jan. 2013.
[3] L. Wollmann, A. K. Nayak, S. S. P. Parkin, and C. Felser, "Heusler 4.0: Tunable Materials," *Annual Review of Materials Research*, vol. 47, no. 1, pp. 247–270, Jul. 2017.
[4] T. Graf, C. Felser, and S. S. P. Parkin, "Heusler compounds: Applications in spintronics," in *Handbook of Spintronics*, Springer Netherlands, 2015, pp. 335–364.
[5] V. Srivastava and K. P. Bhatti, "Ferromagnetic shape memory Heusler alloys," in *Solid State Phenomena*, vol. 189, Trans Tech Publications Ltd, 2012, pp. 189–208.
[6] T. Klimczuk *et al.*, "Superconductivity in the Heusler family of intermetallics," *Physical Review B - Condensed Matter and Materials Physics*, vol. 85, no. 17, May 2012.
[7] T. M. Tritt, "Thermoelectric Phenomena, Materials, and Applications," *Annual Review of Materials Research*, vol. 41, no. 1, pp. 433–448, Aug. 2011.
[8] L. Huang, Q. Zhang, B. Yuan, X. Lai, X. Yan, and Z. Ren, "Recent progress in half-Heusler thermoelectric materials," *Materials Research Bulletin*, vol. 76. Elsevier Ltd, pp. 107–112, 01-Apr-2016.
[9] X. Yan *et al.*, "Enhanced thermoelectric figure of merit of p-type half-heuslers," *Nano Letters*, vol. 11, no. 2, pp. 556–560, Feb. 2011.
[10] Y. Kimura, H. Ueno, and Y. Mishima, "Thermoelectric properties of directionally solidified half-heusler (M 0.5a,M 0.5b)NiSn (M a, M b = Hf, Zr, Ti) alloys," in *Journal of Electronic Materials*, 2009, vol. 38, no. 7, pp. 934–939.
[11] P. Giannozzi *et al.*, "QUANTUM ESPRESSO: a modular and open-source software project for quantum simulations of materials," *Journal of Physics: Condensed Matter*, vol. 21, no. 39, p. 395502, Sep. 2009.
[12] P. Giannozzi *et al.*, "Quantum ESPRESSO toward the exascale," *Journal of Chemical Physics*, vol. 152, no. 15, p. 154105, Apr. 2020.
[13] G. K. H. Madsen and D. J. Singh, "BoltzTraP. A code for calculating band-structure dependent quantities," *Computer Physics Communications*, vol. 175, no. 1, pp. 67–71, Jul. 2006.
[14] "MPI: A Message-Passing Interface Standard," 2015.
[15] A. Dal Corso, "Pseudopotentials periodic table: From H to Pu," *Computational Materials Science*, vol. 95, pp. 337–350, Dec. 2014.
[16] G. L. Eesley, "Relaxation time of electrons," *Access Science*, 2020.

[17] N. Van Du *et al.*, "X-site aliovalent substitution decoupled charge and phonon transports in XYZ half-Heusler thermoelectrics," *Acta Materialia*, vol. 166, pp. 650–657, Mar. 2019.

Available online at:
Al-Fiziya: Journal of Materials Science, Geophysics, Instrumentation and Theoretical Physics
Website: http://journal.uinjkt.ac.id/index.php/al-fiziya
Vol.4 No.I Tahun 2021, 52 – 62

Analysis of Superhydrophobic-Superoleophilic Properties on Modification of Polyurethane Sponge for Selective Oil-Water Separation

Niken Aprilia Eka Putri[1,†], Arif Tjahjono[1], Perdamean Sebayang[2]

[1]Physics Study Program, Faculty of Sciences and Technology, Syarif Hidayatullah State Islamic University Jakarta, Tangerang Selatan 15412, Indonesia

[2]Research Center for Physics, Indonesian Institute of Sciences (LIPI), South Tangerang, Banten, 15314, Indonesia

[†]niken.aprilia16@mhs,uinjkt.ac.id

Submitted: February 2021; Revised: March 2021; Approved: April 2021; Available Online: June 2021

Abstrak. Pada penelitian ini, telah dilakukan modifikasi material spons polyurethane (PU) untuk memperoleh sifat superhidrofobik-superoleofilik. Modifikasi yang dilakukan yakni melapisi spons PU dengan beberapa nanomaterial seperti ZnO, Fe_3O_4+TEOS, dan stearic acid dengan metode *dip-coating* dan *drop-coating*. Pengujian yang dilakukan meliputi pemisahan minyak dan air secara selektif dengan menggunakan respon magnetik. Beberapa jenis minyak dan pelarut organik diuji daya serapnya. Hasil penelitian menunjukkan bahwa spons PU@ZnO@Fe_3O_4@SA memiliki kapasitas penyerapan yang cukup baik, yaitu sebesar 4.37 mL hingga 7.37 mL. Spons PU yang dibuat dapat secara selektif memisahkan minyak dari air dengan efisiensi pemisahan diatas 99%. Spons PU yang dibuat juga dapat digerakkan secara magnetis oleh medan magnet eksternal. Dari hasil karakterisasi menggunakan 3D OM, diperoleh sudut kontak air sebesar 153.38° yang menunjukkan bahwa spons PU@ZnO@Fe_3O_4@SA merupakan superhidrofobik. Dari morfologi permukaan diperoleh ukuran rata-rata diameter pori sebesar 167.475 µm.

***Kata Kunci**: superhidrofobik-superoleofilik, spons PU, ZnO, Fe_3O_4+TEOS, stearic acid.*

Abstract. In this research, a modification of polyurethane (PU) sponge material has been made to obtain superhydrophobic-superoleophilic properties. The PU sponge was coated with several nanomaterials such as ZnO, Fe_3O_4+TEOS, and stearic acid by dip-coating and drop-coating methods. The tests include selective separation of oil and water with a magnetic response. Several types of oil and organic solvents were tested for absorption capacity. The results showed that the PU@ZnO@Fe_3O_4@SA sponge has a good absorption capacity, from 4.37 mL to 7.37 mL. The fabricated PU sponge could selectively separate oil from water with a separation efficiency above 99%. The fabricated PU sponge also could be magnetically driven by external magnetic fields. From the characterization using 3D OM, the water contact angle was 153.38°, which indicates that the PU@ZnO@Fe_3O_4@SA sponge is superhydrophobic. And from surface morphology obtained an average pore size diameter of 167.475 µm.

***Keywords**: superhydrophobic-superoleophilic, PU sponge, ZnO, Fe_3O_4+TEOS, stearic acid.*

DOI : *10.15408/fiziya.v4i1.19808*

P-ISSN: 2621-0215, E-ISSN: 2621-489X

INTRODUCTION

Production and consumption of petroleum products have increased worldwide. With the increasing need for petroleum, there is a risk of accidents due to oil spills [1]. The largest case of oil spills occurred in 2010 in the Gulf of Mexico with 779 million liters of oil spilled into the sea [2]. The effects of environmental pollution caused by oil spills and organic pollutants that insoluble in water require an urgent cleaning process. Thus, an oil collector based on sorbent materials with special properties is needed [3]. PU sponge is one of the candidate materials, but commercial PU sponge cannot be used immediately, so surface modification is needed to obtain superhydrophobic-superoleophilic properties [4].

Superhydrophobic

Hydrophobic is a term derived from a Greek term "hydro" meaning water and "phobos" meaning fear. Hydrophobic literally means "the fear of water". So, superhydrophobic is a special property of a surface because of its high ability to repel water with a contact angle above 150°. Superhydrophobicity arises when a molecule does not partake in the hydrogen bonding of water [5]. The surface of a lotus leaf is an example of superhydrophobicity, because of its non-wetting surface and perfection of its water repellency with unique hierarchical micro/nanoscale structures [6]. Superhydrophobicity can be improved by reducing surface tension and by increasing surface roughness [7].

Surface Tension

Surface tension is the energy required to increase the surface area of a liquid due to intermolecular forces [5]. The cohesion force acts to separate the two different materials in the same intervention medium. If the cohesion force on a solid is higher than a liquid, then the two materials will not stick together and tend to form the smallest possible surface area. That's why the water droplets are spherical because the spherical shape is the most stable geometry and can minimize surface tension [8]. Thus, it is necessary to reduce surface tension to obtain wetting properties such as superhydrophobic.

Surface Roughness

In general, the surface roughness will make hydrophobic surfaces superhydrophobic. The concept of superhydrophobic was introduced by Wenzel (1936). Wenzel proposes a modification to Young's equation based on the Wenzel state [6], [9].

$$\cos\theta_W = r_s \times \cos\theta, \quad (1)$$

where θ_W is the contact angle at the Wenzel state and r_s is the roughness factor. This Wenzel equation predicts that the contact angle can be increased by roughing the surface [7].

The Wenzel theory was further developed by Cassie and Baxter (1944). The Cassie-Baxter model shows the angle of contact depends on the percent of solids in contact with the droplets. On heterogeneous (porous) surfaces it decreases with increasing part of the wettable surface [10]. The Cassie-Baxter equation:

$$\cos\theta_{CB} = f_s \times \cos\theta - (1 - f_s), \quad (2)$$

Vol.4 No.I Tahun 2021, 52 – 62
P-ISSN: 2621-0215, E-ISSN: 2621-489X

where θ_{CB} is the angle of contact in the Cassie-Baxter state, and f_s is the fraction of the surface area in contact with the liquid droplet [6].

Superoleophilic

Oleophilic comes from the word "oleo" meaning oil and "philic" meaning love. As the wettability properties of the others, oleophilic is a property of some materials due to its ability to attract oil [11]. Oleophilic refers to materials that have a strong affinity for oils. A surface is oleophilic if it has a contact angle to the oil less than 90°. Meanwhile, surfaces that are superoleophilic have a contact angle to the oil of less than 10° even 0° [12]. Superoleophilic is a surface whose energy is dominated by London dispersion forces, exceeding the surface tension of hydrocarbons [13].

Porous surfaces with superoleophilic properties (good permeability to oil) are commonly used as oil-water separation devices [14]. Because such surfaces are easily wet with oil but can completely repel water, they are effective in the separation process of water and oil mixtures.

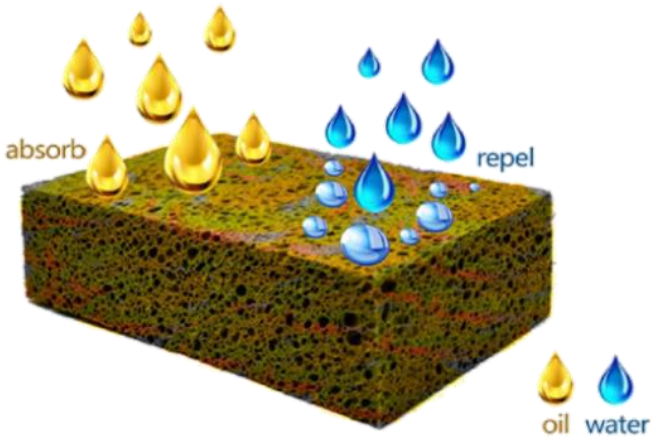

Figure 1. superhydrophobic-superoleophilic on the surface of the sorbent material

The maximum oil absorption capacity (k) for a porous sorbent material can be calculated by weight gain ratio,

$$k = \frac{W_a - W_b}{W_b} \ (g/g), \tag{3}$$

where W_a and W_b are the weight of the sorbent after and before oil absorption, respectively. Meanwhile, to calculate the separation efficiency of a mixture of oil and water (50%, v/v) or an oil-in-water emulsion (e) can be determined as:

$$e = \frac{V_a}{V_b} \times 100\%, \tag{4}$$

where V_a is the volume of water remaining on the surface and V_b is the initial volume of water in the water-oil mixture [15].

Vol.4 No.I Tahun 2021, 52 – 62
P-ISSN: 2621-0215, E-ISSN: 2621-489X

EXPERIMENT

Materials

Commerical polyurethane sponges (PU sponge D.24), ZnO, Fe_3O_4 nanoparticles, TEOS, NH_4OH, and stearic acid were used to modify surfaces. Palm oil, olive oil, castor oil, lubricating oil, kerosene, and gasoline were used to test the oil absorption capacity of the fabricated sponge. Deionized water was used for all experiments and tests.

Methods

The research was done with an experiment to make superhydrophobic-superoleophilic sponges. But, before that, Fe_3O_4 was first coated with TEOS precursor solution.

Preparation of Fe_3O_4 Nanoparticles

The magnetic Fe_3O_4 nanoparticles were prepared by coating the material with a TEOS precursor solution. Briefly, 4 g Fe_3O_4 were stirred with ethanol and deionized water for 30 minutes. After that, 4 mL of TEOS were poured, and 10 mL of NH_4OH were slowly added to the solutions containing Fe_3O_4, the mixture was stirred for 6 h. The mixture was repeatedly separated by a magnet and washed with deionized water. Then, Fe_3O_4 dried at 80° for 18 hours.

Preparation of Superhydrophobic-Superoleophilic Sponge

The pristine PU sponge was cut into cubes ($2\times2\times2$ cm^3) and cleaned with deionized water and ethanol several times and dried at 60°C for 6 h. Several pieces of clean sponges were immersed in a uniform suspension contains 0.2 g ZnO and 30 mL ethanol by ultrasonication for 30 min, and dried at 80℃ for 2 h. PU@ZnO sponges were uniformly coated with Fe_3O_4+TEOS by drop-coating method and dried. But, it was found that the interaction between the sponge and the Fe_3O_4 particles was weak. Then, the PU@ZnO@Fe_3O_4 sponges were dipped into 0.1 g stearic acid solution overnight at room temperature. Stearic acid was used as the top layer, to decrease the loss of Fe_3O_4 and also to obtain superhydrophobicity. The PU@ZnO@Fe_3O_4@SA were annealed at 80℃ for 4h to obtain the superhydrophobic-superoleophilic PU sponge.

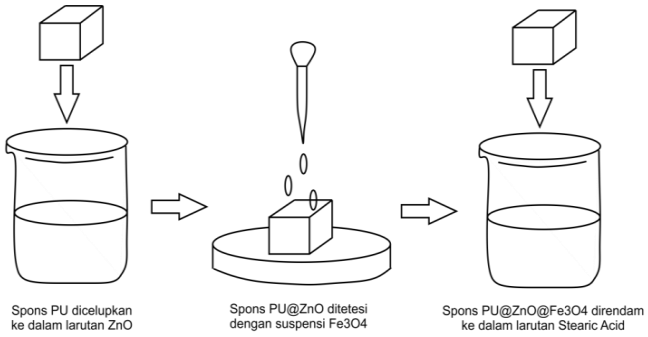

Figure 2. Schematic steps involved in the synthesis of superhydrophobic-superoleophilic PU sponge

RESULTS AND DISCUSSIONS

Testing results of the surface-modified PU sponges

Wetting Properties

To determine the surface properties of each sponge, a comparison was made between pristine PU sponge, PU@ZnO sponge, PU@Fe_3O_4@SA sponge, and PU@ZnO@Fe_3O_4@SA sponge, as shown in the following image and table.

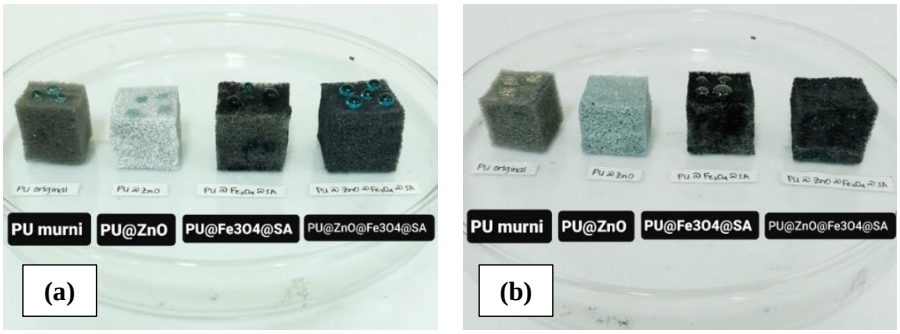

Figure 3. Surface properties between the coated PU sponges (a) with water and (b) with oil

Table 1. Surface properties to water and oil

PU sponge	Surface Properties to Water	Surface Properties to Oil
Pristine PU sponge	Hydrophobic	Oleophobic
PU@ZnO sponge	Superhydrophilic	Superoleophilic
PU@Fe_3O_4@SA sponge	Hydrophobic	Oleophobic
PU@ZnO@Fe_3O_4@SA sponge	Superhydrophobic	Superoleophilic

Based on Figure 3 and Table 1, it's known that the PU@ZnO@Fe_3O_4@SA sponge is superhydrophobic-superoleophilic. Because the surface has good abilities to repel the water and can completely absorb oil. Sample with the composition of ZnO 0.2g, Fe_3O_4 0.3g, and SA 0.1g was made to test the capacity

Absorption Capacity

Several types of fluids include oil and organic solvents used to test the time and absorption capacity of the PU@ZnO@Fe_3O_4@SA sponge.

Table 2. Test results of PU@ZnO@Fe_3O_4@SA sponge with several types of oils and organic solvents

Types of Oil	Density of Oil (g/cm^3)	Absorption Capacity (g/g)	Absorbed Volume (mL)
Palm Oil	0.92	12.5845	6.6332
Olive Oil	0.91	14.0268	6.7053
Castor Oil	0.95	13.7361	6.8732
Lubricating Oil	0.90	11.5483	6.4594
Gasoline	0.73	10.4116	7.3745
Kerosene	0.82	10.5448	6.3682

Types of Organic Solvent	Density of Organic Solvent (g/cm^3)	Absorption Capacity (g/g)	Absorbed Volume (mL)
Ethanol	0.80	11.1777	5.0908
Aceton	0.78	10.2260	6.2078
n-Hexane	0.65	9.4568	6.6361
Toluene	0.86	11.7350	6.2125
Tetrachloromethane	1.59	12.8844	4.3774
Trichlorethen	1.32	13.0129	5.1864

Oil-Water Separation

Tetrachloromethane was used to test the ability of the oil-water separation of PU@ZnO@Fe_3O_4@SA sponge. In this case, oil has a density lower than water is hard to use, so tetrachloromethane acts as a substitute for oil. Tetrachloromethane and water are both clear liquids. So the water must be given a dye to facilitate visual observation.

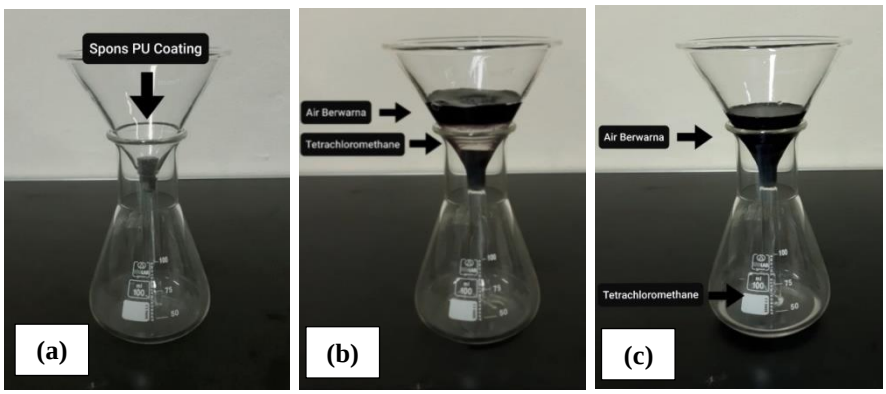

Figure 4. (a) PU sponge in a funnel (b) A mixture of dyed water and tetrachloromethane (50%/50%) poured into the funnel (c) Selective separation of water from organic solvent by PU@ZnO@Fe_3O4@SA sponge

From the results, it's known that the PU@ZnO@Fe_3O_4@SA sponge can selectively separate water from organic solvents. Tetrachloromethane can completely absorb the oil with small pieces of coated PU Sponge, showing its superoleophilic properties. Meanwhile, water is held above the surface and repelled because of its superhydrophobic properties. The modified PU sponge can selectively separate oil-water with separation efficiency above 99%.

Magnetic Response

Adding a magnetic component such as Fe_3O_4 is a simple way to drive the PU@ZnO@Fe_3O_4@SA sponge using an external magnetic field. Oil adsorption for cleaning the water surface by a magnet can be seen in the figure below.

Vol.4 No.I Tahun 2021, 52 – 62
P-ISSN: 2621-0215, E-ISSN: 2621-489X

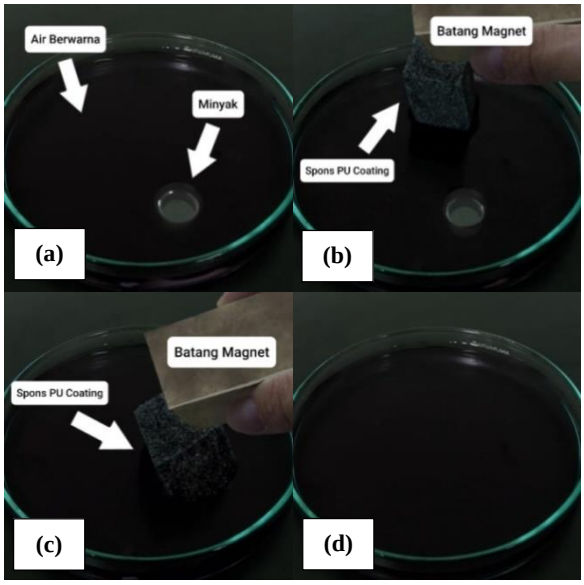

Figure 5. (a) Petri dish containing oil droplet on the dyed water surface (b, c) cleaning oil with magnetically PU@ZnO@Fe_3O_4@SA sponge (d) cleaned water surface

The modified PU sponge has a magnetic response that is good enough. So that is easy to use in the selective separation of oil-water.

Characterization results of the surface-modified PU sponges

Water Contact Angle

There were 4 samples observed, including pristine PU sponge, PU@ZnO sponge, PU@Fe_3O_4@SA sponge, and PU@ZnO@Fe_3O_4@SA sponge. The 3D OM characterization was carried out by using the sessile drop method. The results of measuring the water contact angle on the surface can be seen in the image below.

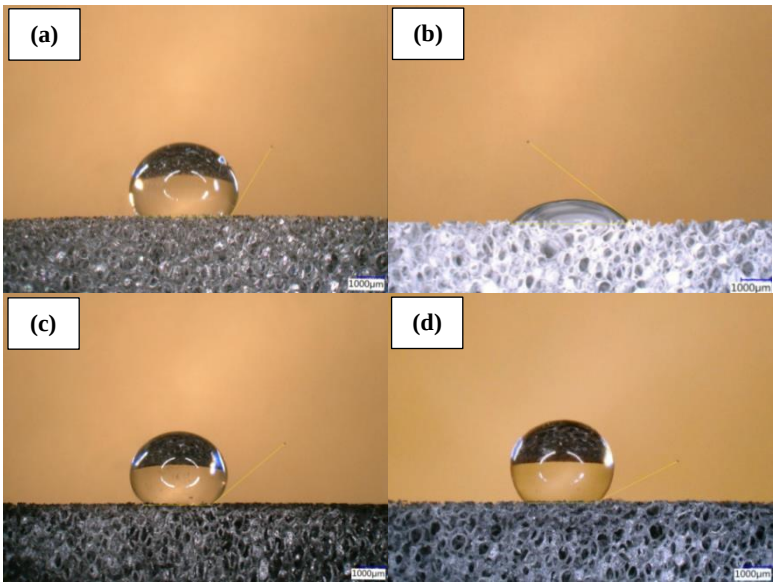

Figure 6. Water contact angle measurement (a) pristine PU sponge, (b) PU@ZnO sponge, (c) PU@Fe_3O_4@SA sponge, and (d) PU@ZnO@Fe_3O_4@SA sponge

The water contact angle is affected by surface tension. Contact angle on the surface occurs because the cohesion force between water droplet molecules is greater than the adhesion force between water molecules and molecules on the surface. Water droplets tend to be attracted to a sphere due to the forces between molecules.

Water droplets on the surface were observed with 3D OM to measure the contact angle. Measurements performed 10 times to get a definite value and reduce human error. Measurement of the average contact angles shown in the following table.

Table 3. Measurement of the average contact angle

Sample	Average Contact Angle	Surface Properties
Pristine PU sponge	120.34°	Hydrophobic
PU@ZnO sponge	37.14°	Hidrophilic
PU@Fe_3O_4@SA sponge	140.40°	Hydrophobic
PU@ZnO@Fe_3O_4@SA sponge	153.38°	Superhydrophobic

From **Table 3**, it is known that the modified PU Sponge has increased the contact angle. This increased contact angle occurs due to the role of each component. Such as Fe_3O_4 and stearic acid increases surface roughness, and ZnO acts as an amphiphilic surfactant. All of those can change the surface wettability to become superhydrophobic and proves the theory of Wenzel also Cassie-Baxter which states that surface roughness and low surface tension can increase the water contact angle.

Surface Morphology

To determine how surface roughness affects the surface properties, it can be seen in the surface morphology image below.

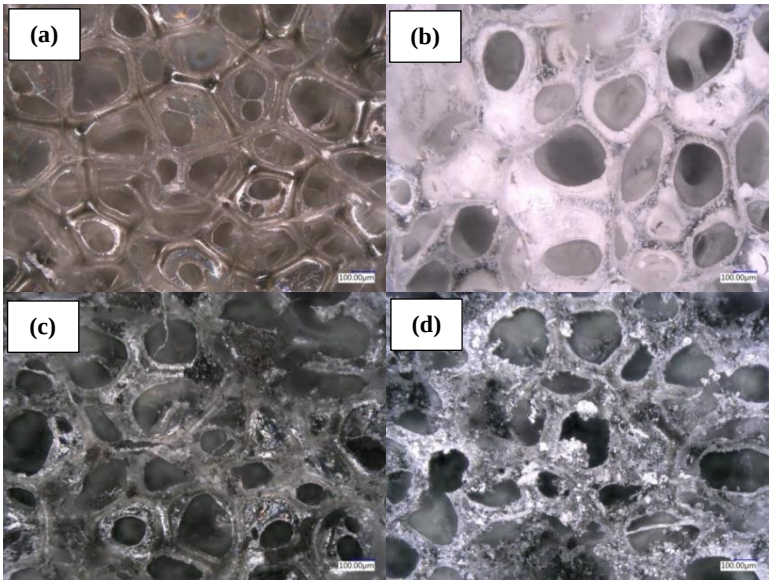

Figure 6. Images of surface morphology using 3D OM with 200x magnification (a) pristine PU sponge, (b) PU@ZnO sponge, (c) PU@Fe_3O_4@SA sponge, (d) and PU@ZnO@Fe_3O_4@SA sponge

The color difference in the image above shows the difference in the material coated on the PU sponge. But at this magnification, the material can't be identified obviously, so done again with a magnification of 500x. Pores morphology observations were shown in the following figure.

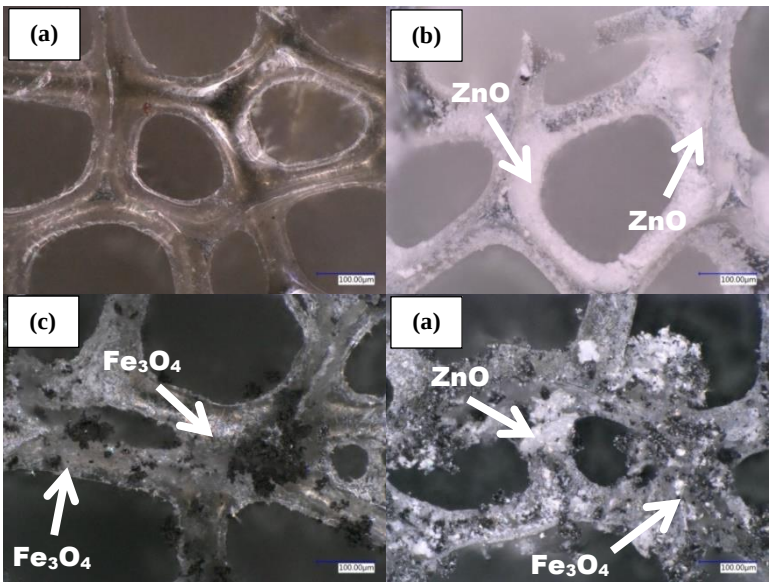

Figure 7. Images of surface morphology using 3D OM with 500x magnification (a) pristine PU sponge, (b) PU@ZnO sponge, (c) PU@Fe_3O_4@SA sponge, (d) and PU@ZnO@Fe_3O_4@SA sponge

In **Figure 7a**, pores of the pristine PU sponge still refined because they haven't coated yet. But, in **Figure 7b** there was a thin white layer due to the addition of ZnO. Meanwhile, in **Figure 7c**, there were black lumps due to the addition of Fe_3O_4. In **Figure 7d**, it can be seen how the ZnO and Fe_3O_4 materials are mixed and make the pore diameter smaller. The addition of stearic acid could affect the roughness of the PU sponge pores. This proves that surface roughness affects its wettability.

Along with the increasing number of component materials, the rougher the surface, the better surface will repel water. So the PU@ZnO@Fe_3O_4@SA sponge has better wettability compared to other samples.

Surface roughness is evidenced by a change in the average pore diameter of PU sponges. ImageJ software is used to processing images obtained from 3D OM observations with a magnification of 200x (Fig 6) to determine the size distribution of the average diameter of the coated PU sponge. The data performed 50 times with various diameter sizes. The results are shown in the table below.

Table 4. Average diameter of PU sponges pore size using ImageJ

Sample	Average Diameter (µm)	Minimum (µm)	Maximum (µm)	Standard Deviation (µm) ± (*n*)
Pristine PU sponge	209.76	116	343.913	56.077 ± (50)
PU@ZnO sponge	203.23	92.65	336.149	57.098 ± (50)
PU@Fe_3O_4@SA sponge	198.841	84.095	297.469	51.241 ± (50)
PU@ZnO@Fe_3O_4@SA sponge	167.475	78.409	290	52.11 ± (50)

The more the material is added, the smaller the pore diameter. It will increase the surface roughness, thus affecting its superhydrophobic properties.

CONCLUSIONS

The PU@ZnO@Fe3O4@SA sponge has superhydrophobic-superoleophilic properties because it can selectively separate oil and water with a separation efficiency above 99% and has an absorption capacity of oil and organic liquids of 4.37 mL to 7.37 mL. The fabricated PU sponge also has a magnetic response guided by external magnetic fields to adsorb oil. The addition of ZnO, Fe3O4, and stearic acid nanomaterials can reduce surface tension and increase surface roughness, both of them can affect the increase in contact angle. The contact angle formed on the PU@ZnO@Fe3O4@SA sponge is 153.38° with a pore size diameter of 167.475 µm. Hopefully, this research can be applied in the continuous separation of oil-water mixtures in large scales for application in the cleanup of oil spills and removal of organic solvents from water.

ACKNOWLEDGMENT

This research was supported by the Research Center for Physics, Indonesian Institute of Sciences (LIPI), Indonesia. The authors express their gratitude to professor Perdamean Sebayang and other researchers of nanomagnetic materials.

REFERENCES

[1] M. Fingas, *Oil Spill Science and Technology*, 1st ed., vol. 53, no. 9. USA, 2013.
[2] M. Schrope, "Oil spill: Deep wounds," *Nature*, vol. 472, no. 7342, pp. 152–154, 2011
[3] J. Ge, H. Y. Zhao, H. W. Zhu, J. Huang, L. A. Shi, and S. H. Yu, "Advanced Sorbents for Oil-Spill Cleanup: Recent Advances and Future Perspectives," *Adv. Mater.*, vol. 28, no. 47, pp. 10459–10490, 2016
[4] S. Zhou *et al.*, "One-pot synthesis of robust superhydrophobic, functionalized graphene/polyurethane sponge for effective continuous oil-water separation," *Chem. Eng. J.*, vol. 302, pp. 155–162, 2016
[5] J.-P. Tolvanen, J. Sprinkle, M. Rossi, and S. Kelly, *Hydrophobic surfaces: Effect of surface structure on wetting and interaction forces*. 2010.
[6] A. Carré and K. L. Mittal, *Superhydrophobic Surface*, vol. 65, no. 6. CRC Press, 2009.
[7] R. L. J. Crawford and E. P. Ivanova, *Superhydrophobic Surfaces*. Aalborg, 2015.
[8] I. Yılgör, E. Yılgör, and C. K. Söz, *Superhydrophobic polymer surfaces : preparation, properties and applications*.
[9] A. Søbye, J. K. Jørgensen, M.-L. K. Lund, and M. O. Mikkelsen, "Superhydrophobic Surfaces: A study of the superhydrophobicity of modified silicon dioxide surfaces," Aalborg University, 2015.
[10] I. G. Wenten, N. F. Himma, S. Anisah, and N. Prasetya, "Membran Superhidrofobik: Pembuatan, Karakterisasi, dan Aplikasi," no. December, pp. 2018–2019, 2015.
[11] H. Wang *et al.*, "A novel carbon nanotubes reinforced superhydrophobic and superoleophilic polyurethane sponge for selective oil-water separation through a chemical fabrication," *J. Mater. Chem. A*, vol. 3, no. 1, pp. 266–273, 2015
[12] G. Kwon, E. Post, and A. Tuteja, "Membranes with selective wettability for the separation of oil-water mixtures," *MRS Commun.*, vol. 5, no. 3, pp. 475–494, 2015
[13] A. J. Groszek, "The role of oleophilic surface in lubrication," 1968.

[14] W. Lianga and Z. Guo, "Stable Superhydrophobic and Superoleophilic Soft Porous Materials for Oil/water Separation," *RSC Adv.*, pp. 1–6, 2013
[15] V. T. Tran and B. Lee, "Novel fabrication of a robust superhydrophobic PU@ZnO@Fe3O4@SA sponge and its application in oil-water separations," *Sci. Rep.*, no. June, pp. 1–12, 2017

Available online at:
Al-Fiziya: Journal of Materials Science, Geophysics, Instrumentation and Theoretical Physics
Website: http://journal.uinjkt.ac.id/index.php/al-fiziya
Vol.4 No.I Tahun 2021, 63 – 73

Simultaneous Seismic Inversion for Reservoir Characterization at Poseidon Field, Browse Basin, Australia

Suleman Mauritz Sihotang[1†], Ida Herawati[1]

[1]Geophysical Engineering Study Program, Faculty of Exploration and Production Technology, Universitas Pertamina, Teuku Nyak Arief, RT.7 / RW.8, Simprug, Kebayoran Lama, South Jakarta, DKI Jakarta 12220, Indonesia

[†]suleman.sihotang@gmail.com

Submitted: Februari 2021; Revised: March 2021; Approved: April 2021; Available Online: June 2021

Abstrak. Metode seismik inversi telah banyak digunakan untuk menghasilkan properti reservoir di lapangan minyak dan gas. Dalam penelitian ini, salah satu metode inversi yang dikenal sebagai inversi simultan digunakan untuk menganalisis karakterisasi reservoir di Lapangan Poseidon, Cekungan Browse. Inversi Simultan diterapkan pada data *partial angle stack* dan menghasilkan volume Impedansi Akustik (AI), Impedansi Geser (SI) dan parameter Lame (LMR). Penelitian ini bertujuan untuk mengetahui sebaran litologi batupasir yang tersaturasi gas pada formasi reservoir Plover. Analisis sensitivitas dilakukan dengan *cross-plotting* antara parameter elastis dan parameter Lame menggunakan lima data log sumur dan menganalisa jenis litologi dan fluida yang tersaturasi di dalamnya. Berdasarkan *cross-plot* tersebut, tipe litologi dapat diidentifikasi menggunakan parameter AI, λρ, μρ, dan λ/μ. Sedangkan keberadaan gas dapat dibedakan dengan menggunakan parameter SI, λρ, dan /μ. Keberadaan batupasir yang tersaturasi gas ditandai dengan nilai *Lambda-Rho* kurang dari 50 GPa g cc-1 dan *Lambda over Mu* kurang dari 0,8 GPa g cc-1. Peta dari setiap parameter dihasilkan pada interval reservoir. Berdasarkan peta tersebut, dapat disimpulkan bahwa persebaran batupasir yang tersaturasi gas tersebar di wilayah timur dan barat daerah penelitian.

***Kata Kunci**: Lambda Mu Rho, Inversi Simultan, Lapangan Poseidon*

Abstract. Seismic inversion method has been widely used to obtain reservoir property in an oil and gas field. In this research, one of inversion methods known as simultaneous inversion is used to analyze reservoir characterization at Poseidon Field, Browse Basin. Simultaneous inversion is applied to partial angle stack data and result in volume of Acoustic Impedance (AI), Shear Impedance (SI) and Lame parameter (LMR). The objective of this study is to determine distribution of sandstone lithology with gas saturated in Plover reservoir formation. Sensitivity analysis is done by cross-plotting elastic and Lame parameter from five well log data and analyzing lithology type and fluid saturation. Based on those cross-plots, lithological type can be identified from AI, λρ, μρ and λ/μ parameters. Meanwhile, the presence of gas can be discriminated using SI, λρ, and λ/μ parameters. Gas-saturated sandstone presence is characterized by Lambda-Rho value less than 50 GPa g cc^{-1} and Lambda over Mu value less than 0.8 GPa g cc^{-1}. Maps of each parameter are generated at reservoir interval. Based on those maps, it can be concluded that gas sand spread out in the eastern and western areas of research area.

***Keywords**: Lambda Mu Rho, Simultaneous Inversion, Poseidon field*
DOI : *10.15408/fiziya.v4i1.19782*

P-ISSN: 2621-0215, E-ISSN: 2621-489X

INTRODUCTION

Poseidon field is a gas field located on the Australian North-West Shelf and discovered in 2009 with Poseidon-1 exploration well. Subsurface data is made available to public in 2017 by Geoscience Australia and ConocoPhilips as field operator. The open datasets consist of well data and seismic reflection data. Seismic reflection is geophysical method that primarily used in oil and gas exploration to obtain subsurface information in wide coverage.

In this study, Poseidon data will be interpreted quantitatively to provide us about layer property especially on property of reservoir interval. Reservoir properties such as lithology type and fluid saturation are very important to estimate hydrocarbon reserve and to define potential for field development. Lithology and fluid saturation information is obtained by analyzing log data from drilled well and need to be mapped through the area using seismic data. We will use seismic inversion method that integrate well log and seismic data to obtain property volume. Inversion method will result in acoustic/elastic parameter that can relate to reservoir property based on sensitivity analysis.

In this study, we use simultaneous inversion method that works on pre-stack gather or multi partial angle stack data. By using this inversion method, the volume of Acoustic Impedance (AI), Shear Impedance (SI) and density. From those volume, we can transform to other parameters such as Lame parameters. By obtaining those parameters, the distribution of lithology and fluid will be mapped and analyzed at Poseidon Field.

METHODS

Data

The data used include:

1). Seismic data for partial angle stack in the form of near stack (6^0-18^0), mid stack (18^0 - 30^0) and far stack (30^0 - 42^0).
2). There are five well data (Kronos, Pharos, Poseidon 1, Poseidon 2 and Protheus) with log data consist of Gamma ray, Caliper, Resistivity, RHOB, NPHI, Vp, Vs, and Checkshot. The basemap of the research data is shown in Figure 1.

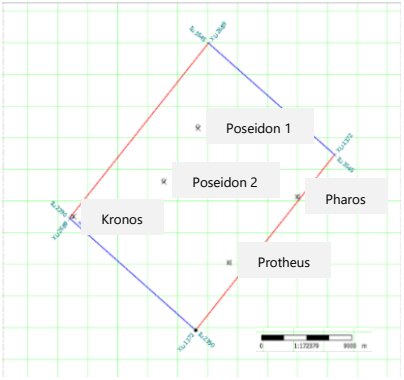

Figure 1. Basemap of the research area

Methodology

Workflow of the entire process is shown in Figure 2. Data processing that will be carried out in this study consist of several main stages, such as:

Sensitivity analysis

Sensitivity analysis is performed to determine the most sensitive parameters that can be used to analyze sandstone lithology zone and gas presence in the study area. This analysis is done by cross-plotting two parameters from log data and calculate shale Volumetric (Vshale) and water saturation (Sw) of each data point. The parameters tested are Acoustic Impedance (AI), Shear Impedance (SI), Lamda-rho, Mu-rho, and Lamda over Mu as well as Vshale and water saturation as the color key.

Low frequency model

This process is used to add low frequency information to seismic data due to the limited frequency information on seismic. The model is built by interpolating impedance value from well log through study area guided by horizon interpretation.

Inversion

This process is performed to extract impedance information from seismic data. The low frequency model and wavelet will be used as the input data along with the partial angle stack seismic data. By using the simultaneous inversion method, the volume of P-impedance, S-impedance, and density will be generated simultaneously.

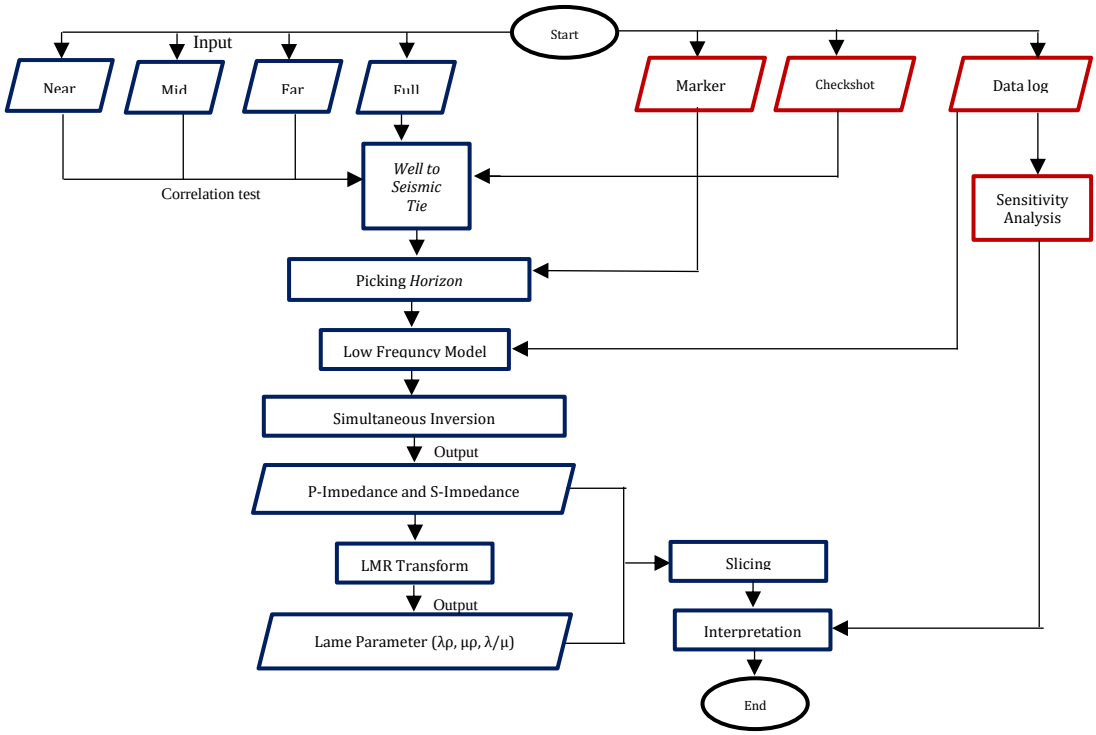

Figure 2. Simultaneous Inversion Workflow

FORMALISM

Regional Geology

Poseidon field is located at Browse Basin, offshore of Western Australian. This basin lies from the northeast to the southwest of Australia. Reservoir interval is Plover formation which was formed in the Early to Middle Jurassic Extension phase [1]. During this phase, many small faults were generated which resulted in the collapse of anticline structure that had been formed in the previous phase. In this phase, fluvio-deltaic sandstones and shallow marine sandstones are deposited and accompanied by silt rock and a little carbonate rock deposition.

Plover formation is sandstone with gas accumulation. Its grain ranges from well to very good and is also mixed with other sandstones with medium to coarse grains. In this formation there are alternations with siltstone, claystone and also a little coal.

Simultaneous Seismic Inversion

The seismic inversion used to obtain a model that describes physical properties of subsurface using information obtained from field data by utilizing information from impedance [2]. The earth's reflectivity model will be calculated from the input in the form of seismic response using an inversion algorithm. Based on input data, the inversion method is divided into two types: post-stack inversion and pre-stack inversion. Furthermore, the pre-stack inversion can also be divided into two methods based on the process, namely linear and non-linear methods. An example of a pre-stack seismic inversion method that uses a linear method is simultaneous seismic.

The process of simultaneous inversion is carried out using several inputs, namely seismic gather data or by combining partial angle stacks, low frequency models and wavelets. Mathematically, information on acoustic impedance (AI or Zp) and shear impedance (SI or Zs) is obtained from linear functions [3]:

$$Ln(Zs) = kln(Zp) + kc + \Delta Ld. \quad (1)$$

$$\ln(Zd) = m\,ln\,(Zp) + mc + \Delta Ld. \quad (2)$$

A value of k, kc, m, and mc is obtained from relationship between Ln(Zs) versus Ln(Zp) and ln(*p*) versus ln(Zp) as shown in Figure 3.

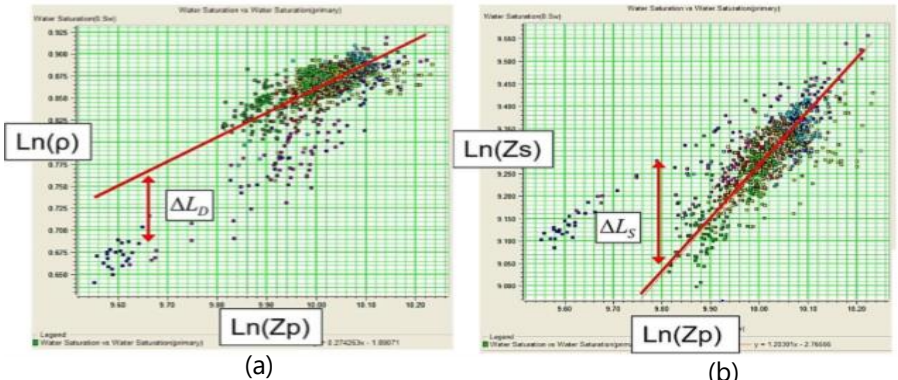

(a) (b)

Figure 3. Cross-plots (a) Ln(Zp) and Ln(p), (b) Ln(Zp) and Ln(Zs) [2]

The deviations away from straight line, ΔLs and ΔLd are the desired fluid anomaly. By combining trace equation, Fatti's equation, and two equation above, angle trace equation is obtained as follow [3]:

$$T(\theta) = ć1W(\theta)DLp + ć2W(\theta)D\Delta Ls + W(\theta)c3D\Delta Ld, \quad (3)$$

where,

$$ć1 = \left(\frac{1}{2}c1\right) + \left(\frac{1}{2}\right)kc + mc3; \quad (4)$$

$$ć2 = \left(\frac{1}{2}\right)c2; \quad (5)$$

$$c1 = 1 + \ tan^2\theta\ ;\ c2 = -8\gamma^2 tan^2\theta\ ; c3 = -0.5tan^2\theta + 2\gamma^2 sin^2\theta\ ;\ \gamma = \frac{Vs}{Vp}, \quad (6)$$

To solve equation (3), initial impedance model (low frequency model) is used and then iterate the equation using gradient conjugate method. The solution of acoustic Impedance (Zp) , Shear Impedance (Zs), and density (ρ) values is obtained as follows:

$$Zp = \exp(Lp). \quad (7)$$

$$Zs = \exp(kLp + kc + \Delta Ls). \quad (8)$$

$$\rho \ = \exp\left(mLp + mc + \ \Delta Ld.\right. \quad (9)$$

Lame Parameter

Lame parameter is a physical parameter derived from the equation for P-wave velocity (Vp) and the S-wave velocity (Vs). This parameter is used to determine physical properties of the rock, namely rigidity (μ) and incompressibility (λ). Both of these physical properties can be used to identify reservoir rocks below the surface. The Lame parameter [4] is derived as follows:

$$\mu\rho = \ Zs^2, \quad (10)$$

$$\lambda\rho = Zp^2 - 2Zs, \quad (11)$$

$$\lambda/\mu = \frac{\lambda\rho}{\mu\rho}. \quad (12)$$

RESULT AND DISCUSSIONS

Sensitivity Analysis

AI vs SI

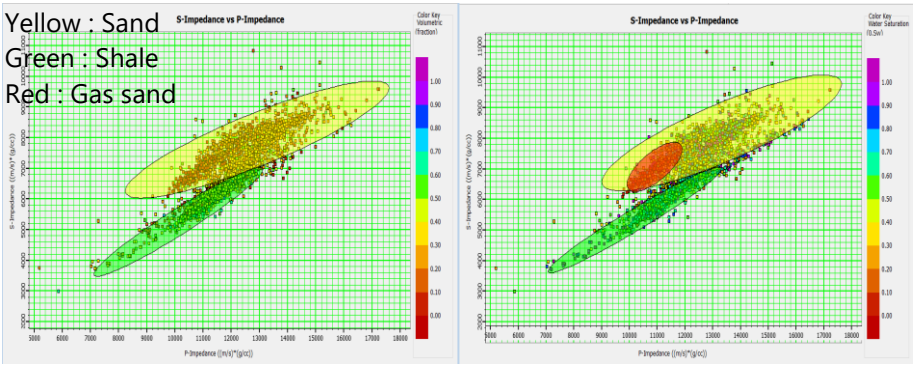

(a) (b)

Figure 4. Cross-plot between log impedance P values and Neutron Porosity with information on the color key (a) Vshale and (b) water saturation

P-impedance log is cross-plotted with S-Impedance in color key Vshale (Figure 4a) and Water Saturation (Figure 4b). Figure 4a shows that in general, sandstone zone (yellow circle) has higher P-impedance and S-impedance value compared to shale zone (green circle). From the cross-plot, gas-saturated sandstone (red circle) has low P-impedance and low S-impedance compared to wet sand. However, gas sand is difficult to identified solely from two impedances since there is still overlap between those zones.

λρ vs μρ

Figure 5 shows a cross-plot between $\lambda\rho$ and $\mu\rho$. Sandstone zone has same range in $\lambda\rho$ with shale zone and there is overlap between two zones for $\mu\rho$ value (Figure 5a). Gas sand zone has low λρ value and low μρ value compared to wet sand. However, there is still overlay between gas sand and shale (Figure 5b).

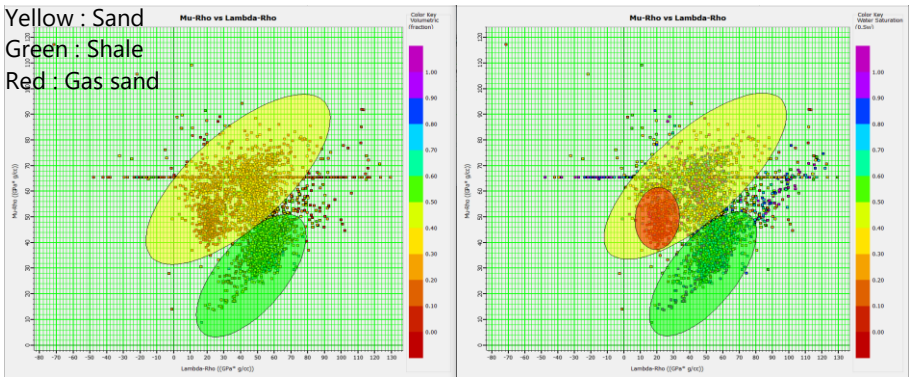

(a) (b)

Figure 5. Cross-plot between log Lambda-Rho and Mu-Rho log values with information on the color key (a) Vshale and (b) water saturation

λρ vs λ/μ

Cross-plot between λρ and λ/μ shows good separation between sandstone and shale for λ / μ value (Fig. 6a). From Fig. 6b, it can be seen that gas sand has low λ / μ value and a low λρ value. In this cross-plot, there are no overlap zones between gas sand and shale.

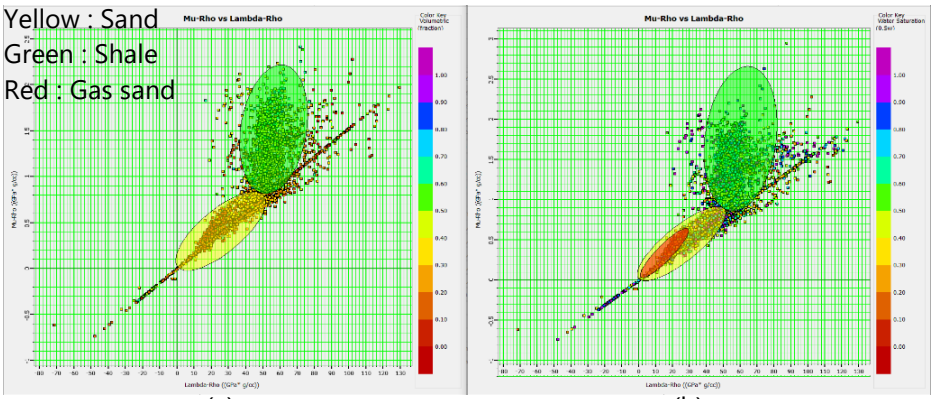

(a) (b)

Figure 6. Cross-plot between log Lambda-Rho and Lamda over Mu values with information on the color key (a) Vshale and (b) water saturation

From sensitivity analysis, it can be concluded that combination of Lame parameter can differentiate gas sand presence. The value of elastic and Lame parameter for each lithology are listed in Table 1 below.

Table 1. Sensitivity analysis result

Lithology	AI $ms^{-1}gcc^{-1}$	SI $ms^{-1}gcc^{-1}$	λρ $GPaGcc^{-1}$	μρ $GPaGcc^{-1}$	λ/μ
Sand	9.000 – 17.000 (high)	6.500 – 10.000 (high)	0 – 50 (low)	35- 90 (high)	0 – 1 (low)
Shale	7.000 – 13.000 (low)	3.800 – 7.000 (low)	50 – 80 (high)	0 – 50 (low)	1 – 2.5 (high)
Gas Sand	10.000 – 12.000	6.500 – 8.000	0- 40	40 – 60	0 – 0,8

Wavelet Estimation and Low Frequency Model

Statistical wavelets are extracted from each partial angle stack with 100 msec length and time window around reservoir interval (Figure 7). The amplitude spectrum shows wavelet at near angle has higher frequency content compared to wavelet extracted from far angle. These wavelets will be used in the inversion process.

To build low frequency model, P-impedance and S-impedance data from five wells is interpolated through study area guided by top and base of Plover horizon.

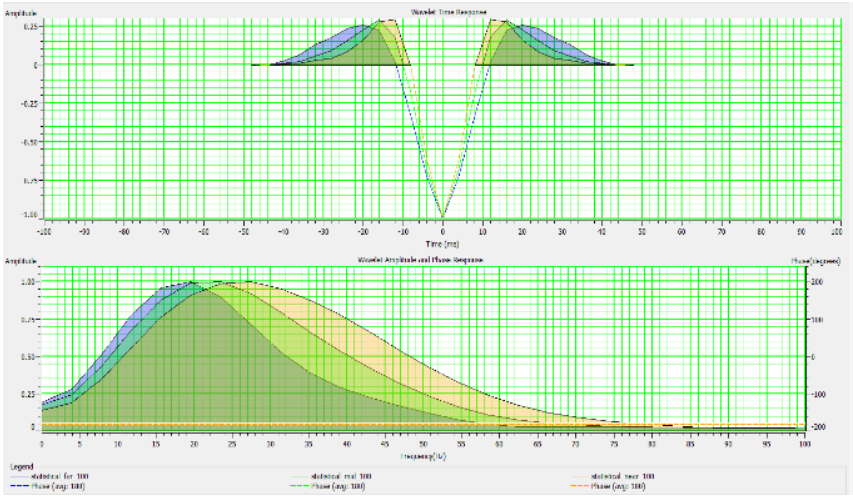

Figure 7. Wavelet extracted at near (orange), mid (green), and far(blue) angle stack

Inversion Result

To check whether wavelets, low frequency model and inversion parameter is good enough, an inversion process is first applied at well location. Figure 8 shows an example of inversion analysis at Poseidon-1 with P-impedance and S-impedance inversion results (red curve), log data (blue curve) and low frequency model (black curve). P-Impedance inversion error for Poseidon-1 well is around 10% (compared to average P-impedance log) with correlation between log and inversion result is 0.77, and S-impedance error is around 14% with correlation 0.74. In average P-impedance error is around 10%, correlation 0.63 and for S-impedance is around 11% in error and its correlation is 0.61.

Vol.4 No.I Tahun 2021, 63 – 73
P-ISSN: 2621-0215, E-ISSN: 2621-489X

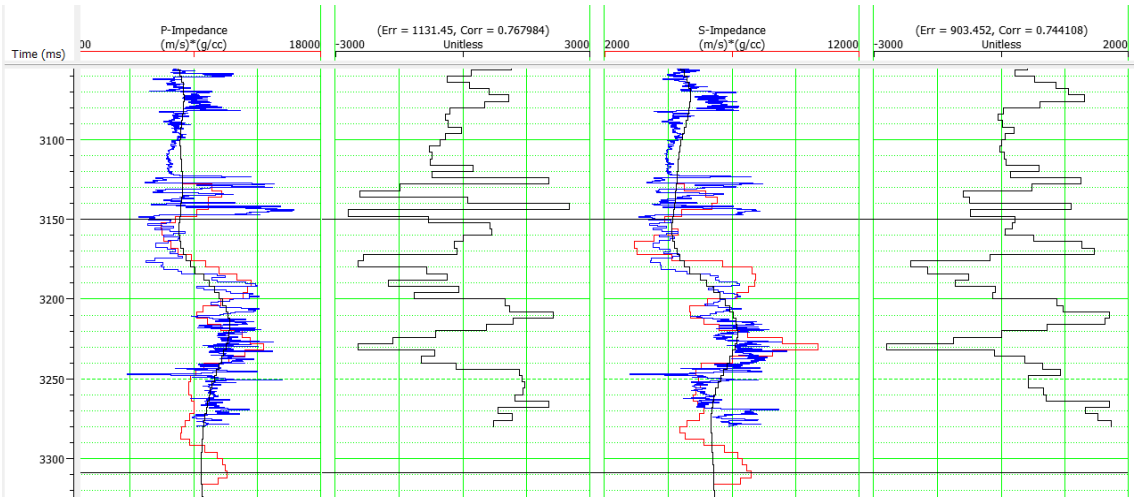

Figure 8. Inversion analysis at Poseidon-1 well

The inversion process is then applied to whole study area and will focus from the top to the base of Plover formation. Figure 9 shows inversion result of P-impedance and S-impedance at a line that passes Kronos well. From Figure 9a, there is low P-impedance value above base of Plover formation that might be related to gas presence.

To obtained more information based on Table.1, volume of P-impedance and S-impedance resulted from simultaneous inversion will be transformed into combination of Lame parameters (λρ, μρ, and λ / μ) volumes.

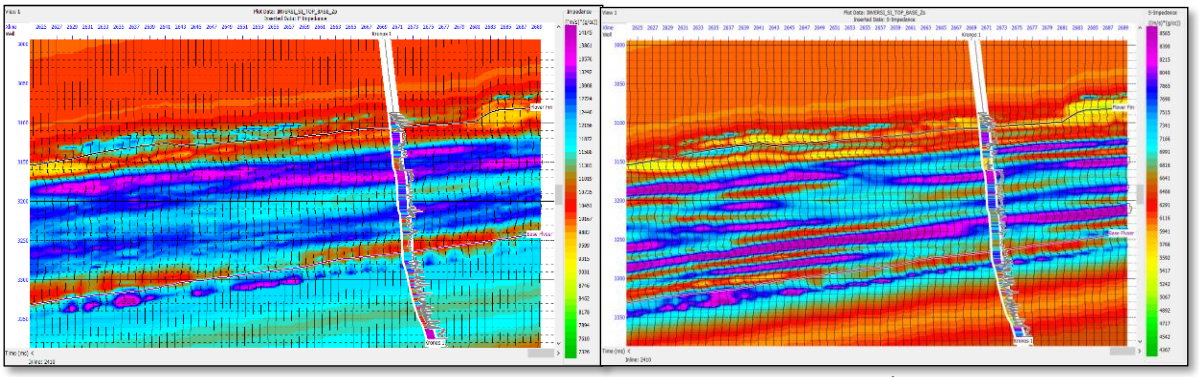

(a) (b)

Figure 9. Inversion results around Kronos well (a) P-Impedance, (b) S-Impedance

Figure 10 shows combination of λρ, μρ, and λ / μ parameter sections that passes Kronos well. Based on sensitivity analysis listed in Table 1, areas with low λρ, high μρ and low λ /μ values are estimated as gas sand interval in this study area.

Vol.4 No.I Tahun 2021, 63 – 73
P-ISSN: 2621-0215, E-ISSN: 2621-489X

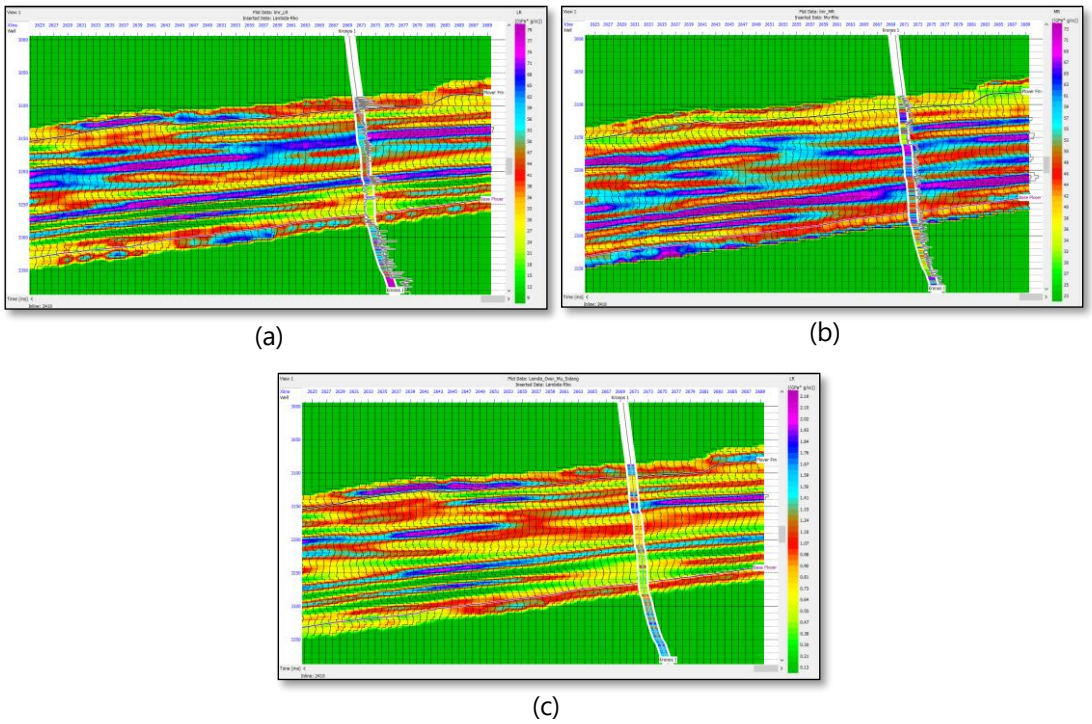

Figure 10. (a) Lambda rho, (b) Mu rho, (c) Lamda over Mu sections around Kronos well

Identification of Gas Sand Distribution at Plover Formation

Based on the interpretation of the log data, it is known that the gas sand interval is around the base of Plover formation (Figure 11). Therefore, the map of elastic and combination of Lame parameters will be extracted around base of Plover interval.

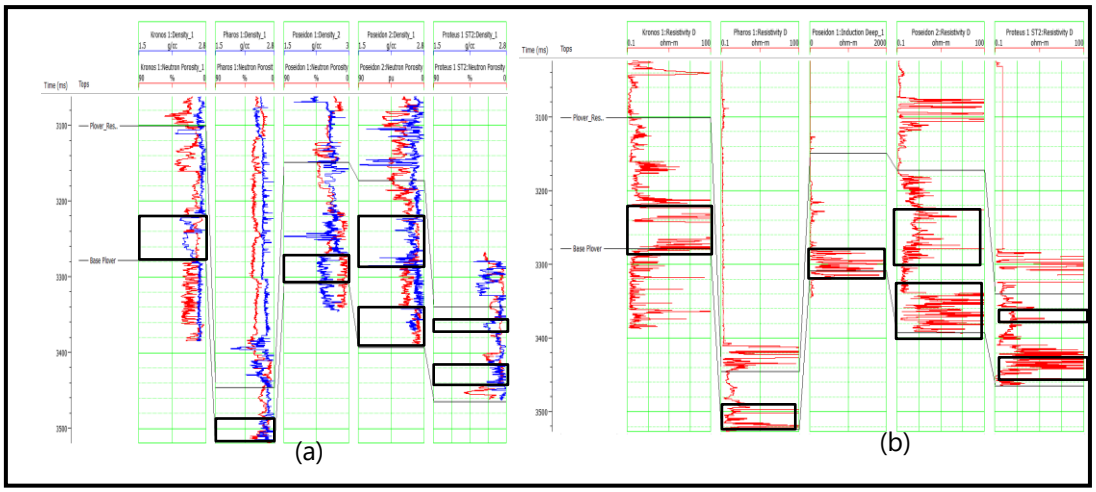

Figure 11. Interpretation of the gas sand zone at log (a) Neutron-Density and (b) Resistivity

Based on Table.1, S-Impedance (SI) value of gas sand is higher compared to surrounding. Figure 12(a) show SI map and zone with high SI value is inside the black polygon. Meanwhile, map of λρ around interval of interest is shown in Figure 12(b). The area with a low λρ value is also bounded by a black line. Based on those maps and combined with a μρ map then we draw a polygon with high μρ in Figure12(c). The result of overlapping between three maps is considered so far as gas sand area.

To increase the accuracy of interpretation, λ / μ is also mapped as shown in Figure 12(d). Area with low λ / μ values is indicated by black polygon. Based on the overlay of all maps (AI, SI, λρ, μρ, and λ / μ), it can be concluded gas sand area spreads in the eastern and western areas of this research area. This zone is located near to Kronos well, Poseidon-2 and Pharos well. From quick look interpretation on the log data, those three wells contained thick gas sand near base of Plover formation. Further study on relationship between those parameters with gas thickness need to be carried out to have more understanding about reservoir characterization in this field.

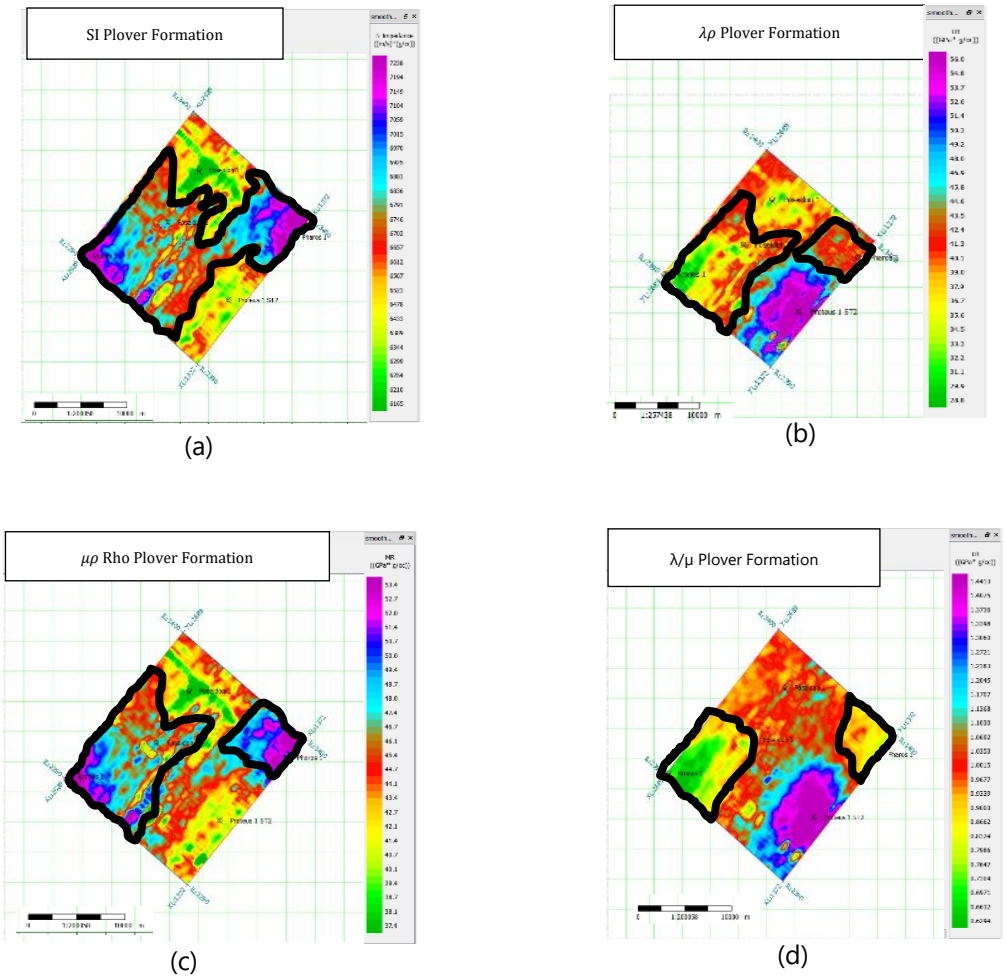

Figure 12. (a)SI, (b) $\lambda\rho$, (c) $\mu\rho$, and (d) λ/μ distribution map in plover formation

CONCLUSIONS

From the results of this study, it can be concluded that:

A. Parameters λρ and λ / μ are the best parameters to identify the distribution of gas sand in this research area. The gas sand area will have a value of λρ less than 30 GPa g / cc while the value of λ / μ will be less than 0.8 GPa g / cc.
B. From inversion analysis, the average correlation between the inversion results and log data gives good correlation around 0.61 with 10% error both in P-impedance and S-impedance.

C. Based on the results of the distribution of AI, SI, λρ, μp, and λ / μ values, it is known that the gas sand area is in the eastern and western areas of this research area.

REFERENCES

[1] Struckmeyer, H.I.M., J.E. Blevin, J. Sayers, J.M. Totterell, K. Baxter and D. Cathro. 1998. "Structural Evolution of The Browse Basin, North West Shelf: New Concepts From Deep Seismic Data". *In The Sedimentary Basin of Western Australia 2*, edited by P. G. Purcell and R.R. Purcell. 345 -367. Exploration Society of Australia.

[2] Sheriff, Robert.2002. "Encyclopedic Dictionary of Applied Geophysics – Fourth Edition". Tulsa: Society of Exploration Geophysicists.

[3] Hampson, Daniel P., and Brian H. Russell Brad Bankhead. 2005. "Simultaneous Inversion of Pre-Stack Seismic Data". SEG Technical Program Expanded Abstract 24(1):13-17.

[4] Goodway, Bill, Taiwan Chen, and Jon Downton. 1997. "Improved AVO fluid detection and lithology discrimination using Lame Petophysical Parameters; λρ,μρ, & λ/μ Fluid Stack, From P and S Inversion". *SEG Technical Program Expanded Abstract 1997* 1: 183-186.


9 772621 489007


9 772621 021009